Optimisation of analog and digital silicon photomultipliers for the positron emission tomography

A PhD thesis submitted to the

University of Milano-Bicocca

for the degree of

Doctor of Philosophy

presented by

Liu Zheng

Master of Science, Swiss Federal Institute of Technology Zurich
Bachelor of Science, Xi'an Jiaotong University
born on December 9 1986 in Changsha (China)
citizen of Changsha

accepted on the recommendation of
Prof. Dr. Marco Paganoni, examiner

2015

Abstract

This research is focusing on the development of medical imaging devices based on particle detectors, in particular in the field of positron emission tomography (PET). Part of the study of the silicon photomultiplier (SiPM) is on the optimisation of the timing performance for the EndoTOFPET-US detector. The aim of the EndoTOFPET-US project is to develop a multi-modal imaging tool combining ultrasound with time-of-flight PET into an endoscopic imaging device. One of the objectives is to reach a coincidence time resolution (CTR) of 200 ps full width at half maximum (FWHM).

An experimental setup was developed to evaluate 256 multi-pixel photon counter (MPPC) arrays (S12643-050CN) for the external plate of the EndoTOFPET-US project to ensure the performance of each component of the detector. A full study of the breakdown voltage, dark count rate, single photon time resolution (SPTR) for the MPPC array was performed and shows the MPPC array is a low noise photon detection device and has good timing performance of SPTR. An average CTR value of 239 ps FWHM has been measured by an an ultra-fast amplifier-discriminator NINO ASIC and High Performance general purpose TDC (HPTDC) for the 256 MPPC arrays coupling with $3.5\times3.5\times15\text{mm}^3$ Lutetium-yttrium oxyorthosilicate (LYSO) 4×4 crystal matrices. Single LYSO crystal coupled to the MPPC array reached CTR of 170 ps better than the value of 239 ps measured. With the study of the different cross section of LYSO crystal, I found a degrading of timing performance due to the light loss because the scintillator has larger size than the dimension MPPC. Additionally, I also found that the crosstalk in the HPTDC will degrade the timing performance. So I can conclude that optimizing the coupling between crystal and SiPM and better performance of electronics can improve the timing performance of PET detector. I have also studied the energy resolution of the multichannel digital SiPM (MD-SiPM) device designed by Delft University of Technology for the endoscopic probe for the EndoTOFPET US project. The energy measurement using the MD-SiPM coupled to the LYSO fiber crystal matrices with each cell size of $0.7\times0.7\times10\text{mm}^3$. 511 keV photon peak can be identified for each channel and 18.26% energy resolution (FWHM) for 511 keV has been achieved.

Another concept of digital silicon photomultiplier (SiPM) has been introduced by Philips as an innovative technology to analog silicon photomultiplier devices. The Philips digital SiPM, has a pair of time to digital converters (TDCs) connected to 12800 single photon avalanche diode (SPAD) cells. Detailed measurements were performed to understand the low photon level response of Philips digital SiPM. The single photon time resolution (SPTR) of each SPAD cell in a pixel consisting 3200 cells was measured and a mean value of 85 ps full width half maximum (FWHM) was observed for these cells. Each SPAD cell sends the signal to the TDC with different signal propagation time, which resulting a so called trigger network skew in the Philips digital SiPM. This statistical distribution of the trigger network skew for a pixel (3200 SPAD cells) has also been measured and a variation of 49.84 ps FWHM was extracted from the fit to the distribution. The SPTR value of the whole pixel of die is the combination of SPAD jitter, trigger network skew, SPAD non-uniformity. The SPTR of pixel is 103 ps at 3.3 V. The effect of the crosstalk at low photon level response has also been studied. The two photon time resolution degrades if the events combined not only the true 2-photon events and also the crosstalk events.

Silicon photomultipliers (SiPMs) and scintillators are often arranged in the shape of arrays in Positron Emission Tomography (PET) systems. Digital SiPMs provide signal readout

in single photon avalanche diode (SPAD) level. From the photon count rate measurement of each SPAD cell of digital SiPM, we found that the output scintillating photons distribute in an area larger than the scintillator physical coupling area. Taking advantage of the possibility to enable/disable individual cells of the digital SiPM, a group of Lutetium-yttrium oxyorthosilicate (LYSO) crystals with different dimensions coupled to a digital SiPM was used to study the influence of using different SiPM active area on the number of photons detected, energy resolution and coincidence time resolution (CTR). For the same crystal coupled to the digital SiPM, the larger the active area of digital SiPM, the higher the number of photons detected. The larger active area of the digital SiPM also results in a better energy resolution after saturation correction. The best energy resolution full width half maximum (FWHM) obtained for the 2×2×5 mm^3, 2×2×10 mm^3, 2×2×15 mm^3, 2×2×20 mm^3 LYSO crystals was 10.7%, 11.6%, 12.1%, 12.5%, respectively. For crystals with different cross sections coupled to the digital SiPM, we found that the larger the cross section of coupling area, the more photons were detected and thus a better energy resolution was obtained. The CTR of crystals fully wrapped with Teflon or without wrapping was measured by positioning two identical crystals facing each other. A larger area of digital SiPM improves the CTR and the CTR reaches the plateau when the active area is larger than 2.2×2.2 mm^2 with both two configurations of wrapping. The best CTR value for the 2×2×5 mm^3, 2×2×10 mm^3, 2×2×15 mm^3, 2×2×20 mm^3 LYSO crystals was 128.87 ps, 148.41 ps, 171.59 ps, 177.88 ps, respectively. The measurements performed lead us to conclude that optimising the coupling between crystal and SiPM to extract more scintillating photons can improve the energy resolution and CTR.

Contents

1 Positron emission tomography **3**
- 1.1 Positron emission . . . 4
- 1.2 Time of flight PET . . . 5
  - 1.2.1 Principles of PET . . . 5
  - 1.2.2 Time of flight . . . 6
- 1.3 Scintillation detector . . . 7
  - 1.3.1 Scintillator . . . 8
  - 1.3.2 Photon detector . . . 10
  - 1.3.3 Front end electronics . . . 13
  - 1.3.4 Readout system . . . 15
- 1.4 EndoTOFPET-US detector . . . 16

2 Silicon photomultiplier **19**
- 2.1 Basic characteristics of silicon photomultiplier . . . 19
  - 2.1.1 Breakdown voltage . . . 19
  - 2.1.2 SPAD quenching . . . 21
  - 2.1.3 Gain . . . 22
  - 2.1.4 Photon detection efficiency . . . 22
  - 2.1.5 Dark noise . . . 24
  - 2.1.6 Optical crosstalk . . . 24
- 2.2 Digital silicon photomultiplier . . . 26

3 Characterization of analog silicon photomultiplier **29**
- 3.1 Current-voltage curve . . . 30
- 3.2 Dark count rate . . . 33
- 3.3 Crosstalk . . . 34
- 3.4 Single photon time resolution . . . 35
- 3.5 Coincidence time resolution . . . 37
  - 3.5.1 Coincidence time resolution with scintillator matrices . . . 37
  - 3.5.2 Study of the effects degrading the coincidence time resolution . . . 39
- 3.6 Conclusion . . . 41

4 Multichannel digital Silicon photomultiplier **43**
- 4.1 Architecture of MD-SiPM chip . . . 43
- 4.2 Operation sequence of MD-SiPM chip . . . 45
- 4.3 Dark count rate . . . 46
- 4.4 Single photon time resolution . . . 47

4.5 Light yield with scintillation crystal 49
4.6 Conclusion 50

5 Digital silicon photomultiplier of Philips 53
5.1 Layout of Philips digital silicon photomultiplier 53
5.2 Data acquisition sequence 54
5.2.1 Trigger scheme 55
5.2.2 Validation process 55
5.3 Basic characteristics of Philips digital photon counter 57
5.3.1 Breakdown voltage 57
5.3.2 Dark count rate 57
5.3.3 Crosstalk 58
5.4 Single photon time resolution 59
5.4.1 Setup 59
5.4.2 Single photon time resolution 60
5.4.3 Low photon number time resolution and crosstalk 63
5.5 Time resolution from single photon to multi-photons. 64
5.6 Conclusion 65

6 Optimisation for energy resolution and CTR 67
6.1 Setup 67
6.2 Crystal position identification and active area selection 68
6.3 Energy resolution and light yield output 70
6.4 Coincidence time resolution 74
6.5 Conclusion 78

7 Summary and conclusion 81

List of Figures

1.1 Schematic of PET. Picture is taken from [8]. 3
1.2 Schematic of positron emission and annihilation process. Picture is taken from [7]. 4
1.3 Principles of PET. The red point corresponds to a tumour cell. 5
1.4 Example of a scatter event. 5
1.5 Example of a random coincidence event. 5
1.6 Principle of Time of Flight PET. 6
1.7 (A) Representative slices from reconstruction images of NEMA torso phantom using TOF and non-TOF IRX algorithms for 2 different scan times. (B) Representative slices from reconstruction images of larger phantom with 35 cm diameter using TOF and non-TOF UPenn algorithms for 2 different scan times. 10 iterations of reconstruction are used for the images. [11] 7
1.8 Schematic of detector based on scintillation. 8
1.9 Drawing of the head on type photomultiplier tube. Picture is taken from [16]. 10
1.10 Typical response of PMT for different wavelength of light. Plot is taken from [16]. 11
1.11 Left plot: Drawing of the avalanche process in APD. Right plot: Drawing of the Geiger-mode avalanche development. Picture is taken from [18]. 12
1.12 A typical design of a front end circuit for scintillation detector. Picture is taken from [14]. 13
1.13 A typical plot of Time over Threshold method. Plot is modified from [21]. . . 13
1.14 Picture of eight channel NINO ASIC. 14
1.15 The principle of the counter based TDC. Picture is taken from [27]. 15
1.16 The architecture of HPTDC chip. Picture is taken from [28]. 16
1.17 The principle of R-C delay line for HPTDC. Picture is taken from [28]. 17
1.18 The EndoTOFPET-US detector system. The left is a miniaturised PET head together with a commercial ultrasound endoscope. The right is a external plate detector outside of the patient opposing to direction of the PET detector head. 18
1.19 The external plate composition of EndoTOFPET-US detector system. . . . 18

2.1 Typical structure of a SiPM. 19
2.2 Microscopic picture of a multi-pixel photon counter (MPPC) (S12643-050CN) from Hamamatsu. 20
2.3 . Electron ionization rate as function with electric field at different temperatures. Picture is modified from [35]. 20
2.4 Normalized breakdown voltage as a function of temperature for different doping concentrations. Picture is modified from [35]. 20

2.5 Typical signal of a SPAD. 21
2.6 Oscilloscope picture of the signal from Hamamatsu MPPC (S10931-050P). . . 21
2.7 Gain as a function of the bias voltage for MPPC (S10931-050P). The line is a linear fit to the data points whose errors are within the symbol. Plot is taken from [38]. 23
2.8 PDE as a function of wavelength. The SiPM is AdvanSiD RGB-SiPM. Plot taken from [39]. 24
2.9 A schematic view of two types structure of for a SPAD. On the left is the so-called p-on-n structure (predominantly blue- sensitive) and on the right is the n-on-p (predominantly red-sensitive) structure. Picture is taken from [19]. 25
2.10 Schematic representation of optical crosstalk between two SPAD cell A and SPAD cell B. When a external photon triggers an avalanche in the SPAD cell A, some internal photons are emitted from the avalanche. These photons propagate through the bulk of the array and finally they trigger another avalanche in the SPAD cell B. Picture is taken from [44]. 25
2.11 Optical crosstalk probability as a function of the over bias voltage. The SiPM type PM1150 is produced by KETEK standard technology and KETEK trench technology which used to reduce the crosstalk. Plot is taken from [47]. 26
2.12 Different concepts of analog and digital SiPM. (a) Typical analog SiPM, (b) Full digital SiPM , (c) Conventional digital SiPM, (d) Multi-TDC digital SiPM. Picture is modified from [50]. 27

3.1 The picture of MPPC array (S12643-050CN). 29
3.2 The drawing of the MPPC array (S12643-050CN) and its dimension description. Picture is taken from [56]. 29
3.3 The drawing of the setup of current-voltage measurement and dark count rate measurement. 30
3.4 Picture of the printed circuit board (PCB) for the MPPC array characterisation. 30
3.5 Current as a function of the applied bias voltage. The measurement is at 19 °C. 31
3.6 An example of the breakdown voltage extracted by the I-V method is shown. The measurement is at 19 °C. 31
3.7 The distribution of the difference of maximum and minimum breakdown voltage within MPPC array for 256 MPPC arrays. 32
3.8 The breakdown voltage distribution of each MPPC in the 256 MPPC arrays. 32
3.9 Breakdown voltage as a function of the temperature. 33
3.10 DCR as a function of NINO threshold. The over bias voltage is 3 V with temperature at 18 °C. 33
3.11 DCR distribution of 256 MPPC arrays. 34
3.12 DCR as a function of temperature. 34
3.13 Crosstalk as function of the over bias voltage at different temperatures. . . . 35
3.14 Single photon ToT spectrum. 35
3.15 Histogram of time difference of selected single photon events. 36
3.16 Single photon time resolution as function of over bias voltage. 36
3.17 Single photon time resolution as function of NINO threshold. 37
3.18 CTR bench for the quality control measurement. 37
3.19 CTR of 3×3×15 LYSO crystal. 38
3.20 CTR of 3×3×15 LYSO crystal. 38

3.21 CTR as function of over bias voltage for 3.5×3.5×15 mm^3 LYSO crystal matrices. 39
3.22 CTR of 3.5×3.5×15 mm^3 LYSO crystal with NINO threshold. The over bias voltage of two MPPC arrays fixed at 3.5 V. 39
3.23 CTR as function of over bias voltage for 3.5×3.5×15 mm^3 LYSO crystal matrices. 40
3.24 CTR as function of the over bias voltage for two sets of LYSO crystals. The over voltage of one MPPC array fixed at 3.5 V. The NINO threshold was fixed at 55 mV. 40
3.25 CTR in different configuration of 3×3×15 mm^3 LYSO crystal. The over bias voltage of one MPPC array fixed at 3.5 V. 41
3.26 The crosstalk calculated by the ToT from all channels for the 511 keV photon event. The channel with 100% is the trigger channel. The over bias voltage of one MPPC array fixed at 3.3 V. 42
3.27 The mean value of the register time in the HPTDC. The channel with 0.0 ns is the trigger channel and other channels have the relative time to the trigger channel. 42

4.1 The plot of 9 × 18 array MD-SiPM. Top right is the zoom in plot of one array of the MD-SiPM. Single SPAD cell is also shown in the bottom of right side. Picture is modified from [66]. 43
4.2 Plot of the TDC connection to pixels of the chip. 44
4.3 The schematic of single SPAD cell circuit. Picture is taken from [66]. 45
4.4 The flowchart of the MD-SiPM data acquisition. 45
4.5 Left plot: DCR map of the whole pixels in the MD-SiPM chip. Plot on the top of right: Zoom in of an array on the left plot. Plot on the bottom of right: Histogram of the DCR of all pixels. The over bias voltage was 2.5 V at 18 °C. 46
4.6 Mean value of array DCR as function of the percentage of active pixels at different over bias voltage. 47
4.7 The data count number recorded without smart reset and with smart reset. The plot is taken from [68]. 47
4.8 Schematic of the single photon time resolution setup. 48
4.9 Pixels fired distribution for an array of MD-SiPM in absence of light. The over voltage was 2.5 V and the temperature was at 18 °C. 48
4.10 Number of fired pixels in the SPTR measurement. The over voltage is 2.5 V. 49
4.11 Histogram of the photon arriving time. The over voltage is 2.5 V. 49
4.12 SPTR as a function of the over voltage. 40% of the pixels are inhibited. . . . 49
4.13 Picture of the glued crystal matrices and MD-SiPM chip. 50
4.14 Fit of the array of 511 keV photo peak. 51
4.15 Distribution of the energy resolution for 16 arrays. 51
4.16 ^{22}Na spectra in the triggered array and spectra of neighbour arrays. 52

5.1 Image of Philips DPC-3200-22 sensor. 53
5.2 Layout and dimension of Philips digital SiPM [69]. 54
5.3 Layout and dimension of single die composed of 4 pixels. Each pixel consists 3200 SPAD cells. 54
5.4 Schematic of the data acquisition. Picture taken from [69]. 54
5.5 The validation configuration network of the Philips digital SiPM. Picture taken from [69]. 56
5.6 DCR of one die as function of over bias voltage at different temperature. . . . 57

5.7 DCR as function of percentage of active cells for one die. The over bias voltage is 3.3 V. The temperature is 18 °C. 57
5.8 DCR distribution of the 12800 cells in one die. The over bias voltage of the chip is 3.3 V. The temperature is 18 °C. 58
5.9 The crosstalk probability map of a centre SPAD cell. 58
5.10 Crosstalk as function of over bias voltage. 59
5.11 SPTR setup. All the measurements were performed at 18°C. 59
5.12 Histogram of the photon count for low intensity laser light (left), the single photon time spectra (middle) and the two photon time spectra (right). 60
5.13 Time resolution of each cell at 1 photon level at 18 °C with different over voltage. 60
5.14 Distribution of SPTR for 3200 SPAD cells in one pixel. 61
5.15 Distribution of skew for 3200 SPAD cells in one pixel. 61
5.16 SPTR as a function of over voltage at different illuminating spot sizes. The temperature was 18 °C. 62
5.17 Distribution of the mean value of the delay time of each cell. The measurements were performed at 3.3 V over bias voltage and at 18°C. 62
5.18 Time resolution with different photon level at 18 °C at 3.3 V over bias voltage. 64
5.19 Delay time with different photon level at 18 °C at 3.3 V over bias voltage. . . 64
5.20 Red colour: time histogram of two photon events due to crosstalk and random coincidence. Blue colour: time histogram of two photon events due to two photons from laser light. 65
5.21 Time spectra of single cell at 18 °C at 3.3 V over voltage. 65
5.22 Time spectra at 9 photon event at 18 °C at 3.3 V over voltage. 66
5.23 Time resolution with different level of detected photons. The sensor is operated at 3V over bias voltage and at 19°C. 66
5.24 Delay time with different level of detected photons.The sensor is operated at 3V over bias voltage and at 19°C. 66

6.1 Setup for scintillating crystal measurement. All measurements were performed at 18°C inside a dark box. 68
6.2 Photon count rate map of single LYSO crystal with dimension of 2×2×15 mm^3 glued on the Philips digital SiPM. The crystal was fully wrapped with Teflon. The measurement was performed at 2 V over bias voltage and the temperature was 18°C. 68
6.3 Plot of photon count rate map of one pixel of the Philips digital SiPM. A single 2×2×15 mm^3 LYSO crystal glued on it. The crystal was fully wrapped with Teflon. The measurement was performed at 2 V over bias voltage and the temperature was 18 °C. 69
6.4 Left: ^{22}Na spectra with 2×2×15 mm^3 LYSO crystal at 3.3 volt over bias voltage with 100% cells activated. Right: Saturation corrected energy spectra of left ^{22}Na spectra. The measurements were performed at 18 °C. 69
6.5 Light output of 2×2×15 mm^3 LYSO crystal coupled to digital SiPM with 2.5×2.5 mm^2 active area for different gamma energies. The measurements were performed at 3.3 V over bias voltage and the temperature was 18 °C. . . 70
6.6 Number of photons detected by using different active area of digital SiPM. The measurements were performed at 3.3 V over bias voltage and the temperature was 18 °C. 71

6.7 Number of photons impinging to the SiPM by using different active area of digital SiPM after saturation correction. The measurements were performed at 3.3 V over bias voltage and the temperature was 18 °C. 71
6.8 Energy resolution without correction by using different active area of digital SiPM. The measurements were performed at 3.3 V over bias voltage and the temperature was 18 °C. 72
6.9 Energy resolution with saturation correction by using different active area of digital SiPM. The measurements were performed at 3.3 V over bias voltage and the temperature was 18 °C. 72
6.10 Correlation plot of number of photons impinging to the SiPM and energy resolution after saturation correction for different LYSO crystals. The measurements were performed at 3.3 V over bias voltage and the temperature was 18 °C. 73
6.11 Coincidence time resolution plot of two 2×2×20 mm^3 LYSO crystals coupled to digital SiPM. The measurement was performed at 3.3 V over bias voltage and the temperature was 18 °C. 73
6.12 Coincidence time resolution with different over bias voltage of 2×2×15 mm^3 LYSO crystal. The measurements were performed when 100% in cells one pixel is enabled. The temperature was 18 °C. 74
6.13 Coincidence time resolution with different level of activated cells of 2×2×15 mm^3 LYSO crystal. The measurements were performed at 3.5 V over bias voltage and the temperature was 18 °C. 74
6.14 Coincidence time resolution for LYSO crystal with dimension of 2×2×5 mm^3 at different sizes of digital SiPM active area. The measurements were performed at 3.5 V over bias voltage and the temperature was 18 °C. 75
6.15 Coincidence time resolution for LYSO crystal with dimension of 2×2×10 mm^3 at different sizes of digital SiPM active area. The measurements were performed at 3.5 V over bias voltage and the temperature was 18 °C. 75
6.16 Coincidence time resolution for LYSO crystal with dimension of 2×2×15 mm^3 at different sizes of digital SiPM active area. The measurement were performed at 3.5 V over bias voltage and the temperature was 18 °C. 76
6.17 Coincidence time resolution for LYSO crystal with dimension of 2×2×20 mm^3 at different sizes of digital SiPM active area. The measurement were performed at 3.5 V over bias voltage and the temperature was 18 °C. 76
6.18 Schematic of the Geant4 simulation model. 76
6.19 Simulation result of $2 \times 2 \times 20\ mm^3$ LYSO crystal. The plot is the position distribution of output scintillating light. 77
6.20 Simulation result of $2 \times 2 \times 20\ mm^3$ LYSO crystal. The plot is position distribution of output scintillating light in the first 200 ps. 77
6.21 Zoom of position distribution of output scintillating light in the first 200 ps. . 77
6.22 Simulation result of $2 \times 2 \times 20\ mm^3$ LYSO crystal. The plot is number of photons detected in the first 200 ps for different active area. 78
6.23 Simulation result of $2 \times 2 \times 20\ mm^3$ LYSO crystal. The plot is number of photons detected in the total scintillation process for different active area. . . 78
6.24 Schematic of the different regions of SiPM we selected. 79

6.25 The ratio of the number of photons detected in the first 200 ps to the number of photons detected in the total scintillation process in different regions. The ratio is calculated from the simulation result of $2 \times 2 \times 20\ mm^3$ LYSO crystal. 79

List of Tables

1.1 Properties of the most important inorganic crystal scintillators used in particle detectors [14]. 9

3.1 The CTR at different configuration for the same two single 3×3×15 mm^3 LYSO crystal coupled to MPPC array. 41

5.1 4 different trigger schemes provided in the chip and their corresponding logical connections based on sub-pixels (sp). The parameters are taken from [69]. . . 55
5.2 Six validation schemes and the logic connections for each validation scheme. . 56
5.3 Timing performance at different photon event level for 9 cells. The over bias voltage is at 3.3 V and temperate is at 18 °C. 63

6.1 Energy resolution of different cross sections of LYSO crystals. The energy resolution not corrected and saturation corrected shown in the table are the best value while choosing the optimal active area of digital SiPM for the glued crystals. The Number of photons detected and saturation corrected shown in the table are the acquired number when the active area is the total pixel. . . 72
6.2 CTR for different cross sections of LYSO crystals. 75
6.3 Properties of LYSO crystal simulated. The parameters are taken from [64], [80]. 76

7.1 Performance summary of the three different SiPMs studied in the PhD work. The value of DCR, crosstalk and PDE are all based on the optimal operation bias voltage for the CTR measurement. The value of energy resolution and CTR are based on the measurement of 3×3×15 mm^3 LYSO crystals. Some values are taken from [67], [53], [81]. 82

Introduction

The Positron Emission Tomography (PET) is a medical imaging technique widely used nowadays. Most of commercial PET scanners use the photomultiplier tube (PMT) as the photon detector in the system. However, a silicon Photomultiplier (SiPM) have great potential to replace the PMT in PET scanner thanks to its compactness, insensitivity to magnetic field and low operating voltage. More importantly, good timing performance of the SiPM make it a good candidate device for the Time of Flight (TOF) PET scanner. The TOF information has been shown to increase the signal to noise ratio and then improve the image quality of PET scanners [1]. Some prototype of TOF PET scanners developed recently achieved the time resolution in the level of 300 ps to 400 ps full width half maximum (FWHM) [2].

Apart from the normal PET scanner, an endoscopic approach PET scanner was proposed and developed by the EndoTOFPET-US project [3]. The aim of this project is to develop a multi-modal imaging tool combining ultrasound with time-of-flight PET into an endoscopic imaging device. One of the objectives is to reach a coincidence time resolution of 200 ps FWHM, corresponding to a spatial resolution of 3 cm for the system. In order to reach this object, a complete characterisation for all the photon detector components need to be performed to guarantee the noise and timing performance as same as designed before integrating the final PET scanner. The evaluation results give a referenced parameters of the optimum setting for the operation of the detector system.

A new photodetector is called digital SiPM which integrating the complementary metal-oxide-semiconductor (CMOS) technology on the SiPM chip. The digital SiPM developed by Philips was fully characterized for the performance comparison of analog and digital SiPM.

In PET systems, scintillators and detectors are often arranged in the shape of arrays. In these configurations, the scintillating light produced by each crystal can be detected by multiple channels of the detector array [4], [5]. In general, because of the large angular distribution of light exiting from a scintillator [6], the photons produced by a single crystal have a chance to hit the detector over an area larger than the cross section of the crystal itself. Digital SiPMs have the advantage of allowing the user to select the active area of the detector, by choosing whether to enable or disable each single Single-Photon Avalanche Diode (SPAD). In this thesis, I also present a study on the influence of choosing different collecting areas of SiPM on the energy resolution and coincidence time resolution (CTR) by using the digital SiPM produced from Philips.

The thesis is organised as follows:

- The first chapter introduces the basic principle of the PET technique. Detailed description of positron emission and advantage of TOF PET are also addressed. In the end the components of the scintillation detectors, and the EndoTOFPET-US project are also briefly described.

- Chapter two addresses the properties of SiPMs in detail, for example, breakdown voltage, gain, and dark noise. The two different types of SiPMs, analog SiPM and digital SiPM are also introduced.

- Chapter three concentrates to the characterisation of the analog SiPM chosen by the EndoTOFPET-US project. It also contains the study of the effects that can degrade

the time resolution when going from a single scintillation detector to a complex detector system.

- Chapter four introduces a multichannel digital silicon photomultiplier developed for the EndoTOFPET-US project by Delft University of Technology and its characterisation for noise, timing, energy performance.
- Chapter five describes a characterisation of the digital silicon photomultiplier developed by Philips. An in-depth study of the low photon level response of this device is also discussed.
- Chapter six gives the results of using the digital SiPM produced from Philips to study the influence of choosing different active areas of SiPM on the energy resolution and CTR when coupled to scintillators.
- A summary and conclusion of the thesis is given in the last chapter.

Chapter 1

Positron emission tomography

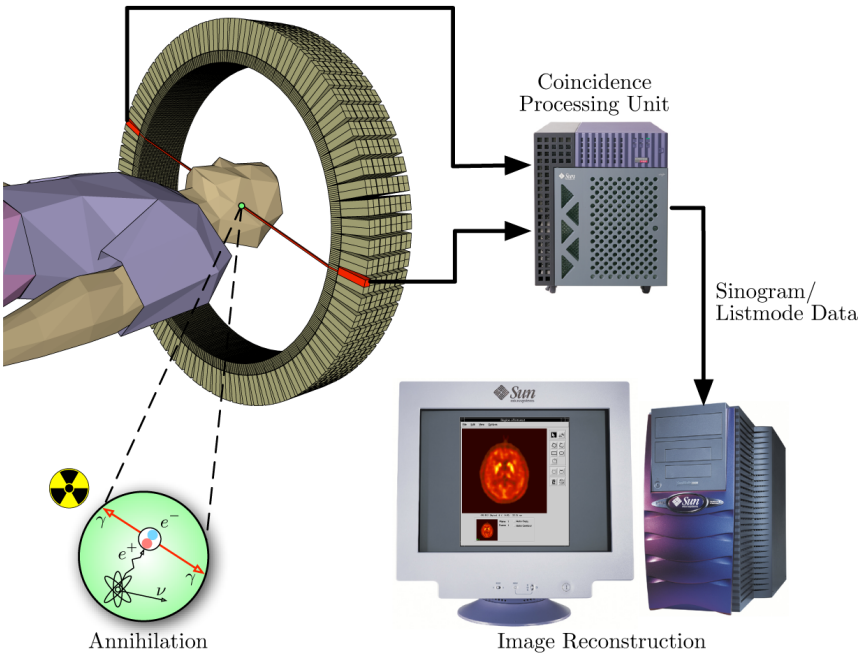

Figure 1.1: Schematic of PET. Picture is taken from [8].

Positron emission tomography (PET) is an imaging technique in the field of nuclear medicine that aims to obtain a three dimensional image of metabolic processes in the body [7]. In figure 1.1 a schematic of a whole body PET detector is shown. A solution containing a radioactive isotope is injected into the body of a human being or an animal, and accumulates in specific regions according to the metabolic processes it might get involved into. The isotope decays by emitting a positron, which in turns after a short path annihilates with an electron and produces two collinear 511 keV gammas rays in opposite directions. These gammas interact with two channels of an array of detectors surrounding the patient, and the energy and timing information are recorded. After coincidence processing, data is sent to a computer that performs image reconstruction. In this chapter the basic physical principles of PET will be discussed, together with the advantages deriving from the inclusion of the Time of flight (TOF) information of the gammas.

1.1 Positron emission

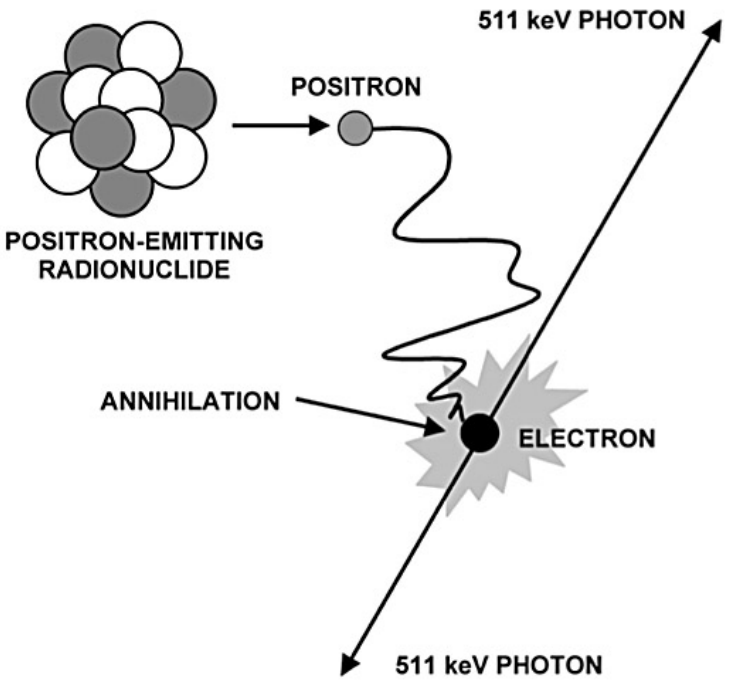

Figure 1.2: Schematic of positron emission and annihilation process. Picture is taken from [7].

The most common isotopes involved in PET are ^{11}C, ^{15}O, and ^{18}F. In particular, a common molecule involved in PET oncology is Fluorodeoxyglucose marked with ^{18}F ($^{18}F - FDG$). It consists in a sugar molecule radiolabeled with by ^{18}F. ^{18}F-FDG, as radioactive sugar, it tends to accumulate in the areas of the body where there is a strong request for energy, and in particular in fast growing cells. After injection into the human body, most of the $^{18}F - FDG$ is absorbed in the cells of brain, kidney and, if present, tumours. The positron is emitted by the F^{18} nucleus via β^+ decay, according to

$$ {}^{A}_{Z}X \longrightarrow {}^{A}_{Z-1}X' + e^+ + \nu_e \tag{1.1} $$

where ${}^{A}_{Z}X$ is the initial nucleus undergoing the decay process, ${}^{A}_{Z-1}X'$ is the final nucleus after the decay process, e^+ is the positron emitted and ν_e is an electron neutrino. The positron then annihilates with a electron and produces two gammas. Because the annihilation happens when the positron is nearly at rest, conservation of momentum imposes that the two gammas are emitted almost collinearly and in opposite directions ("back to back"), as shown in figure 1.2. Furthermore, energy conservation law states that the energy of each of the two gammas emitted is equal to half of the combined rest mass of positron and electron, i.e. 511 keV.

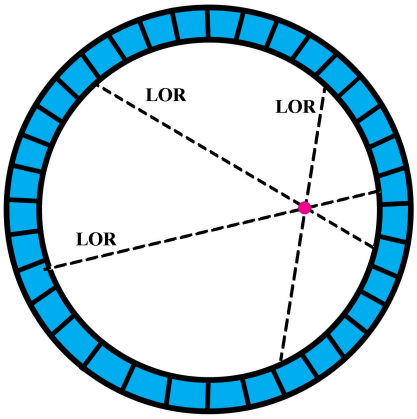

Figure 1.3: Principles of PET. The red point corresponds to a tumour cell.

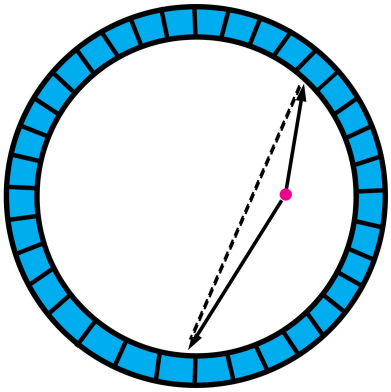

Figure 1.4: Example of a scatter event.

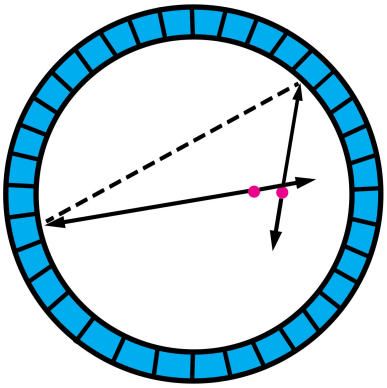

Figure 1.5: Example of a random coincidence event.

1.2 Time of flight PET

1.2.1 Principles of PET

The principle of PET imaging is shown in figure 1.3. A positron emitter places in the area included in a ring of particle detectors. Whenever a positron annihilates, it causes the emission of two back to back gammas. These gammas interact with two detectors of the ring, defining a line of response (LOR). If enough LORs are recorded, the location of the positron emitter can be identified by the intersection point of the LORs. However, before interacting with the detector, the gammas may incur in some interaction with the volume under examination. These events can result in wrong LORs and may lead to a degraded quality of the final image.

One or both of the emitted gammas undergo a Compton scattering in the surrounding tissue. The scattered coincidence leads to an identification of a wrong LOR that does not correspond to the real annihilation position. A schematic representation of a scatter event is shown in figure 1.4. The difference between the scattered and the true coincidence events is

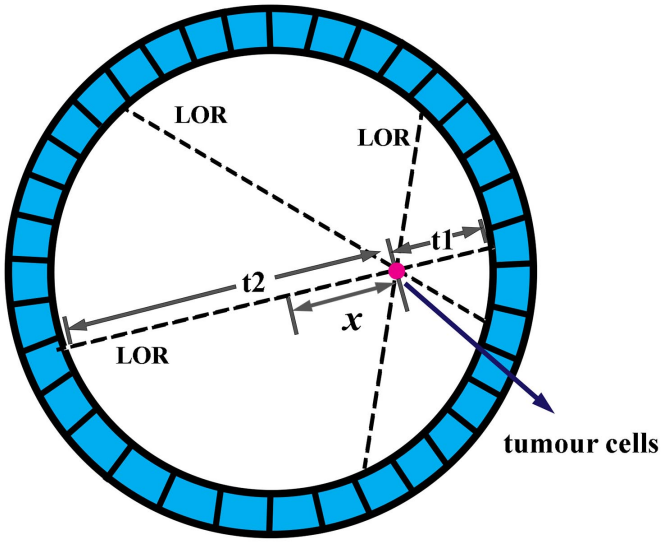

Figure 1.6: Principle of Time of Flight PET.

the energy released in the scintillator. The scattered events lose energy during the interaction with the tissue and so the energy detected is less than the true coincidence events energy. Thanks to a energy threshold, the scattered events can be identified and removed during the image reconstruction. Dedicated algorithms are developed to correct for scattered events [9].

When two unrelated gammas from different annihilation positions are detected in the same coincidence window, a false LOR is reconstructed as shown in figure 1.4. These events are called random coincidence events. The false spatial information carried by the random coincidence events produces background and leads to an incorrect evaluation of the radiotracer concentration. The rate of the random coincidence event is related to the activity of the tracer and to the coincidence time window. The narrower the coincidence time window, the lower the the random coincidence rate.

1.2.2 Time of flight

The position of the annihilation can be identified as the distance x along the centre of the LOR. As shown in figure 1.6, t_1 and t_2 represent the time that the gammas spend to travel from the annihilation point to the detectors. Then x can be expressed as:

$$x = \frac{(t_2 - t_1) \times c}{2 \times n} \tag{1.2}$$

where c is the speed of light and n is the refraction index of the material where the light is traveling. $t_2 - t_1$ is the time difference of two detector recording. Defining Δt the uncertainty of the coincidence time difference, the spatial resolution Δx can be expressed as:

$$\Delta x = \frac{\Delta t \times c}{2 \times n} \tag{1.3}$$

For example, a value of coincidence time resolution (CTR) of 600 ps FWHM corresponds to a spatial resolution of 9 cm while 100 ps FWHM corresponds to the spatial resolution of 1.5 cm.

If the CTR is good enough to reach a high value of spatial resolution, in mm resolution scale, the identification of the annihilation position can be done event by event. Thanks to this process, the image reconstruction can be simplified and the duration of the PET examination can be largely reduced. Patient also benefits that doses from PET procedures are decreased.

In PET scanners, the quality of the reconstructed image depends on the signal to noise ratio (SNR), and the SNR can be improved by including the TOF information. The image quality gain of TOF-PET system compared to a PET that does not include the TOF technique can be expressed as an approximation function [10]:

$$Gain = \sqrt{\frac{D}{\Delta x}} = \sqrt{\frac{2 \times D \times n}{\Delta t \times c}} \tag{1.4}$$

where D is the diameter of the examined volume (dimension of the patient). A CTR of 500 ps FHWM can approximately reach a SNR gain of 2.3 compared to the non TOF-PET system [10]. Figure 1.7 shows the image quality comparison between TOF-PET system with a time resolution of 585 ps FWHM and non-TOF PET system. The reconstruction images using TOF have better quality than non-TOF and the resolution is better.

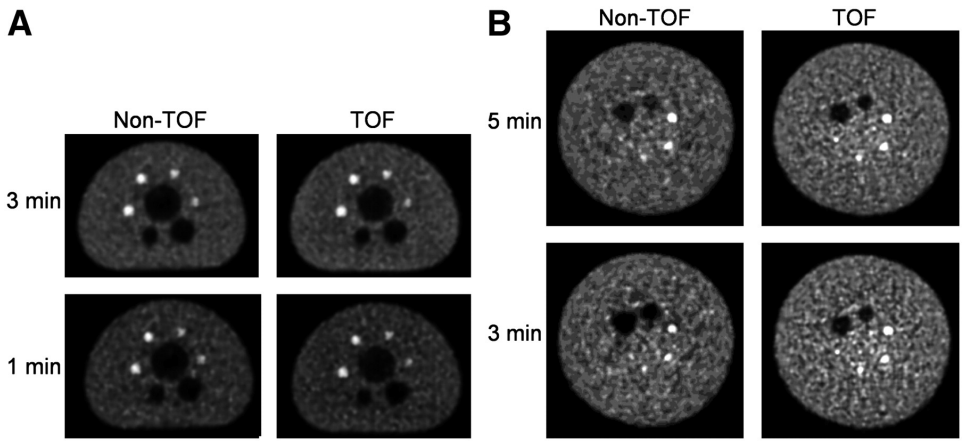

Figure 1.7: (A) Representative slices from reconstruction images of NEMA torso phantom using TOF and non-TOF IRX algorithms for 2 different scan times. (B) Representative slices from reconstruction images of larger phantom with 35 cm diameter using TOF and non-TOF UPenn algorithms for 2 different scan times. 10 iterations of reconstruction are used for the images. [11]

1.3 Scintillation detector

The scintillation detector comprises scintillator, photodetector, processing electronics and readout electronics as shown in figure 1.8. The scintillator absorbs the energy from incident radiation and generates optical photons that are proportional to the energy released in the scintillators. A photodetector collects the output photons from scintillator and generates electrical signals that are proportional to the amount of light. The front end electronics process the signals and then the readout system stores the data for the analysis. The scintillation detectors are widely used in the radiation protection and high energy physics but they are also the key instrument for PET scanners. The components of scintillation detector and operating principle are described in this section.

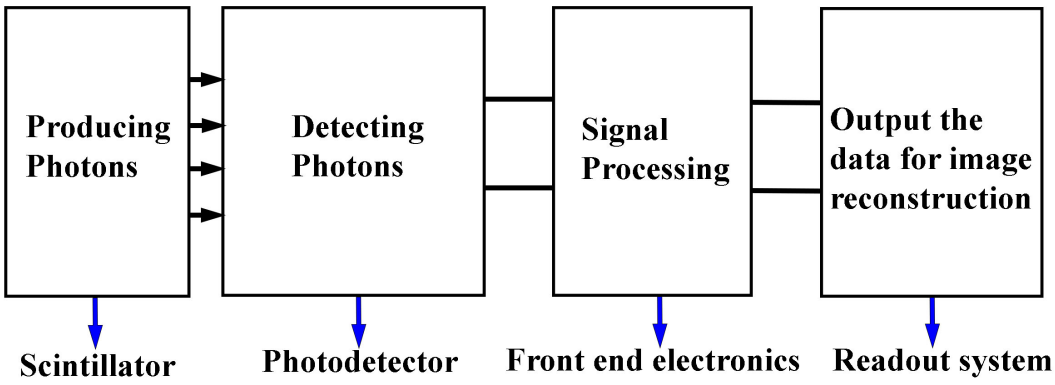

Figure 1.8: Schematic of detector based on scintillation.

.

1.3.1 Scintillator

A scintillator is a material which releases low energy photons when it is excited by ionizing radiation. When a scintillator struck by an incident particle, absorbs its energy and reemits part of the absorbed energy in the form of a small flash of light, typically in the visible range. The scintillators are normally classified into organic scintillators and inorganic scintillators.

Organic scintillator

The organic scintillator has three main types, crystalline, liquid, plastic. All of them generate optical photons from the charged particles ionization. The wavelength of the generated radiation usually goes from the blue to the green wavelength [12]. They have quite fast decay time, typically few nanoseconds or even less. The high light yield and fast time response of the organic scintillator show the potential of the sub-ns timing resolution [13]. However, the organic scintillators have a relative low density and so the low stopping power can not allow to detect particles and high energy radiation in a small dimension scintillator. Therefore, in the PET system, where usually compact components are required, inorganic scintillators with high solid density are more commonly used than organic scintillators.

Inorganic scintillator

In contrast to the organic scintillators, the inorganic scintillators have much higher density (typically from 4 g/cm^3 to 8 g/cm^3). Some inorganic scintillators can produce the scintillating light through its intrinsic luminescence centre, others emitting the scintillating light via doping fluorescent ions. The scintillation mechanism of the inorganic scintillator can be described in the frame of the band theory. Ionization from the incident particles or radiation makes the electrons jump from the valence band to the conducting band. The electrons and holes that are produced in the process can travel through the crystal and be trapped by a luminescent centre. The excited luminescent centre, called activator, returns to the ground state by radiating light. The typical energy range of scintillating photons is around 2-3 eV, which is less than the energy needed to transit an electron from the valence band to the

Table 31.4: Properties of several inorganic crystal scintillators. Most of the notation is defined in Sec. 6 of this *Review*.

Parameter:	ρ	MP	X_0^*	R_M^*	dE^*/dx	λ_I^*	τ_{decay}	λ_{max}	$n^\natural$	Relative output†	Hygro-scopic?	$d(\text{LY})/dT$
Units:	g/cm^3	°C	cm	cm	MeV/cm	cm	ns	nm				%/°C‡
NaI(Tl)	3.67	651	2.59	4.13	4.8	42.9	245	410	1.85	100	yes	−0.2
BGO	7.13	1050	1.12	2.23	9.0	22.8	300	480	2.15	21	no	−0.9
BaF_2	4.89	1280	2.03	3.10	6.5	30.7	650^s	300^s	1.50	36^s	no	-1.9^s
							0.9^f	220^f		4.1^f		0.1^f
CsI(Tl)	4.51	621	1.86	3.57	5.6	39.3	1220	550	1.79	165	slight	0.4
CsI(pure)	4.51	621	1.86	3.57	5.6	39.3	30^s	420^s	1.95	3.6^s	slight	−1.4
							6^f	310^f		1.1^f		
$PbWO_4$	8.3	1123	0.89	2.00	10.1	20.7	30^s	425^s	2.20	0.3^s	no	−2.5
							10^f	420^f		0.077^f		
LSO(Ce)	7.40	2050	1.14	2.07	9.6	20.9	40	402	1.82	85	no	−0.2
$LaBr_3$(Ce)	5.29	788	1.88	2.85	6.9	30.4	20	356	1.9	130	yes	0.2

* Numerical values calculated using formulae in this review.
$^\natural$ Refractive index at the wavelength of the emission maximum.
† Relative light output measured for samples of 1.5 X_0 cube with a Tyvek paper wrapping and a full end face coupled to a photodetector. The quantum efficiencies of the photodetector are taken out.
‡ Variation of light yield with temperature evaluated at the room temperature.
f = fast component, s = slow component

Table 1.1: Properties of the most important inorganic crystal scintillators used in particle detectors [14].

conduction band. So most of the scintillating photons can escape from the crystal avoiding the reabsorption process.

Inorganic crystals have very high light yield and provide good energy resolution down to low energies (few hundred keV) [14]. The properties of several commonly used inorganic scintillators are summarized in Table 1.1.

The thallium activated sodium iodide (NaI(TI)) crystal is a widely used scintillator. Its light yield is quite high and the light emission spectrum is well matched to the working range of the bialkali photomultiplier tubes (PMTs). However, it is hygroscopic and has to be treated carefully.

The CsI(TI) crystal is cesium iodide using thallium as activator. Its density is higher than NaI(TI) and relative higher light yield with slightly hygroscopic. The decay time of CsI(TI) is much longer than NaI(TI). The pure CsI has a short emission time but the light yield is one magnitude order lower than CsI(TI).

The bismuth germanate (BGO) has a high density of 7.13 g/cm^3 and it leads to a good detection efficiency for 511 keV gamma in the PET system. But its slow decay time and low light yield make it not a good candidate for TOF PET imaging.

Lead tungstate ($PbWO_4$) crystals is a fast scintillator and has a short radiation length of 0.89 cm. It is relatively easy to produce from readily available raw materials. It is the densest inorganic scintillator shown in the table. Fast component of decay time of $PbWO_4$

is 10 ns and slow component of decay time is 30 ns. But the intrinsic light yield is quite low compared to other scintillators.

Lutetium oxyorthosilicate (LSO) crystal is consider as a suitable scintillator for the PET system due to the high density and high light yield. Its density is 7.40 g/cm^3. This extremely dense but optically clear property make it ideal for stopping gammas in the PET detector. Lutetium yttrium oxyorthosilicate (LYSO) crystal are similar to LSO which is also a good scintillator for PET imaging.

Cerium doped lanthanum bromide ($LaBr_3$:Ce) has a faster decay time than LYSO. High light yield and good energy resolution with about 2.6% at 662 keV make it become another candidate for PET imaging [15]. However, it is also hygroscopic which requires to avoid moisture.

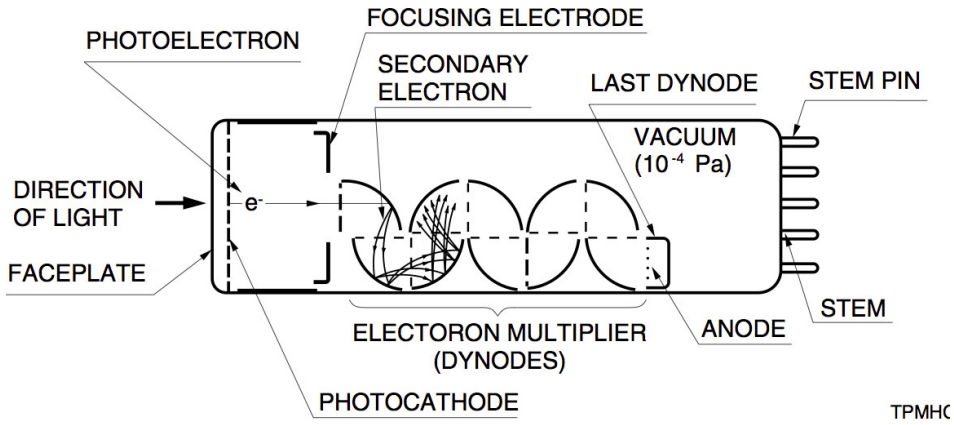

Figure 1.9: Drawing of the head on type photomultiplier tube. Picture is taken from [16].

1.3.2 Photon detector

The visible photons generated by the scintillator are detected by the photodetector which produces a proportional electrical signal. The photon detector can be distinguished into two main technologies: (a) the vacuum photodetectors and (b) the solid state photodetectors. When photons strike the sensitive area of vacuum photodetectors, electrons are ejected from an external photocathode by photoelectric interaction. These electrons are then accelerated in a high electric field and produce secondary electrons by interaction on so called multiplication stages. In solid state photodetectors electron-hole pairs are produced by internal photon interaction in a semiconductor. The produced electron-hole pairs are accelerated in the electric field and multiplied by impact ionization in the semiconductor itself. The avalanche photodiode (APD) and Geiger mode APD (G-APD) also called the silicon photomultiplier (SiPM) are examples of this type of photodetectors. In this section the working principle of both types of photon detector such as the PMT and the SiPM will be described.

Vacuum photodetector

The most widely used vacuum photodetectors are the photomultiplier tube (PMT) and the micro channel plate (MCP). This section is focused on the PMT that has been extensively

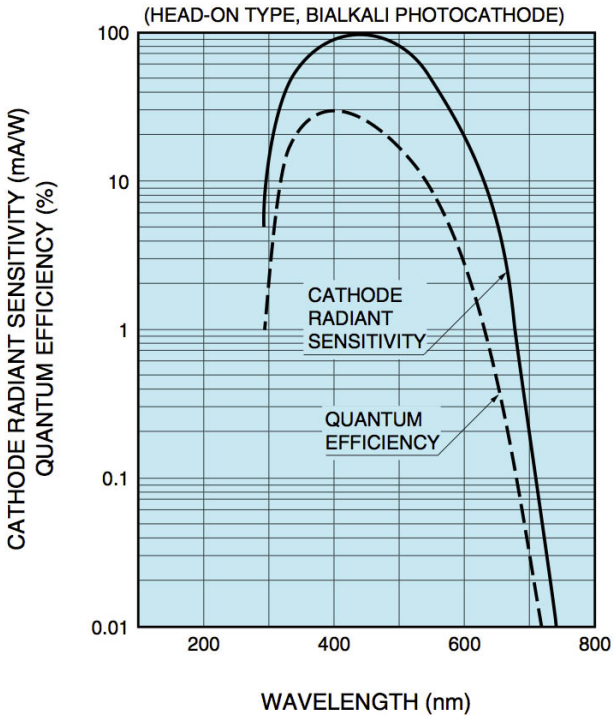

Figure 1.10: Typical response of PMT for different wavelength of light. Plot is taken from [16].

employed in the commercial PET system. The PMT is composed by a photocathode, several dynodes and an anode. Everything is contained by a glass envelope and kept in vacuum condition. Figure 1.9 shows the drawing of an head of a typical PMT. When photons impinge on the photocathode, electrons are emitted by the photocathode material due to the photoelectric effect. The emitted electrons are focused by a focusing electrode and accelerated to the first dynode by the electric field. The electrons that reach the kinetic energy of a few hundred electron volts impact on the dynode producing more low energy electrons. The same multiplication process happens for each dynode. The number of electrons collected by the anode is from 10^4 to 10^8. The gain of a PMT is a function of the applied high voltage V as [14]:

$$Gain = A \times V^{kn} \tag{1.5}$$

where A is a constant, k is another constant that depends on the dynode material, and n is the number of dynodes in the PMT. The high voltage for PMT goes from 1000 V to 3000 V. There are some signals generated in the PMT even in case of no light. This dark noise is caused by the thermal emission of electrons from the photocathode. The noise performance of PMT is normally represented as the dark count rate. Typical dark count rate of PMT is in the order of 100 to 1000 Hz.

The quantum efficiency (QE) is a main feature of the PMT. The QE represents the ratio between photoelectrons number ejected from the photocathode and the number of incident photons. The QE of PMT depends on the material of the photocathode and it is strongly related to the wavelength of the incident light. Figure 1.10 shows a typical response of Hamamatsu photomultiplier tube. The maximum QE value of PMTs is about 20-30 %, some PMTs can reach 40 %.

Solid state photodetector

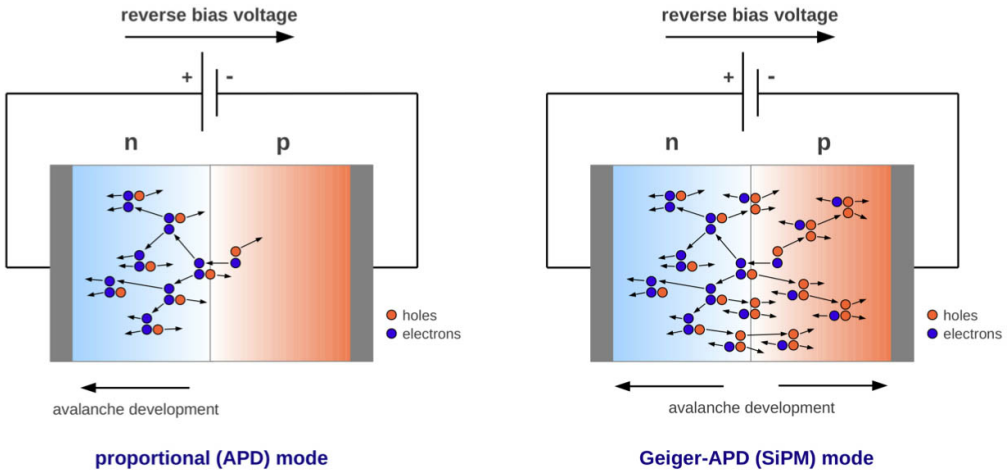

Figure 1.11: Left plot: Drawing of the avalanche process in APD. Right plot: Drawing of the Geiger-mode avalanche development. Picture is taken from [18].

Compared to the traditional vacuum photodetectors, solid state photodetectors are more compact, insensitive to the magnetic field and the operational voltage is lower. The basic component is a photodiode with a p-n structure [17]. If the energy of the photons that strike the detector is high enough, electron-hole pairs are created as a consequence of photoelectric effect. A current is produced by collecting the holes in the anode and electrons in the cathode. The current is quite low and is proportional to the number of photons absorbed. To detect low light flux, the signal of photodiode needs to be amplified because there is no internal gain.

The avalanche photodiode (APD) is another type of solid state photodetector. The gain of this device is higher gain thanks to the increase of the reversed bias voltage of the p-n component. The photoelectron produced by the incoming photon is accelerated to high energy in the electric field that is applied between the anode and the cathode of the junction. The first electrons produced continue to gain energy in the high electric field and further electron-hole pairs are generated. This process is repeated many times and generates the avalanche. A plot showing the avalanche process in the APD mode is depicted in figure 1.11. In APD, most of the holes created do not gain enough energy to generate additional electron-hole pairs and so only electrons participate to the multiplication process. The typical gain of APD is 10^2 to 10^3.

The Geiger mode APD is a device that can detect single photon as a PMT that operates at very high gain. It is also referred as single photon avalanche photodiode (SPAD). The Geiger mode of the silicon photodiode is obtained by increasing the reverse voltage above the voltage level called breakdown voltage. As shown in figure 1.11 the high electric field in the junction is enough to make the electron-holes multiplication process become self sustain and both electrons and holes are involved in the avalanche development [19]. However, in the Geiger mode, the device does not turn off by itself. A high ohm value resistance or a quenching circuit are needed to stop the avalanche process. Several SPAD devices can be grouped on the same silicon substrate and such a device is called silicon photomultiplier

(SiPM). The details of SiPM is introduced in chapter 3.

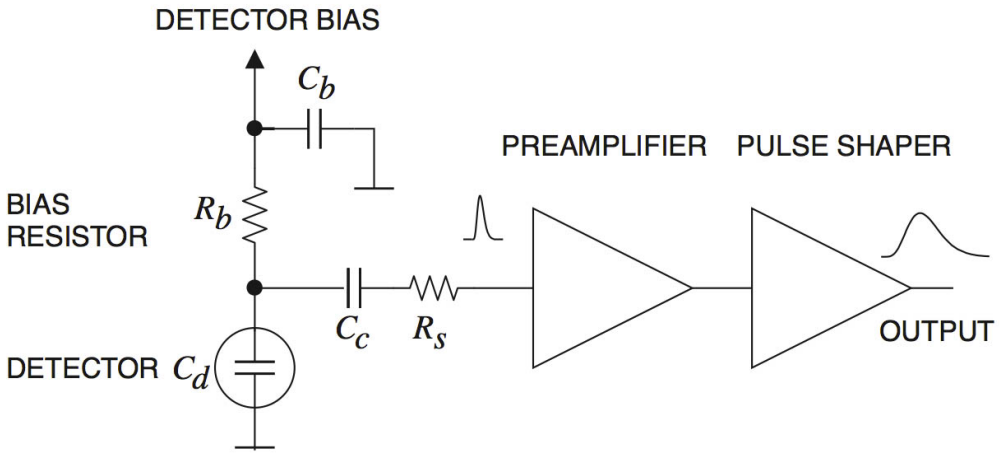

Figure 1.12: A typical design of a front end circuit for scintillation detector. Picture is taken from [14].

1.3.3 Front end electronics

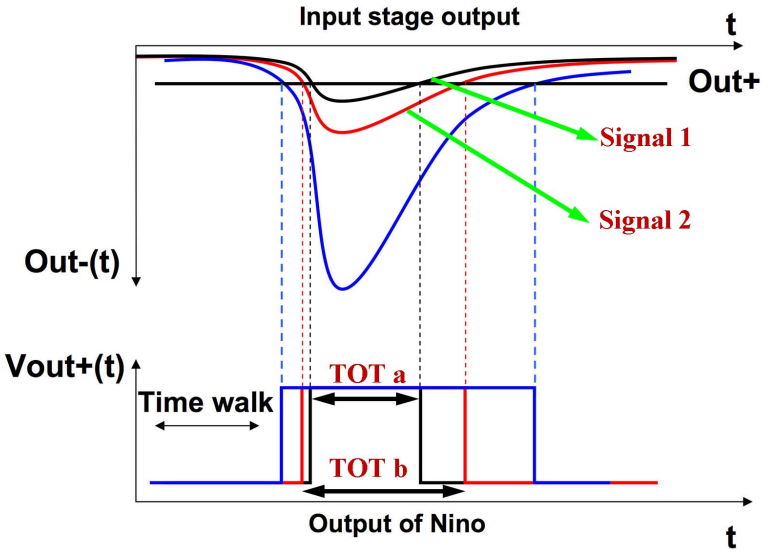

Figure 1.13: A typical plot of Time over Threshold method. Plot is modified from [21].

Before being sent to the readout system, the signal from photodetectors is elaborated by a signal shaper or amplifier. Indeed the direct output of the detectors need to be amplified to increase the SNR and also to be easily read out. The front end electronics perform the amplification and discrimination processes. The performance of the whole detector system relies a lot on low-noise electronics and a low detection threshold to trigger on the 1 photoelectron level. Figure 1.12 shows a typical drawing of a front end circuit. The signal from photode-

tector firstly is amplified with a preamplifier and sent to a pulse shaper which moderates the signal to optimize the SNR for the readout chain.

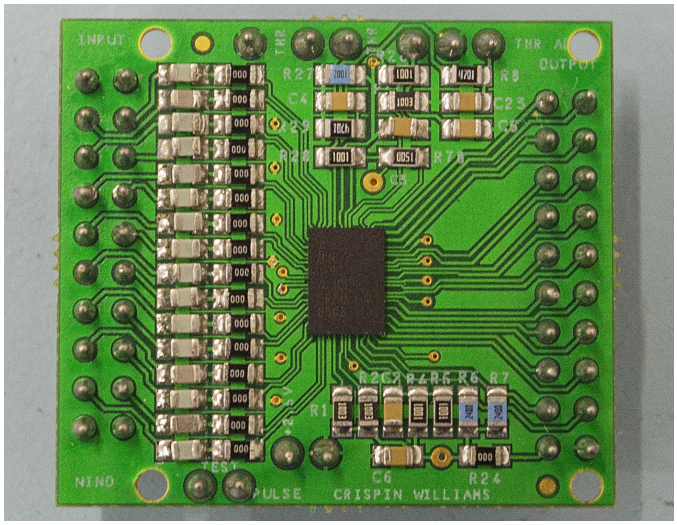

Figure 1.14: Picture of eight channel NINO ASIC.

Time over threshold

Time-over-threshold (ToT) is a technique to convert an input charge into a digital pulse. This process is done recording the time duration which the signal is above a preset threshold level [20]. As shown in figure 1.13, the ToT pulse width is the time difference between the rising edge of signal and falling edge of signal cross the set amplitude threshold. For example, ToT_a is the output of signal 1, ToT_b is the output of signal 2. The leading edge of the output signal can be recorded by the TDC for the time information of the event and the energy information can be extracted from the total length of the ToT pulse. The output time pulse is not linearly proportional to the charge input, so the ToT method has less precision in the energy measurement compared to the charge integration method. However, the ToT gives both time information and energy information together. Thanks to this electronics, the cost of the PET system can be reduced and the PET detector can be simplified by only using time to digital convertor (TDC) to readout the ToT output pulse.

NINO ASIC is a ultra fast preamplifier discriminator based on ToT and developed for the Multi-gap Resistive Plate Chamber (MRPC) of ALICE experiment [22], [23]. The chip has eight channel and is fabricated with 0.25 μm Complementary Metal-Oxide-Semiconductor (CMOS) technology. A picture of NINO ASIC chip is shown in figure 1.14. A differential circuit is used for the input and output signals. In particular the output signal is compatible with the Low Voltage Differential Signalling (LVDS) receiver [24]. The NINO implemented in the TOF-MRPC detector of the ALICE Experiment has achieved a timing precision of less than 60 ps FWHM [25]. NINO has also shown a good timing performance as an amplifier-discriminator for the scintillation detectors. With $2 \times 2 \times 3mm^3$ LSO:Ce codoped 0.4%Ca crystals coupled to the Hamamatsu multi-pixel photon counters (MPPCs) (S10931-050P), a CTR of 108±5 ps FWHM has been achieved using a NINO ASIC [26].

1.3.4 Readout system

The readout of the signal records both the energy information and the time information. The energy information can be extracted either as the area of the signal or as the amplitude of the signal. A charge sensitive electronics uses an integrator like charge-to-digital converter (QDC) that integrates the charge in a defined time window. The most simple way to extract the time information is to use a leading edge discriminator that produces a pulse when the input signal cross a predefined threshold. Thus the pulse is recorded with TDC as the time of the incoming signal.

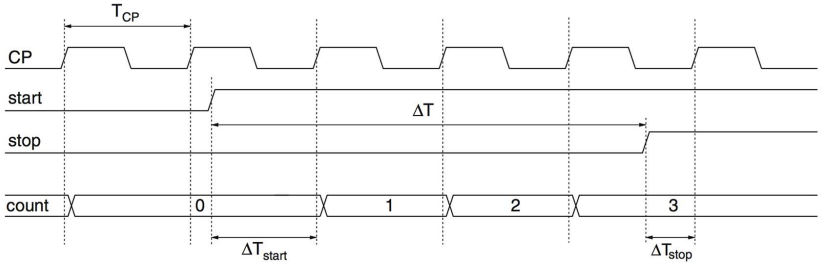

Figure 1.15: The principle of the counter based TDC. Picture is taken from [27].

The time to digital converter is a device that recognizes the arrive time and stop time of the incoming pulse, measures the time interval of the pulse and outputs a digital counter. The most simple TDC based counter is shown in figure 1.15. The T_{CP} is the reference clock period and it is represented as a complete oscillation. The start time measured T_{start} is determined at the rising edge of reference clock while the start signal is at high level. As the same, the stop time measured T_{stop} is determined at the rising edge of reference clock while the start signal is at high level. As indicated in the figure, the measurement error ΔT_{start} is the time difference between the rising edge of the start signal and T_{start}. The time interval Δ T can be expressed as [27]:

$$\Delta T = N \times T_{CP} + (T_{CP} - \Delta T_{stop}) - (T_{CP} - \Delta T_{start}) \tag{1.6}$$

which can be simplified to

$$\Delta T = N \times T_{CP} - \Delta T_{stop} + \Delta T_{start} \tag{1.7}$$

The error of the time interval is $\Delta T_{start} - \Delta T_{stop}$ which is in the range of -T_{CP} to T_{CP}. As the measurement accuracy depends on the reference clock, the resolution of the TDC can be improved by increasing the clock frequency.

The TDCs are widely used in the high energy physics with high timing precision. The High Performance general purpose TDC (HPTDC) is an high precise device, developed by the CERN electronics group [28]. The HPTDC gives the relative time information of each hit signal at the external trigger signal arrival. The architecture of HPTDC chip is shown in figure 1.16. The HPTDC is based on a Delay Locked Loop (DLL) with a delay chain and a Phase Locked Loop (PLL) to perform clock multiplication [29]. The main part of DLL is a delay chain including 32 delay elements that can be changed by a control voltage. Each delay element can receive the input signal from clock and generate a clock output signal with a shift phase from the input signal. The internal clock frequency is 40 MHz, which can be increased

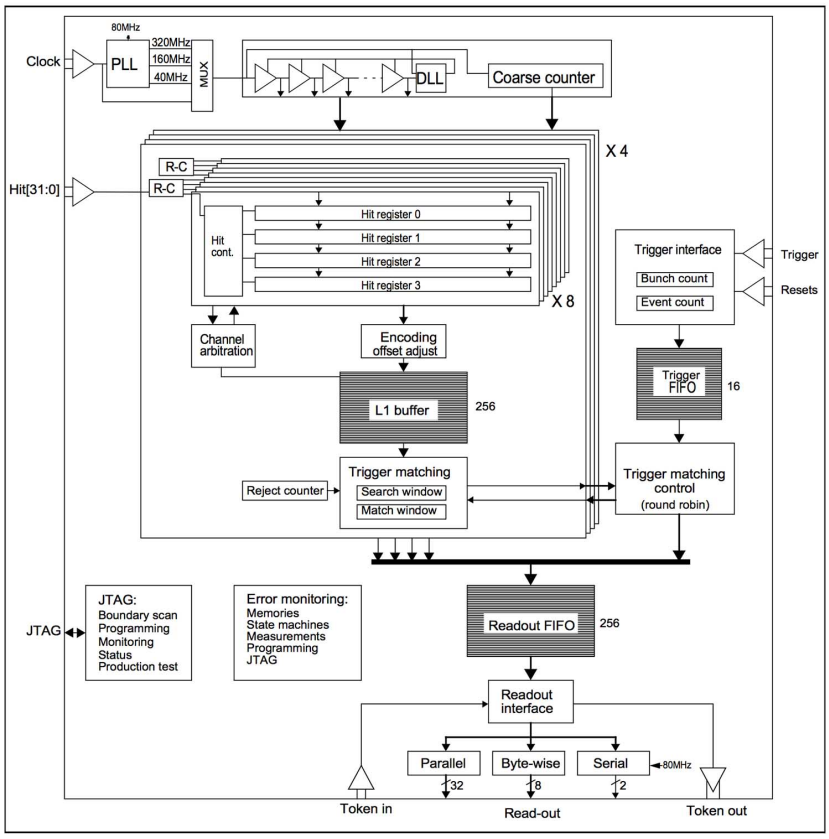

Figure 1.16: The architecture of HPTDC chip. Picture is taken from [28].

to 160 MHz or 320 MHz with PLL. The best time resolution using 320 MHz clock frequency with DLL is 98 ps. In the very high resolution mode, 24.4 ps bin size can be achieved with four channels combined into one channel on the chip [30]. Such a good time resolution is realized by using a precisely calibrated R-C delay line shown in figure 1.17. The incoming sampling pulse is delayed in 25 ps, 50 ps, 75 ps and 100 ps respectively. The delayed four pulses are sent to four different channels and sampled by the TDC, giving a sampling time resolution of 25 ps bin size.

1.4 EndoTOFPET-US detector

Pancreatic cancer has a very difficult prognosis and also, after the diagnosis, only 5% of people survive for five years [31]. For most of the patients, the lesion is diagnosed only during the late stage of the disease. The early detection of the pancreatic cancer becomes very important and can increase the survival rate. Prostate cancer is another cancer which is the most common cancer for men. There is a big chance that the prostate cancer can be healed if it is detected in the early stage of development [32]. For the diagnosis of pancreatic and prostatic cancers, endoscopic ultrasonography is a quite common tool. Using a combination of ultrasonic endoscopic probe and PET technique,the benefits are a shrinkage of the region of interest and also a better imaging quality thanks to the reduction of background from

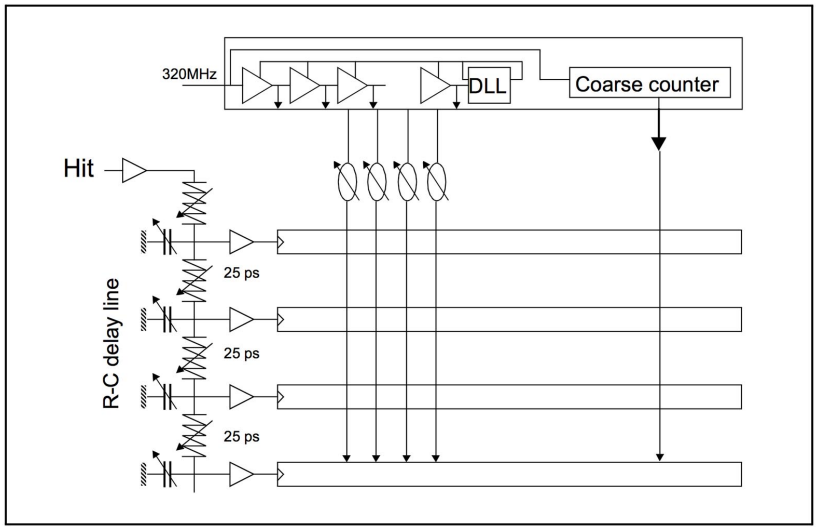

Figure 1.17: The principle of R-C delay line for HPTDC. Picture is taken from [28].

other organs. This kind of device can have high probability to detect early stage cancer and reconstruct the lesion area with a high resolution. The EndoTOFPET-US collaboration proposed a prototype detector that combine Endoscopic Time-Of-Flight Positron Emission Tomography and Ultrasound.

As shown in figure 1.18, on the left there is a miniaturized PET head together with a commercial ultrasound endoscope. On the right, the external plate for PET detector is shown. Both the PET head and the external plate are in coincidence to detect the two back to back photon originated by the positron annihilation. The external PET detector consists 256 matrices of 4×4 LYSO crystals with size of $3.5 \times 3.5 \times 15\ mm^3$, coupled to 256 Hamamatsu TSV-MPPC arrays (S12643-050CN). These 256 MPPC arrays are placed in a data acquisition system that consists in 8 parallel front-end boards (FEB), each one hosts 8×64 channel readout ASICs [33]. The sequence of the assembly of this external plate is shown in figure 1.19. Details of the characterization of the components for external plate are presented in chapter 4.

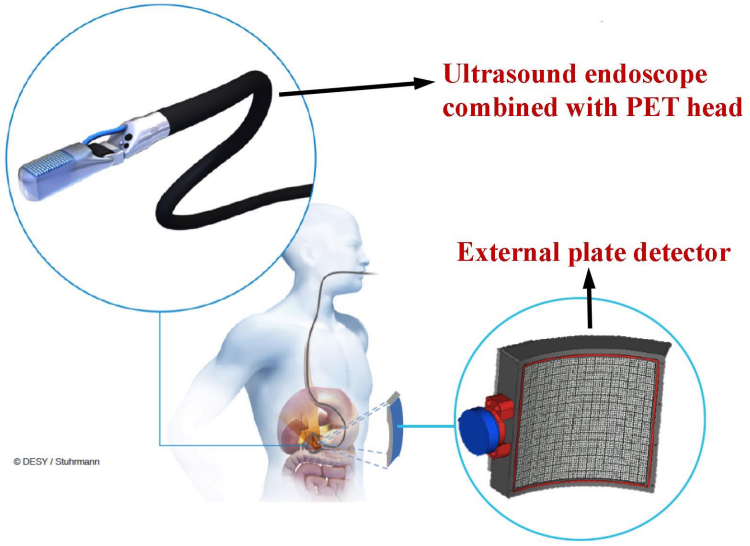

Figure 1.18: The EndoTOFPET-US detector system. The left is a miniaturised PET head together with a commercial ultrasound endoscope. The right is a external plate detector outside of the patient opposing to direction of the PET detector head.

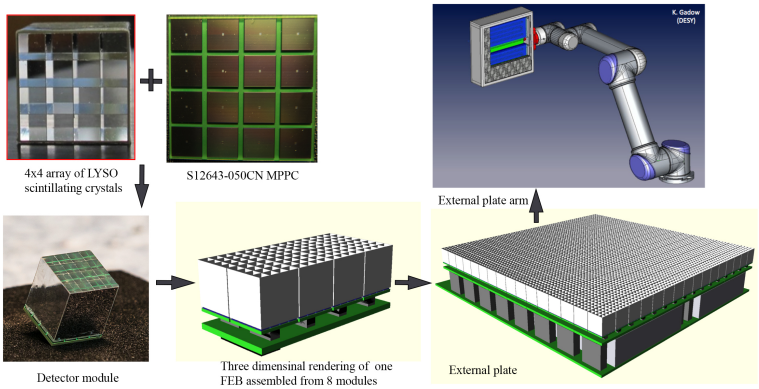

Figure 1.19: The external plate composition of EndoTOFPET-US detector system.

Chapter 2

Silicon photomultiplier

The silicon photomultiplier (SiPM) consists arrays of single photon avalanche photodiodes (SPADs) operating in the Geiger-mode. Figure 2.1 shows a structure of one type of SiPM. Hundreds or thousands SPAD cells are connected together with a common voltage input. The signals from the different SPADs are routed out from the same connecter. The Geiger avalanche process is stopped by the drop of the voltage below the breakdown voltage due to the quenching resister. Typical cell size of the SiPM are 25 $\times$ 25 μm^2, 50 $\times$ 50 μm^2, or 100 $\times$ 100 μm^2, etc. Figure 2.2 shows a picture of SiPM with cell size of 50 μm. The most important properties of SiPM are described in this chapter.

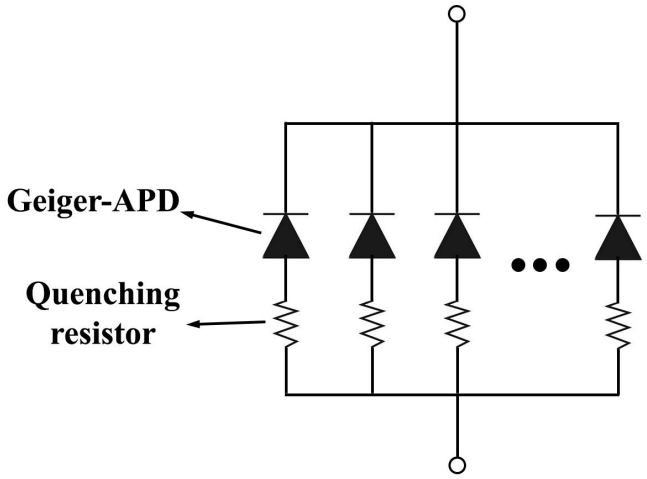

Figure 2.1: Typical structure of a SiPM.

2.1 Basic characteristics of silicon photomultiplier

2.1.1 Breakdown voltage

As described in the first chapter, the breakdown voltage is the boundary of reverse voltage between the avalanche photodiode (APD) mode and Geiger mode of the p-n junction. The breakdown voltage can be defined as the reverse voltage which makes the generation rate

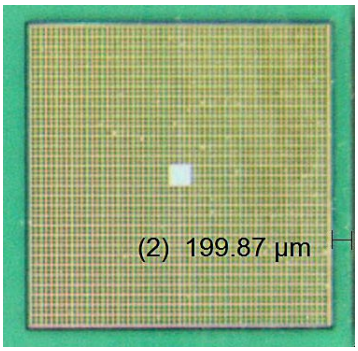

Figure 2.2: Microscopic picture of a multi-pixel photon counter (MPPC) (S12643-050CN) from Hamamatsu.

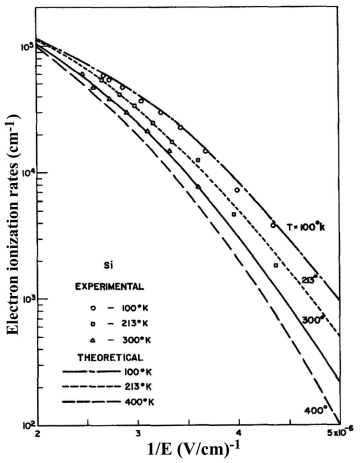

Figure 2.3: . Electron ionization rate as function with electric field at different temperatures. Picture is modified from [35].

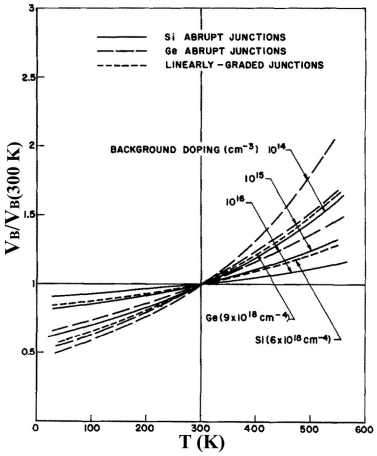

Figure 2.4: Normalized breakdown voltage as a function of temperature for different doping concentrations. Picture is modified from [35].

of electron-hole pairs equal to the extraction rate of charge in the device. The breakdown voltage of SPAD is varying with different design parameter of the SPAD such as the doping profile, or the technology used. For example, SiPM produced from Hamamatsu (also called MPPC) has a breakdown voltage from 50 V to 70 V while the SiPM produced from the AdvanSiD has a breakdown voltage from 20 V to 30 V [34].

Additionally, the breakdown voltage depends on the temperature. Some attempts to analytically describe the change of breakdown voltage with temperature variation have been performed in [35], [36]. The charge carriers's ionization rate changes with different temperatures as shown in figure 2.3. Since the charge carriers have less rate of impact ionization and production of new electron-hole pairs at higher temperature, a higher bias voltage is needed for creating stronger electric field. A predicted result of breakdown voltage vs temperature for Si and Ge p-n junctions is shown in figure 2.4 [35].

The breakdown voltage gives the reference of the operating voltage. The performance for the silicon photomultiplier is strongly dependent on the over breakdown voltage (or over

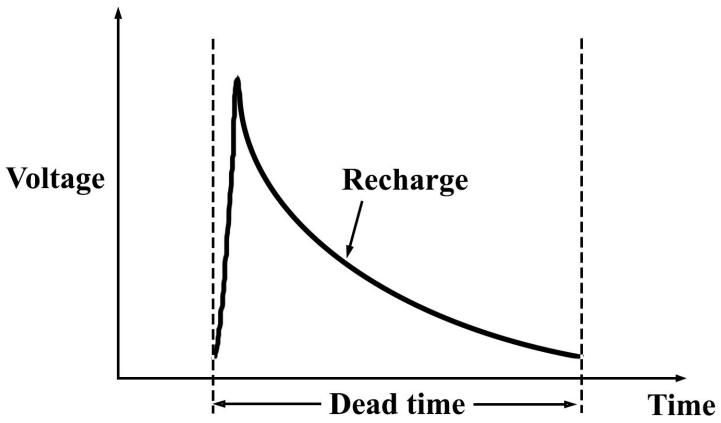

Figure 2.5: Typical signal of a SPAD.

voltage). In large detector system, hundreds to thousands SiPM devices are used. The operating voltage for each SiPM device should be adjust according to its breakdown voltage to optimise the performance of the detector. In case of no current-limiting circuitry is provided for the SiPM, the device can be damaged with too high over bias voltage by thermal effects.

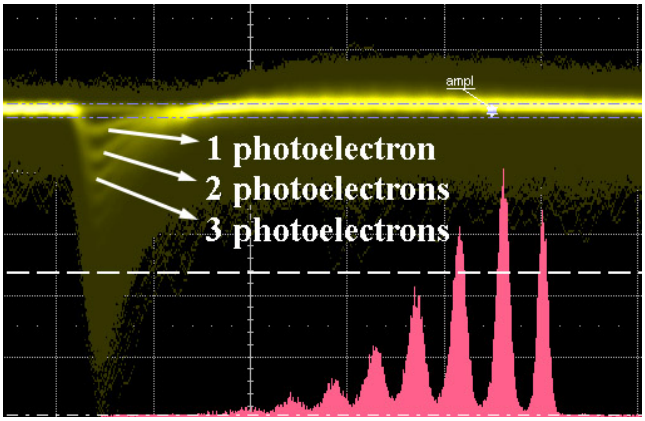

Figure 2.6: Oscilloscope picture of the signal from Hamamatsu MPPC (S10931-050P).

2.1.2 SPAD quenching

With a reverse voltage above the breakdown voltage, every SPAD of the SiPM is operated in Geiger mode. Once the SPAD is triggered, the avalanche process can be self-sustained. Thus the SPAD is no longer able to detect further photons. The avalanche current in the multiplication region of the SPAD needs to be quenched to stop the avalanche. A quenching circuit is designed to terminate the avalanche process with two main function: to reduce the voltage across the junction so that the avalanche process stops and to restore the voltage of the SPAD back to the initial state.

One typical circuit is obtained with a passive quenching. This circuit includes a resistance in the range between 100 kΩ to 1 MΩ, as shown in figure 2.1. When no avalanche is triggered, the added quenching resister does not affect the applied voltage across the junction. After the detection of one photon, a voltage drop is developed across the quenching resistor due to the avalanche current that flows through it. This leads to a reduction of the voltage in the diode, and of the avalanche current, with less and less charge carriers go through the multiplication region. It is possible to show that the avalanche process terminates when the the current in the diode drops below a latching current [37]. The SPAD is recharged when the avalanche finishes. When the voltage applied to the SPAD goes above the breakdown voltage the device is ready to detect another photon. The recharge time is dependent on the resistor and capacitance and can be expressed as [37]:

$$\tau_{recharge} = R_{quench} \times (C_{diode} + C_{stray}) \tag{2.1}$$

where $\tau_{recharge}$ is the time constant of the recharging time, R_{quench} is the value of the quenching resistor, C_{diode} is the capacitance of the diode and C_{stray} is the stray capacitance (capacitance to ground of the diode terminal connected to quenching resistor).

An example of the operation cycle for the SPAD is shown in figure 2.5. The signal of the SPAD rises up immediately after the avalanche breakdown and then decreases exponentially. The time period of the quenching process and the recharge represents the dead time of the SPAD since it can not count other photons.

2.1.3 Gain

The SiPM outputs a standard signal in case of an avalanche process is triggered by one or more photons. The gain of the SiPM can be defined as the ratio of total charge output to the charge sum of photoelectrons triggering the avalanche, which is simply expressed:

$$Gain = \frac{Q_{single}}{q} = \frac{C_{SPAD} \times (V_{bias} - V_{BD})}{q} \tag{2.2}$$

where Q_{single} is the output charge of SiPM when only one SPAD is triggered, q is the charge of electron, C_{SPAD} is the capacitance of the SPAD, V_{bias} is the bias voltage, and V_{BD} is the breakdown voltage. The typical gain of SiPM varies from 10^5 to 10^6. Figure 2.6 shows the output of the Hamamatsu MPPC (S10931-050P) on the oscilloscope. The signal amplitude of 2 photoelectrons is twice the one of 1 photoelectron.

A typical plot of gain as function of the bias voltage is shown in figure 2.7. As indicated in the equation 2.2, the gain is linearly proportional to the over bias voltage. The breakdown voltage can be estimated as the value of the voltage where the gain is equal to zero.

2.1.4 Photon detection efficiency

The Photon Detection Efficiency (PDE) of SiPM is the probability that an incident photon triggers an avalanche breakdown. The PDE can be expressed as the combination of three factors:

$$PDE = FF \times QE \times P_{trigger} \tag{2.3}$$

where FF is the geometric fill factor of the SiPM, QE is the quantum efficiency and $P_{trigger}$ is the probability of avalanche triggering.

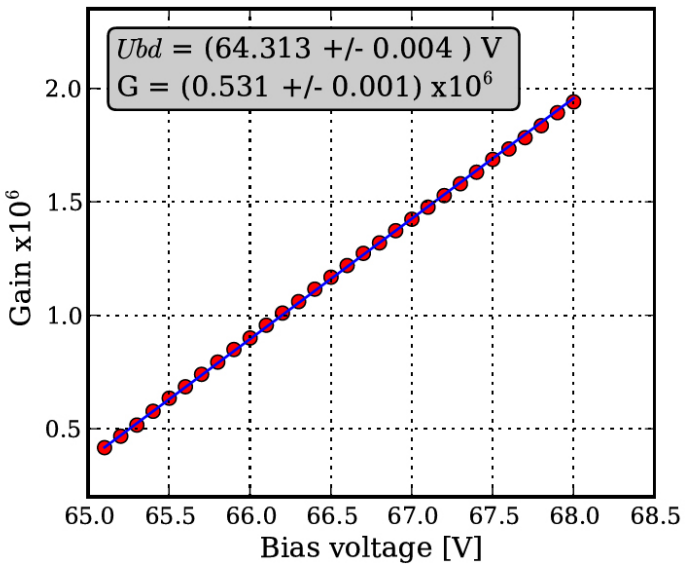

Figure 2.7: Gain as a function of the bias voltage for MPPC (S10931-050P). The line is a linear fit to the data points whose errors are within the symbol. Plot is taken from [38].

The geometric fill factor is the ratio of the active area to the total area of the SPAD. Besides the area for detecting photons, some space is used for the separation of each SPAD and for the electronics circuit. The fill factor depends on the design of the SiPM, such as the SAPD shape, size and the technological routing of the electronics. Generally, the smaller the SPAD size, the lower the fill factor. The typical fill factors are in the range 30% to 70%. The quantum efficiency describes the number of electron-hole pairs generated per incident photon. As for PMTs, the quantum efficiency of SiPM is also wavelength dependent. The Probability of the avalanche generation depends on the position where the primary electron-hole pair is created and on the strength of the electric filed. Thus the probability of avalanche triggering can be increased with higher over bias voltages.

Figure 2.8 shows a plot of PDE as a function of wavelength. The highest PDE for this SiPM is 32.5% at 4 V over bias voltage in the wavelength of 550 nm. The PDE sensitivity of wavelength depends on the structure of the SPAD. For example, a p-on-n structure will be more sensitive to short wavelength of light. As shown in figure 2.9, the blue light (short wavelength) has a high probability to be absorbed in the very thin p-layer in the top of the structure. The electrons generated will be accelerated by the high electric field to the p-n junction with high probability to trigger an avalanche breakdown. Thus the PDE reaches high value with the blue light. On other hand, most of the red light (long wavelength) will be absorbed in the p-layers at the bottom of the p-n junction. The holes generated toward the junction have lower probability to trigger the avalanche breakdown which results into a low PDE value for the red light. Another structure is the n-on p structure, as shown in the right side of figure 2.9. Most of the red light absorbed in p-layer gives higher trigger probability than the blue light. The n-on-p structure has a higher PDE with red light region.

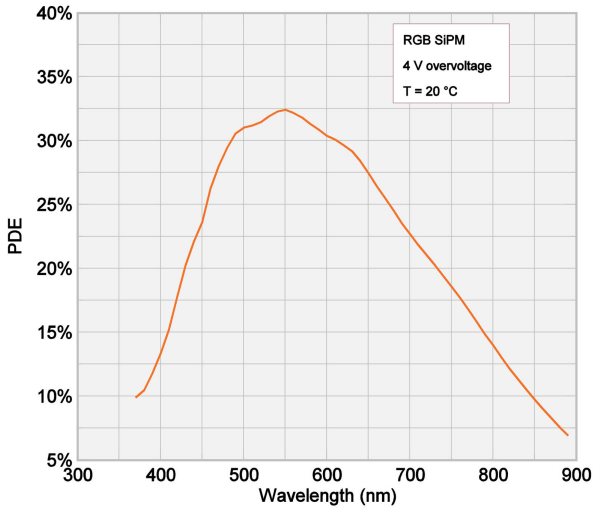

Figure 2.8: PDE as a function of wavelength. The SiPM is AdvanSiD RGB-SiPM. Plot taken from [39].

2.1.5 Dark noise

The avalanche process can also be triggered by electron-hole pairs generated by thermal effect, or field-assisted generation electrons [40]. Since these signals are created in the absence of impinging light, they are called "dark noise". The dark count rate (DCR) is used to describe the noise performance of the SiPM. The DCR value is often quoted for a threshold of half the single photon amplitude. The typical DCR value of latest SiPM is in the range from 100 kHz to 1 MHz per mm^2 at 20 $°C$.

The DCR is strongly temperature dependent. In fact the probability of thermally generated electron-hole pairs can be expressed as a function of temperature [41]:

$$p(T) = CT^{\frac{3}{2}} e^{(-\frac{E_g}{2k_B T})} \tag{2.4}$$

where C is a constant depending on the SiPM material and its technological parameters, T is the temperature in Kelvin, E_g is the band gap energy and k_B is the Boltzmann constant. The DCR of a SiPM can be decreased by working in lower temperature condition. The DCR value is reduced by 3 orders of magnitude when varying the temperature from 293 K to 100 K [42]. Additionally, the field-assisted generation related dark noise can be reduced by decreasing the over bias voltage. However, the PDE and the gain are also lower with a smaller over bias voltage.

2.1.6 Optical crosstalk

In the avalanche process, photons generated by the hot carriers may penetrate the neighbour SPAD and trigger another avalanche [43]. This effect is referred to optical crosstalk. The photon can travel to the neighbour SPADs with a direct optical path or be reflected in the bottom of the silicon substrate to another SPAD. A simplified representation of optical crosstalk is shown in figure 2.10. An estimate of the number of photons created is three photons per 10^5 avalanche electrons [45]. As shown previous, as the higher the over bias

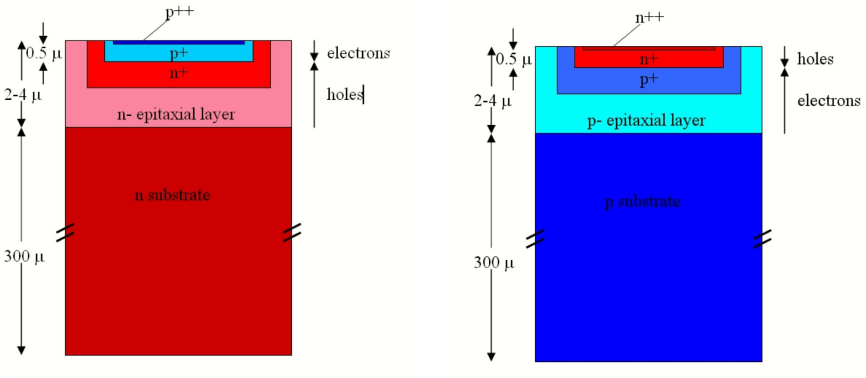

Figure 2.9: A schematic view of two types structure of for a SPAD. On the left is the so-called p-on-n structure (predominantly blue- sensitive) and on the right is the n-on-p (predominantly red-sensitive) structure. Picture is taken from [19].

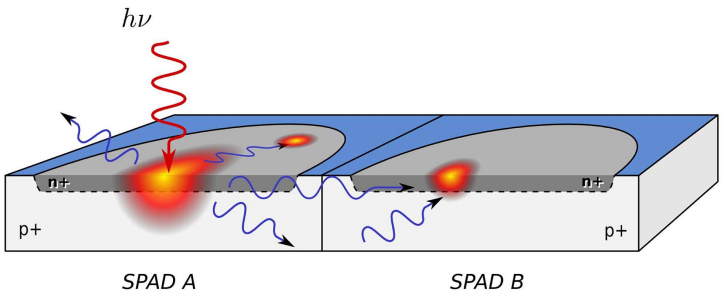

Figure 2.10: Schematic representation of optical crosstalk between two SPAD cell A and SPAD cell B. When a external photon triggers an avalanche in the SPAD cell A, some internal photons are emitted from the avalanche. These photons propagate through the bulk of the array and finally they trigger another avalanche in the SPAD cell B. Picture is taken from [44].

voltage, the higher the gain of the SiPM, so the crosstalk probability is strongly related to the over bias voltage of the SiPM. Most of the optical crosstalk is due to red or infrared photons, since they can travel longer distance in the SiPM without being absorbed. There are some models to describe the crosstalk [44], [46].

The crosstalk probability of the SiPM is normally calculated as:

$$P(ct) = \frac{DCR_{1.5p.e.}}{DCR_{0.5p.e.}} \tag{2.5}$$

where the $DCR_{1.5p.e.}$ is the dark count rate with a threshold at 1.5 photoelectron level and $DCR_{0.5p.e.}$ is the dark count rate with a threshold at 0.5 photoelectron level.

The crosstalk increases the noise and the excess noise factor, thus degrading the performance of the SiPM. To reduce the crosstalk, one can operate the SiPM at lower over bias voltage. As shown in figure 2.11, the crosstalk probability increases as a function of the over bias voltage. However, the low over bias voltage also results into a lower gain and a low PDE. To optimise the performance of the SiPM, a balance between the different parameters

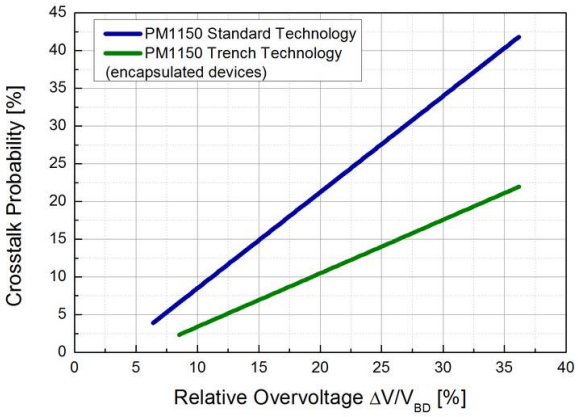

Figure 2.11: Optical crosstalk probability as a function of the over bias voltage. The SiPM type PM1150 is produced by KETEK standard technology and KETEK trench technology which used to reduce the crosstalk. Plot is taken from [47].

is important. Another way to reduce the crosstalk is using some structure design to provide optical isolation between the SPAD cells, like optical separation cell trench [48]. For example, the crosstalk of KETEK PM1150 SiPM is reduced significantly by using the KETEK trench technology instead of the standard technology as can be seen from figure 2.11. The drawback of this optical isolation is the PDE reduction due to the lower fill factor.

In the application, the SiPM will be optically coupled with scintillator. It has been shown that the optical crosstalk can be increased by the coupling of scintillator [49]. In fact in the absence of the scintillator, the photons emitted from the avalanche can escape through the SiPM surface to the air without being reflecting back to the SiPM. By placing a scintillator in front of the SiPM, these photons travelling to the surface of SiPM will be potentially reflected back to the SiPM, increasing the crosstalk probability. It is also found that the optical crosstalk amplification due to the coupling with the scintillator is one important factor limiting the timing performance of the detector [49].

2.2 Digital silicon photomultiplier

A SiPM consists of an array of SPADs operated in Geiger mode and capable of detecting single photon and multi photons. A typical structure of analog SiPM is shown in figure 2.12 (a). Thanks to the development of modern semiconductor technology, the complementary metal-oxide-semiconductor (CMOS) electronics can be integrated on the SiPM chip, resulting in a fully digital readout [51]. This SiPM is often called digital SiPM, which utilises the digitalization of the SPAD signal, inhibiting high noise SPADs, direct time to digital convertor (TDC) readout and digital trigger logic. As the most of electronics are built on the chip, the detector system can be simplified and more compact. The individual single SPAD readout of digital SiPM gives the possibility to measure the light spatial distribution on the SiPM surface.

In a full digital SiPM, the signal of each SPAD cell is digitized and its time information can be recorded with an individual TDC. The concept of this ideal digital SiPM is shown in

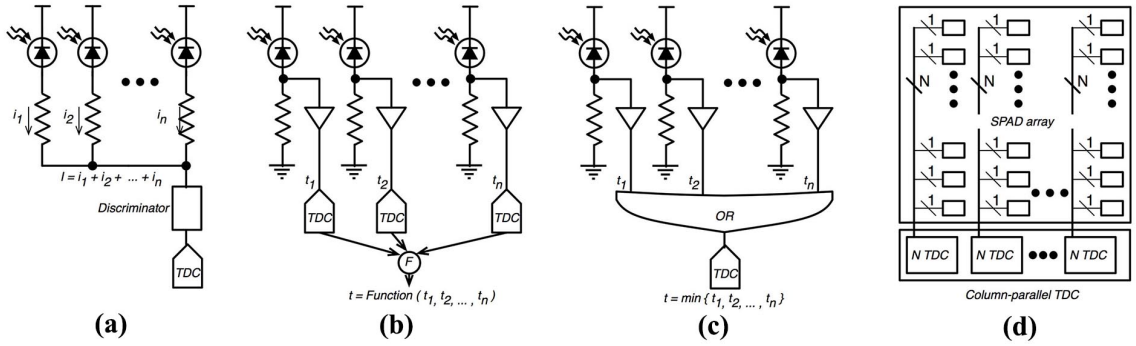

Figure 2.12: Different concepts of analog and digital SiPM. (a) Typical analog SiPM, (b) Full digital SiPM , (c) Conventional digital SiPM, (d) Multi-TDC digital SiPM. Picture is modified from [50].

figure 2.12 (b). A full digital SiPM has the capability to create timestamps for all detected photons, leading to obtain the best possible timing performance for scintillation detectors [52]. The disadvantage of this device is a quite low fill factor, since large space are used for the cell electronics and the TDC.

Another type of digital SiPM is developed by Philips [53]. The concept is shown in figure 2.12 (c). Each SPAD cell is represented as a digital photon counter, but all output signals from the SPAD cells are sent to the same TDC through a trigger network. A small animal PET scanner prototype by using the Philips digital SiPMs coupled to monolithic LYSO crystals reached a spatial resolution of 0.7 mm and time resolution of 680 ps full width half maximum (FWHM) [54].

Apart from the design of SiPM previous discussed, an multichannel digital SiPM (MD-SiPM) was developed by the Delft University of Technology and its concept is shown in figure 2.12 (d). Instead of all pixels in an array are connected to a single TDC, multiple TDCs are shared for all cells of the SPAD array. Study of the MD-SiPM has shown that the estimation of timing information by using multiple timestamps are more accurately than utilizing a single timestamp [55].

Chapter 3

Characterization of analog silicon photomultiplier

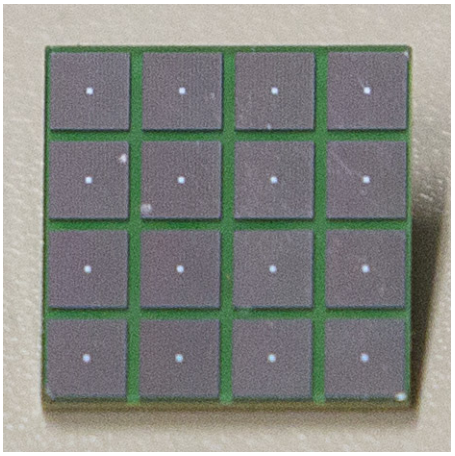

Figure 3.1: The picture of MPPC array (S12643-050CN).

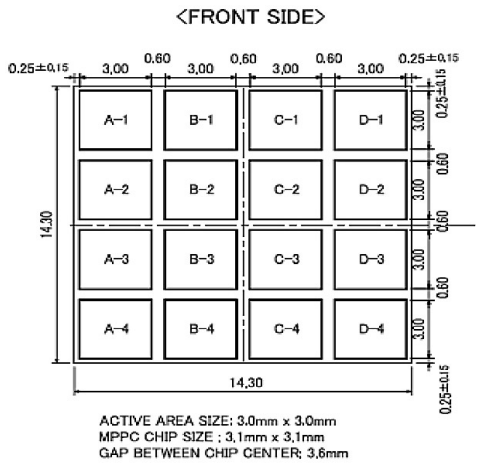

Figure 3.2: The drawing of the MPPC array (S12643-050CN) and its dimension description. Picture is taken from [56].

The result of the full characterisation of the samples of the multi pixel photon counter (MPPC) (S12643-050CN) produced by Hamamatsu for the EndoTOF-PET US project is presented here. These devices, manufactured with the through silicon via (TSV) technology, have a size of 3×3 mm^2 and feature a structure of reduced dead space along the peripheral of the active area. The MPPC array, is arranged in a 4 × 4 array as shown in figure 3.1 and figure 3.2, with a MPPC pitch of 3.6 mm (i.e 600 μm dead space between each MPPC). The SPADs have a 50 micron pitch with each chip having 3464 SPADs with some SPADs removed in the centre due to the TSV (60×58-16).

Before being installed, the MPPC arrays need to be characterised in terms of the breakdown voltage (V_B), noise performance and time performance. Figure 3.3 shows the scheme of the setup for current-voltage measurement and dark count rate measurement. An electronics

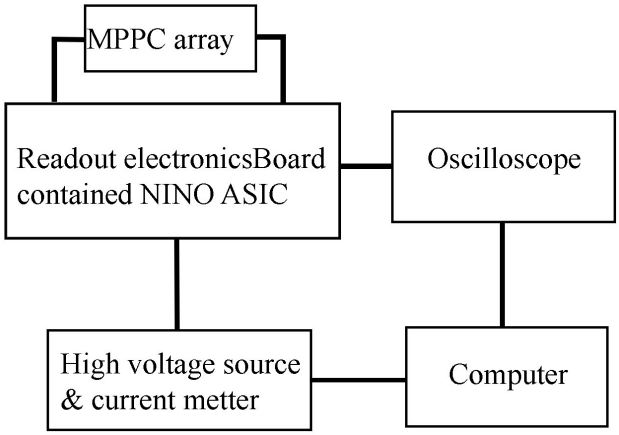

Figure 3.3: The drawing of the setup of current-voltage measurement and dark count rate measurement.

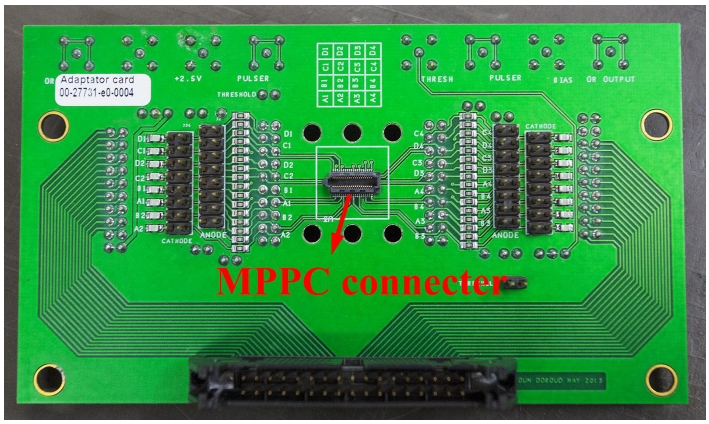

Figure 3.4: Picture of the printed circuit board (PCB) for the MPPC array characterisation.

board is designed to connect the MPPC array and high voltage power supply. A picture of the board's front side is shown in figure 3.4. The NINO ASICs are mounted to the back side of the board and give the output signal after amplification and discrimination [23]. The high voltage source and the oscilloscope are controlled by a specialised LabVIEW program [57].

After the characterisation of the MPPC arrays, the crystal matrices were glued to the MPPC arrays. The Dow Corning RTV 3145 was used for the gluing [58]. The index of refraction of RTV 3145 at 420 nm wavelength is 1.6 which allows more scintillating light to reach the MPPC array than air coupling. The coincidence time resolution (CTR) of 256 modules (crystal matrices glued on MPPC array) was measured. The result of this quality control procedure is also presented in this chapter.

3.1 Current-voltage curve

To find the proper operating voltage of the MPPC array, the current of MPPC output is measured as a function of the reversed bias voltage using a Keithley 2410 source meter in a

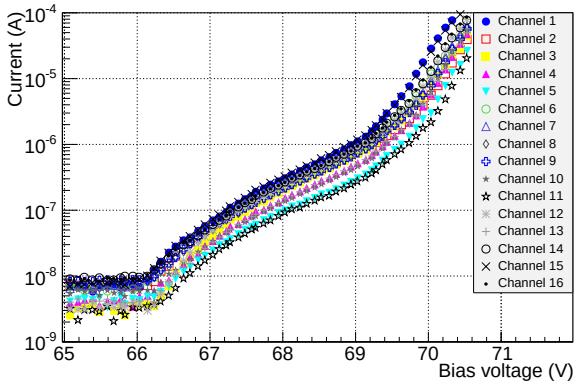

Figure 3.5: Current as a function of the applied bias voltage. The measurement is at 19 °C.

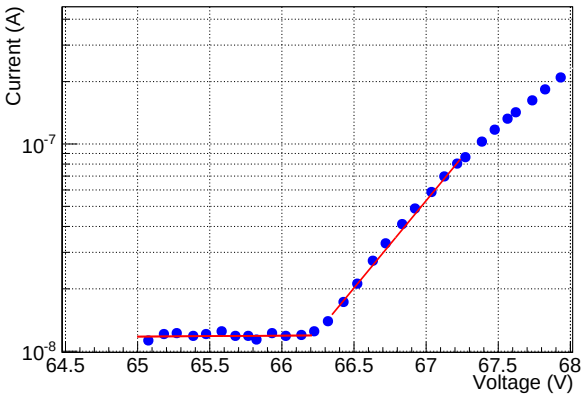

Figure 3.6: An example of the breakdown voltage extracted by the I-V method is shown. The measurement is at 19 °C.

temperature controlled dark box. A typical plot of current-voltage (I-V) for the 16 channels of a MPPC array is shown in figure 3.5. For the silicon photomultipliers, with a small over bias voltage, where only a small current is conducted, the current-voltage curve is exponential in accordance with the ideal diode equation [59]. The approximated function is the following:

$$I = I_1 e^{\frac{qV}{E}} \tag{3.1}$$

where I_1 is a pre exponential factor, q is the elementary charge, V is the over bias voltage and E is the characteristic energy [60]. One can estimate from figure 3.5 that channels of this array have a breakdown voltage around 66.2 V to 66.4 V. A zoom-in of I-V curve for one channel is shown in figure 3.6. Breakdown voltage of this channel of the MPPC array is extracted from the I-V curve as the intersection point between an exponential fit to the data 0 to 1 V above the breakdown and a baseline calculated below the breakdown voltage. An excellent homogeneity has been observed between the 16 channels of each MPPC array. The distribution of the difference of maximum and minimum breakdown voltage within a MPPC array for the 256 MPPC arrays is shown in figure 3.7. All 256 MPPC arrays have a

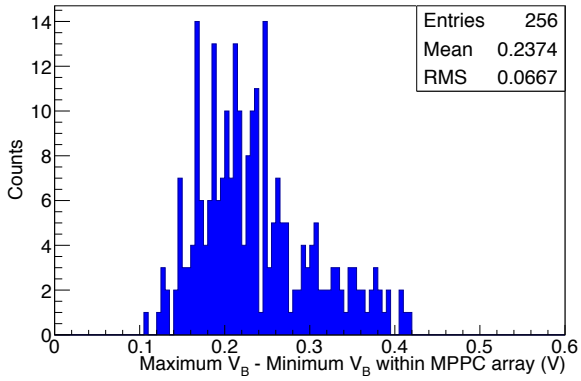

Figure 3.7: The distribution of the difference of maximum and minimum breakdown voltage within MPPC array for 256 MPPC arrays.

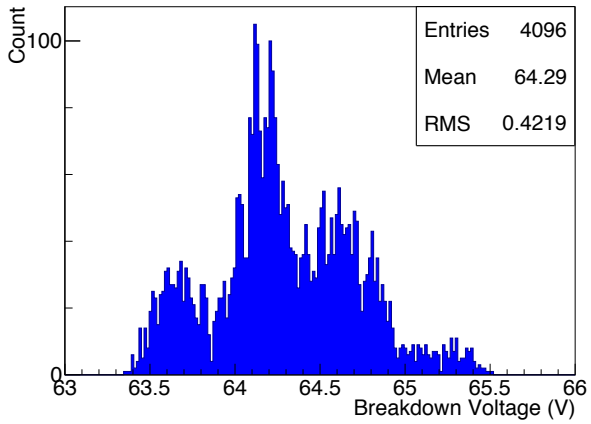

Figure 3.8: The breakdown voltage distribution of each MPPC in the 256 MPPC arrays.

breakdown voltage difference less than 0.5 V. Figure 3.8 is the breakdown voltage distribution of all the channels of 256 MPPC arrays. As can be seen, the breakdown voltage of different MPPC arrays have a big variation. To mount the 256 MPPC arrays to the EndoTOF-PET system, a sortation have been done according to the breakdown voltage, to ensure that the over bias voltage of the MPPC arrays arranged in the same front electronics board is more or less the same. Further more, the operating voltage of each MPPC array is adjusted according to their breakdown voltage. A difference in the over bias voltage would result in different PDE and compromise the performance of the TOF-PET system.

The temperature dependency of MPPC has also been studied. Figure 3.9 shows the breakdown voltage of the MPPC as a function of the temperature, the change of breakdown voltage is 63 mV/°C.

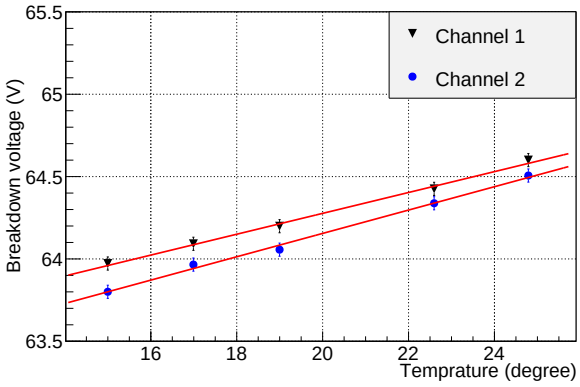

Figure 3.9: Breakdown voltage as a function of the temperature.

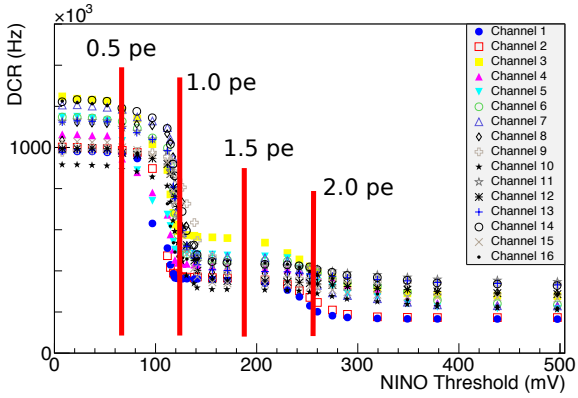

Figure 3.10: DCR as a function of NINO threshold. The over bias voltage is 3 V with temperature at 18 °C.

3.2 Dark count rate

An avalanche breakdown triggered by an electron generated from thermal excitation or by tunnelling effect is usually called dark noise. The dark count rate (DCR) represents the frequency of the dark noise. To measure the DCR, the MPPC array was placed in a dark environment. When a signal from the MPPC gives the charge output amplitude above the threshold set on the NINO board, a square signal is sent to the oscilloscope, the number of signals in 1 ms are counted. The dark count N_{signal} is the average number of 100 times measurement. The DCR was calculated as:

$$DCR = \frac{N_{signal}}{\Delta t} \tag{3.2}$$

The DCR has been measured as a function of the threshold of the NINO amplifier/discriminator. A typical DCR plot of 16 channels of one MPPC array is shown in figure 3.10. In the DCR plot, the DCR does not go to zero at high NINO threshold because the maximum threshold set does not reach the highest amplitude of the MPPC output signal. The measurements of the DCR have been performed with an over voltage of 3 V. The step in the DCR plot indicates

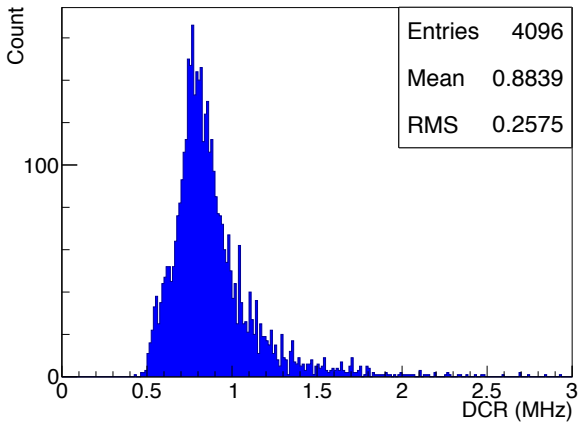

Figure 3.11: DCR distribution of 256 MPPC arrays.

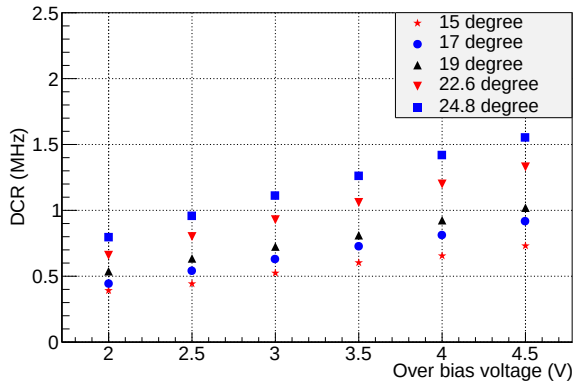

Figure 3.12: DCR as a function of temperature.

the threshold to separate 1 and 2 photo-electrons (pe). The steep slope around this threshold is an indication of a homogenous gain of all the microcells (SPADs) within one MPPC, and low noise when read out with the NINO ASIC. The best time resolution is achieved when the timing threshold of the readout ASIC is set as low as possible, above the noise level. The DCR values measured at the 0.5 pe threshold for all MPPCs are histogrammed and shown in figure 3.11; the mean value of the DCR distribution is 0.88 MHz for the total 256 MPPC arrays.

The value of the DCR for a MPPC arrays is also measured as a function of over voltage at different temperatures. Figure 3.12 shows the growing of the DCR versus bias voltage. The DCR increases faster at high temperature than at low temperature.

3.3 Crosstalk

Additionally, from figure 3.10, the percentage of the crosstalk between SPADs can be calculated. As described in chapter 3, the crosstalk can be calculated using the ratio of DCR at

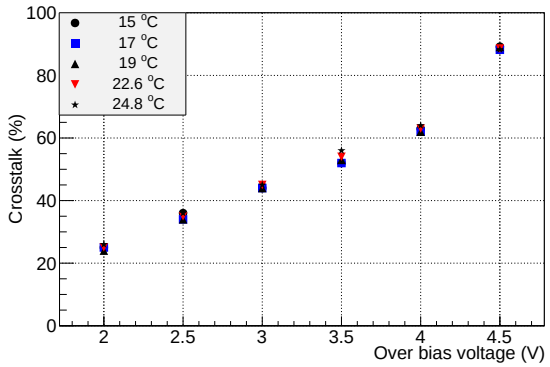

Figure 3.13: Crosstalk as function of the over bias voltage at different temperatures.

1.5 pe threshold to DCR at 0.5 pe threshold. The mean value of the crosstalk at 3 V over voltage for the 256 MPPC arrays is 43.8 %. Figure 3.13 shows the crosstalk as a function of the over bias voltage at different temperatures. The crosstalk has a strong dependence on the over bias voltage but it does not vary with the temperature. The crosstalk can limit the photon counting resolution and the dynamic range of the MPPC, so the energy resolution of the detector could be degraded when the over bias voltage is too high.

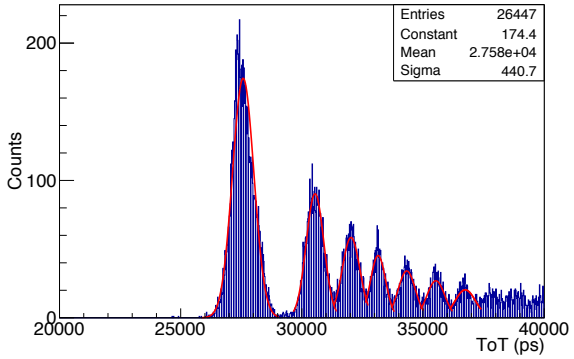

Figure 3.14: Single photon ToT spectrum.

3.4 Single photon time resolution

The single photon time resolution (SPTR) has been measured by illuminating the MPPC with a 403 nm laser light with temporal width of 48 ps full width half maximum (FWHM) [61]. It is worth to mention that the measured SPTR receives also a contribution form the front end electronics. Based on the DCR measurement, the trigger threshold was fixed at the 0.5 pe level firstly to detect the single photon events. A 16 channel TDC from CAEN (V1290N) basing on the CERN HPTDC was used for the data acquisition [62], [28]. The "synch out" signal from the laser was used as trigger signal and it was also sent to one TDC channel. The output signal from the NINO was recorded by another TDC channel.

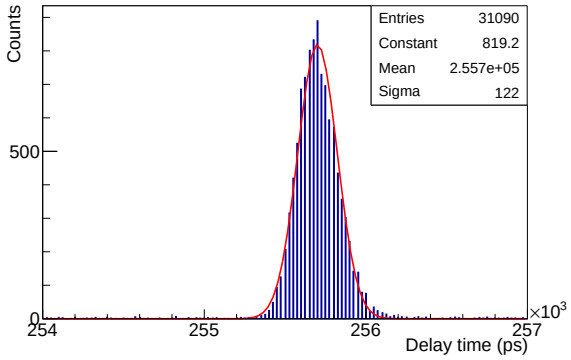

Figure 3.15: Histogram of time difference of selected single photon events.

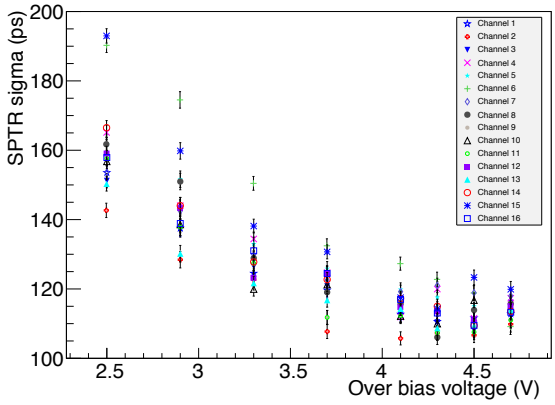

Figure 3.16: Single photon time resolution as function of over bias voltage.

The signal spectra is reconstructed offline from the time over threshold (ToT) and shown in figure 3.14. The first peak corresponds to the single photon electron event. For the SPTR measurement only events with ToT width within one sigma from the single photon mean ToT value were selected. The time difference of laser "synch out" signal and NINO output signal were histogrammed as shown in figure 3.15. A value of 119.3 ps sigma for SPTR is obtained from the gaussian fit to the time difference histogram. The SPTR has been measured as a function of over bias voltage and the result is shown in figure 3.16. An improvement of the SPTR with increasing bias voltage is observed, reaching a plateau of 110 ps sigma for an over voltage of 4 V.

The SPTR as a function of NINO threshold is also studied. The over voltage of MPPC was set at 4 V. As shown in figure 3.17, the SPTR reaches its best value when the NINO threshold is set around 20 mV. On the other hand, one can obtain a better energy resolution with higher NINO threshold. At the lowest NINO threshold, it is hard to separate the one photon event to two photon events. Alternately, two different threshold can be used to obtain the optimal value for both energy and timing measurement.

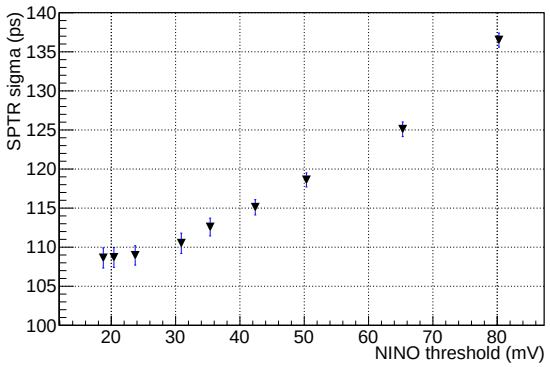

Figure 3.17: Single photon time resolution as function of NINO threshold.

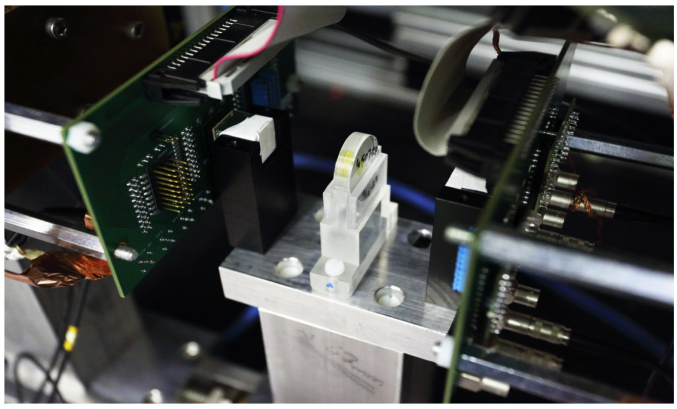

Figure 3.18: CTR bench for the quality control measurement.

3.5 Coincidence time resolution

3.5.1 Coincidence time resolution with scintillator matrices

The timing performance of the MPPCs coupled to the scintillating crystals (modules) was tested using the setup shown in figure 3.18: two 4 × 4 arrays of LYSO crystals are fully wrapped in Vikuiti specular reflector [63] and placed facing each other of 10 cm distance. A ^{22}Na source is placed between them and aligned with the line connecting the centres of the two modules. One module has been selected as the reference for the measurement of all the other 256 modules.

Data analysis is performed with a total number of 4 $\times 10^6$ triggers. An example of ToT spectra is shown in figure 3.19. The 511 keV gamma peaks were first selected in the ToT spectra; only events with the energy of the 511 keV gamma were selected for the CTR measurement. Then one histogram of the time difference between the two channels is shown in figure 3.20 as an example. This pair has presented a CTR of 227.3 ps FWHM.

Figure 3.21 shows the CTR as a function of over bias voltage for one pair of photodetector modules. The CTR improves with increasing on over bias voltage, as expected. In order to find the optimised NINO threshold for the timing performance, the CTR was also measured

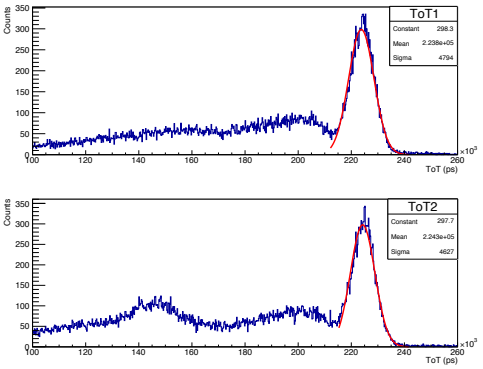

Figure 3.19: CTR of 3×3×15 LYSO crystal.

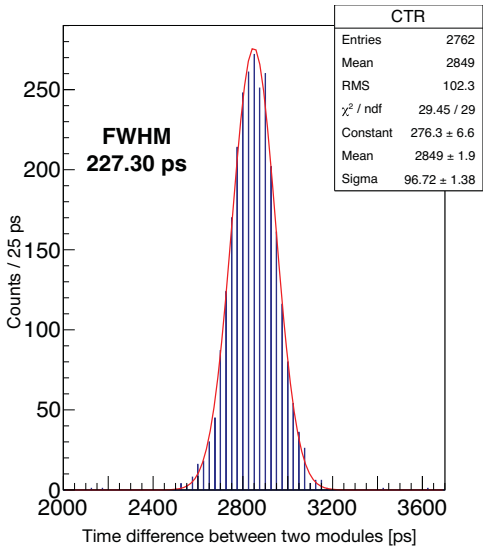

Figure 3.20: CTR of 3×3×15 LYSO crystal.

as a function of the NINO threshold as shown in figure 3.22. The CTR reach its best value in the range of 30 mV to 60 mV. It degrades for thresholds less than 30 mV. This can be explained due to noise around the baseline of signal. For the CTR measurements for the quality control of the 256 modules, an over voltage of 3 V was used, the NINO ASIC threshold was fixed at 55 mV, which is the threshold of 0.5 pe. The measurement setup was maintained at 19°C. The CTR of the 256 modules was measured with respect to the reference module and the distribution is presented in figure 3.23, with an average of 239 ps FWHM. The variation of the CTR among the different channels of the modules is due to the different light yield of the crystals, the quality of coupling, the different performance of each MPPC, and the quality of the wrapping.

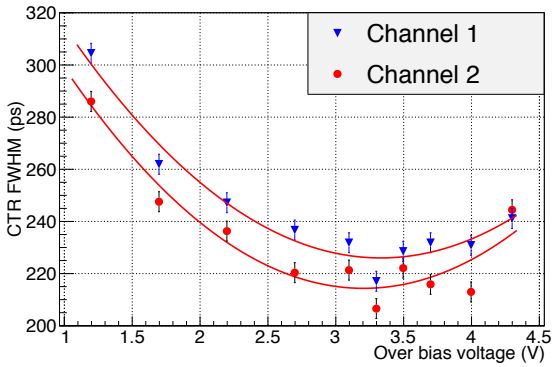

Figure 3.21: CTR as function of over bias voltage for 3.5×3.5×15 mm^3 LYSO crystal matrices.

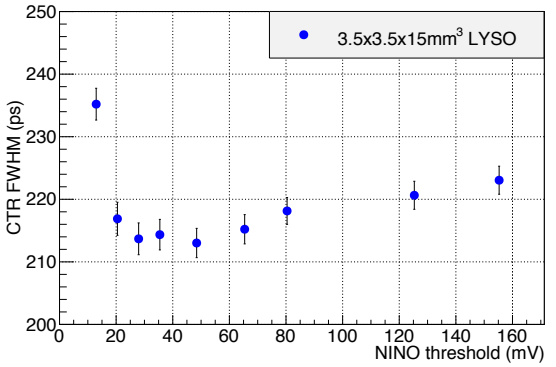

Figure 3.22: CTR of 3.5×3.5×15 mm^3 LYSO crystal with NINO threshold. The over bias voltage of two MPPC arrays fixed at 3.5 V.

3.5.2 Study of the effects degrading the coincidence time resolution

The MPPC array has been glued with two sets of single LYSO crystals. One set contains two LYSO crystals with the dimension of 3.5×3.5×15 mm^3, the same size of which is the crystals of the external plate. Another set contains two LYSO crystals with the dimension of 3×3×15 mm^3 which has the same cross section as the active area of MPPC used. The two set crystals were coupled to same MPPC and all crystals were fully wrapped with Vikuiti. As shown in figure 3.24, the best CTR of 3×3×15 mm^3 LYSO crystal is 170 ps, the best CTR of 3.5×3.5×15 mm^3 LYSO crystal is 193 ps. A previous study has shown that the CTR has a strong relation with the light yield of the crystal [64]. With the 3.5 × 3.5 mm^2 cross section LYSO crystal coupled to the 3 × 3 mm^2 active area of MPPC, 26.5% of the scintillating photons are lost due to the mismatch of size. The result of the CTR for the two LYSO crystal dimensions is in agreement with a simple assumption of the CTR dependence on the light detected as:

$$CTR \propto \frac{1}{\sqrt{Light\ detected}} \tag{3.3}$$

Nevertheless, the Hamamatsu Discrete MPPC with the new TSV technology read out by ultrafast amplifier discriminator (NINO ASIC) showed excellent performance of 170 ps FWHM

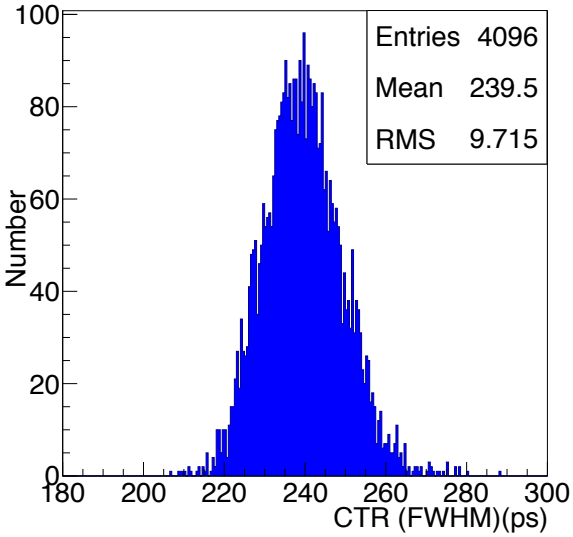

Figure 3.23: CTR as function of over bias voltage for 3.5×3.5×15 mm^3 LYSO crystal matrices.

CTR for two back to back single crystals with the dimension of 3×3×15 mm^3.

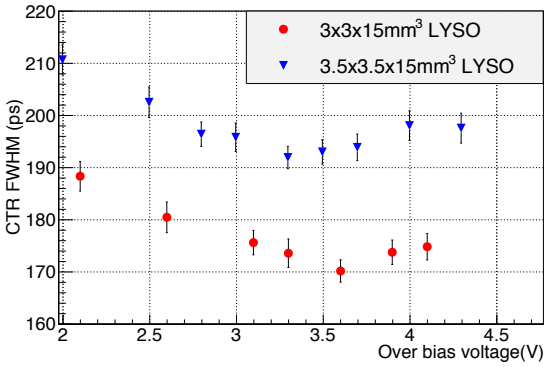

Figure 3.24: CTR as function of the over bias voltage for two sets of LYSO crystals. The over voltage of one MPPC array fixed at 3.5 V. The NINO threshold was fixed at 55 mV.

The CTR value measured in our setup became worse from 190 ps to 239 ps by coupled 4×4 3.5×3.5×15 mm^3 LYSO crystal matrices instead of single 3.5×3.5×15 mm^3 LYSO crystal. The possible factors degrading the timing performance could come from the front end electronics and readout chip used in the evaluation bench.

To investigate the origin of the time resolution degrading from single channel of MPPC array to the multi-channel of MPPC array, two single LYSO crystals with the dimension of $3\times3\times15\ mm^3$ coupled to the MPPC array have been studied in different configuration. In the first configuration, only cables linked to the 2 MPPCs with coupled single crystal were connected to the HPTDC. The high voltage was selected to apply to only the MPPCs with coupled crystal or all channels of the MPPC array. The result is listed in the table 3.1. There

Number of TDCs connected	Number of active MPPCs of MPPC array	CTR (ps) (FWHM)
2	2	173.45±2.23
2	16	174.52±2.39

Table 3.1: The CTR at different configuration for the same two single 3×3×15 mm^3 LYSO crystal coupled to MPPC array.

is no difference of CTR value in these two configurations. So the signals from other channels does not affect the timing performance in the front electronics.

The time resolution of another configuration for the connection of HPTDC has also been measured and the result is shown in figure 3.25. As can be seen from the figure, the best CTR is 173 ps when only 2 channels of HPTDC is connected to the target channel of MPPC array. When all the channels of HPTDC are connected, the CTR degraded to about 197 ps. The crosstalk calculated by the ToT in each channel are shown in figure 3.26. The mean value of the time difference among other channel to the target channel are shown in figure 3.27. The time difference in 16 channels is in the range from 1.1 ns to 10.8 ns. The 4 close neighbour channels have a big crosstalk and the time is quite close to the target channel. These crosstalk between the channels of HPTDC will degrade the timing performance [65].

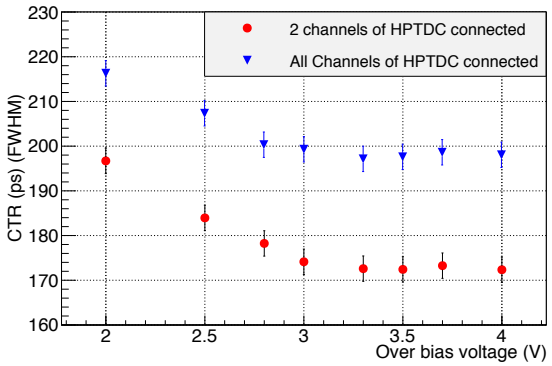

Figure 3.25: CTR in different configuration of 3×3×15 mm^3 LYSO crystal. The over bias voltage of one MPPC array fixed at 3.5 V.

3.6 Conclusion

The characterisation of 256 arrays of 4×4 MPPC arrays, supplied by Hamamatsu for the external plate detector of EndoTOFPET-US, has been performed. These arrays have low DCR and exhibit good SPTR of 110 ps sigma. The breakdown voltages for the individual MPPCs in the 4x4 arrays are within 0.5 V range. An average CTR value of 239 ps FWHM has been measured for the 256 modules. For such a large number of readout units (crystals + MPPC array), such performance is very promising and close to our target value of 200 ps. A study of the improving the time resolution was also performed. One factor degrading

3.2 %	6.1 %	8.2 %	7.2 %
6.3 %	15.9 %	48.2 %	21.2 %
11.7 %	44.3 %	100 %	46.1 %
7.1 %	14.1 %	41.1 %	17.1 %

Figure 3.26: The crosstalk calculated by the ToT from all channels for the 511 keV photon event. The channel with 100% is the trigger channel. The over bias voltage of one MPPC array fixed at 3.3 V.

10.8 ns	7.6 ns	7.2 ns	6.4 ns
6.8 ns	4.7 ns	1.1 ns	4.0 ns
6.1 ns	1.8 ns	0.0 ns	1.4 ns
7.8 ns	5.7 ns	2.1 ns	5.5 ns

Figure 3.27: The mean value of the register time in the HPTDC. The channel with 0.0 ns is the trigger channel and other channels have the relative time to the trigger channel.

the timing is the light loss because the scintillator has larger size than the dimension MPPC. Crosstalk between the channels of HPTDC was measured due to the spread light from the scintillating crystal. This should be considered in the further design of the readout chip of EndoTOFPET-US scanner to optimize the timing performance. Besides, the variation of the CTR in different channels can be also explained by the different quality of wrapping, variation of the light yield of the scintillating crystal, the quality of the alignment for the coupling between MPPC array and crystal matrices and so on.

Chapter 4

Multichannel digital Silicon photomultiplier

A multichannel digital Silicon photomultiplier (MD-SiPM) has been developed by Delft University of Technology for the internal probe of EndoTOFPET-US project. Several matrices of 9×18 LYSO crystal with cross section of 0.7×0.7 mm^2 and lengths varied from 8 to 15 mm were produced from the company Proteus to be tested for the internal probe. The MD-SiPM was designed as a 9×18 arrays with matching dimensions with the crystal matrices. The architecture of the MD-SiPM chip is introduced in this chapter and a complete evaluation of the chip is shown.

4.1 Architecture of MD-SiPM chip

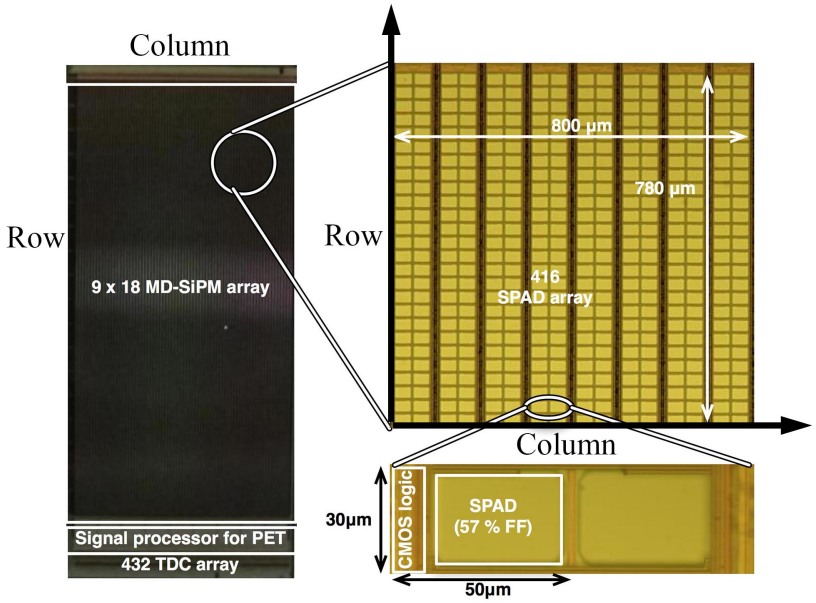

Figure 4.1: The plot of 9×18 array MD-SiPM. Top right is the zoom in plot of one array of the MD-SiPM. Single SPAD cell is also shown in the bottom of right side. Picture is modified from [66].

The 9 × 18 MD-SiPM chip has a dimension of 7.6 × 17.1 mm^2. Figure 4.1 shows the architecture of the MD-SiPM with 9 × 18 arrays. Each array consists 416 SPAD cells arranged in 16 × 26, result a matrix of 144 × 468 SPAD cells in the whole chip. The dimension of the array is 800 μm × 780 μm as shown in the top right side of figure 4.1. Each SPAD cell has a size of 30 × 50 μm^2 [67]. To maximize the PDE of the chip, each pixel has a active area up to 57%. The MD-SiPM chip are mounted in a PCB, with all the communication to the PC via field-programmable gate array (FPGA).

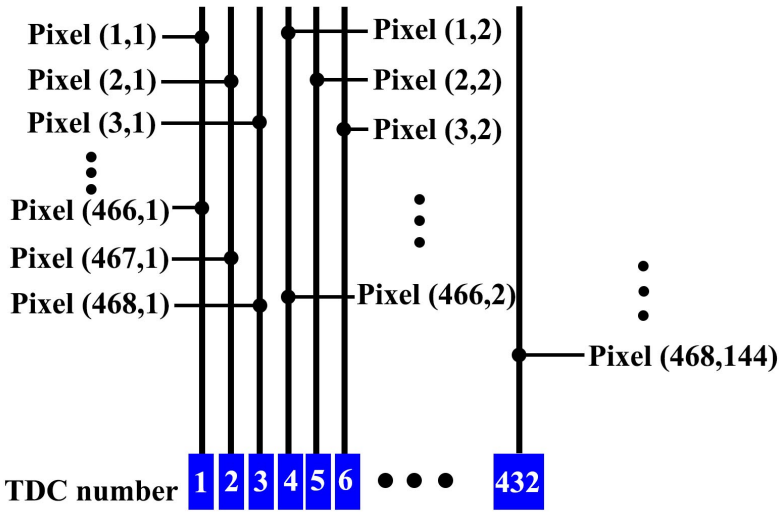

Figure 4.2: Plot of the TDC connection to pixels of the chip.

A new feature in the design of this chip is the way in which 162 arrays are connected to 432 TDC channels. As shown in figure 4.1, the axis along the TDC array direction is named as column of the chip, the orthogonal axis is named as row. Each column of the chip is connected to 3 TDCs. The arrangement of the TDC connection is depicted in figure 4.2. The first pixel in the column 1, row 1 (pixel(1,1)) is connected to the TDC 1, The second pixel in the column 1, row 2 (pixel(2,1)) is connected to the TDC 2, the third pixel in the column 1, row 3 (pixel(3,1)) is connected to the TDC 3. Then the fourth pixel (4,1) is connected again to the TDC 1, and so on. The pixels in column 2 are connected to the TDC 4 to 6, till the pixels in last column, which is connected to the TDC 430 to 432. Thus each array of 16 × 26 pixels is connected to 48 TDCs, and the 18 arrays in a column are connected to the same 48 TDCs.

The circuit of a single SPAD with its electronics is shown in figure 4.3. One pixel (SPAD cell together with its electronics) consists of a SPAD for detecting the light, a quenching circuit, a 1-bit counter to record wether the SPADs detecting a photon or not, a mask circuit to enable or disable the SPAD and a connection line to pass the output signal to the TDC. Thus, differently from an analog SiPM, the MD-SiPM is able to select the pixels to be used and each pixel gives a simple digital output (0 or 1), to give the light detection information.

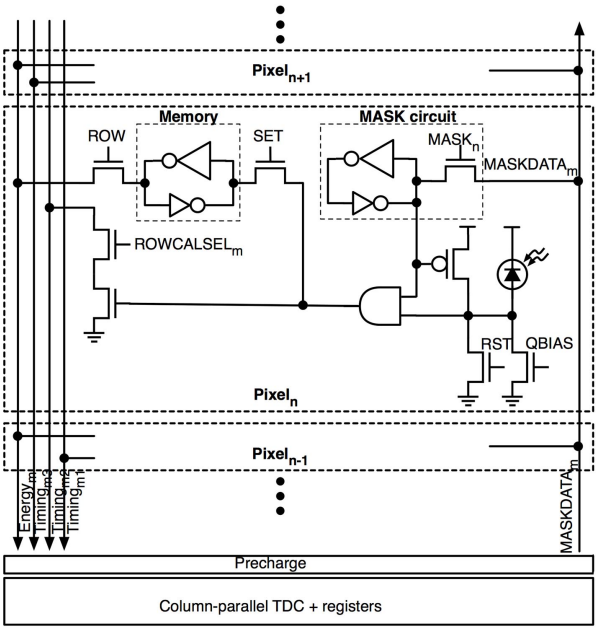

Figure 4.3: The schematic of single SPAD cell circuit. Picture is taken from [66].

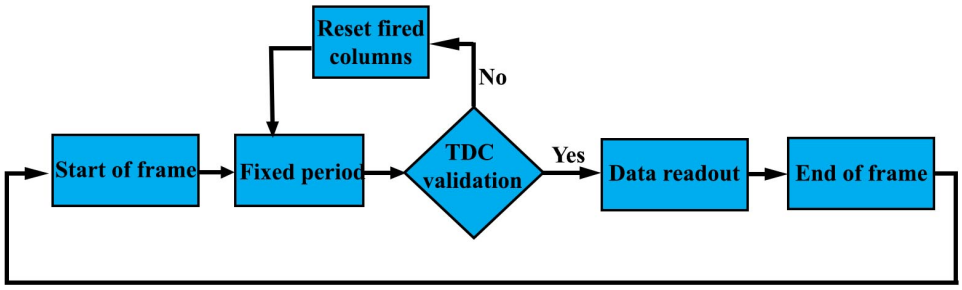

Figure 4.4: The flowchart of the MD-SiPM data acquisition.

4.2 Operation sequence of MD-SiPM chip

The data acquisition and readout of MD-SiPM employs a frame based readout. The scheme of the data acquisition flow is shown in figure 4.4. In the beginning of a frame, all pixels and TDCs of chip are ready for the collecting photons. After a predefined time (range from 50 ns to 200 ns), the number of fired TDCs are recorded and compared to a TDC threshold. If the condition is validated, the chip continues the data acquisition until the end of the frame. The frame can be set up to 6.4 μs. If the threshold is not reached, a smart reset function is used, all the fired TDCs and pixels are refreshed and the chip collects the photons in the same frame again. The fired pixels and TDCs are insensitive during the reset functions, but the unfired pixels are still capable to detect the photons. The data of one frame are sent to the pixel memories. These data are readout during the next frame.

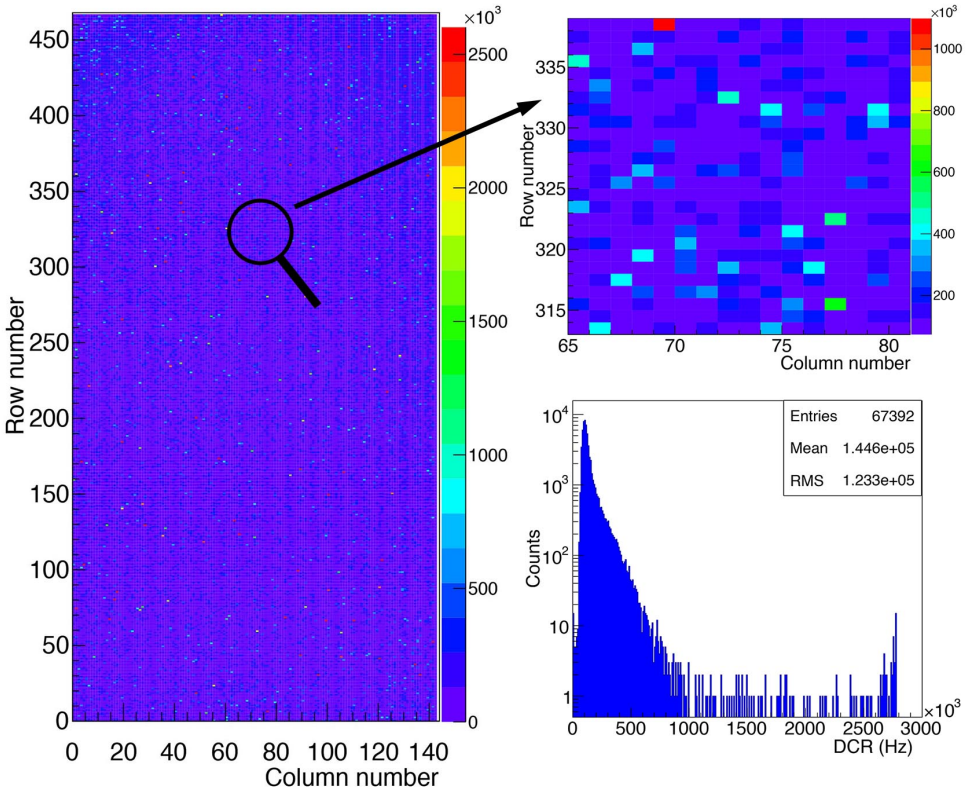

Figure 4.5: Left plot: DCR map of the whole pixels in the MD-SiPM chip. Plot on the top of right: Zoom in of an array on the left plot. Plot on the bottom of right: Histogram of the DCR of all pixels. The over bias voltage was 2.5 V at 18 °C.

4.3 Dark count rate

The DCR of the whole chip was measured when placing the chip in a tight dark box. Each pixel gives a dark count value N_{dark} in certain time ΔT. Thus the DCR of the pixel is calculated by:

$$DCR_{pixel} = \frac{N_{dark}}{\Delta T} \tag{4.1}$$

Figure 4.5 shows a DCR map of the whole chip when the chip is operated at 2.5 V above the breakdown voltage. The frame interval for the DCR measurement was 260 ns. The whole DCR of the chip is the sum of the DCR value of all pixels. A detailed DCR map of one array is shown in the top left of figure 4.5. For most pixels, the DCR value is less than 500 kHz. The plot on the bottom of right side in figure 4.5 gives the distribution of DCR for all pixels. The DCR value is centred around 144 kHz while a few pixels with a high DCR value. For the 9 $\times$ 18 array, the mean DCR of arrays is 53.7 MHz.

The DCR of the chip can be suppressed by disabling some very hot pixels with little cost in terms of the PDE. The DCRs of all arrays were measured as a function of the percentage of active pixels at different over bias voltage. As shown in figure 4.6, the DCR is increasing with the over bias voltage. The less pixels enabled, the lower of the DCR. Disabling the 10 % of the pixels with highest DCR, the overall DCR is reduced by a factor of 2. The percentage of the active pixels of the chip needs to be optimised by taking into account both the DCR

and the PDE.

The number of dark counts of an array during different frame acquisition time has also been measured and the result is shown in figure 4.7. Without a smart reset function, 160 pixels of the total 416 pixels will be fired in 6.4 μs due to dark noise. The dark count level is kept in the same level at 20 pixels in 6.4 μs when the smart reset function is used.

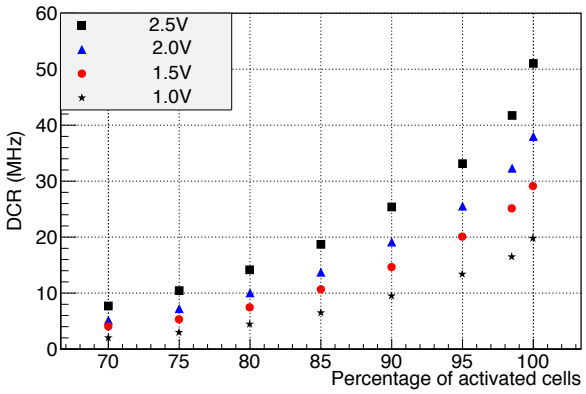

Figure 4.6: Mean value of array DCR as function of the percentage of active pixels at different over bias voltage.

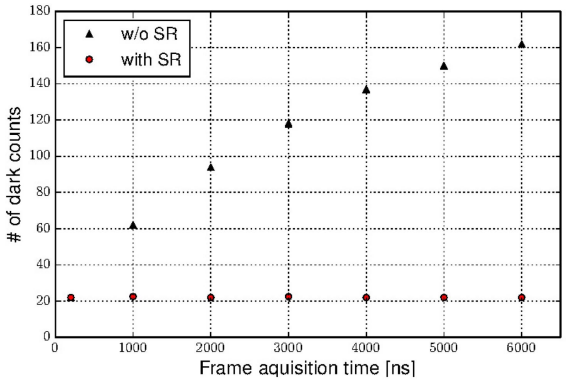

Figure 4.7: The data count number recorded without smart reset and with smart reset. The plot is taken from [68].

4.4 Single photon time resolution

Figure 4.8 shows the setup for the SPTR measurement. A picosecond laser with 403 nm wavelength is used to illuminate the MD-SiPM chip [61]. The pulse width of the laser is 48 ps FWHM. Several neutral density filters are placed between the laser and MD-SiPM chip, to decrease the laser light intensity to the level of single photon per pulse. A pulse was generated when the MD-SiPM started a data acquisition frame and sent to the laser as a trigger signal. The trigger signal was delayed 100 ns to give light pulse to the MD-SiPM in the middle of an acquisition frame. The over voltage for the SPTR measurement was 2.5 V.

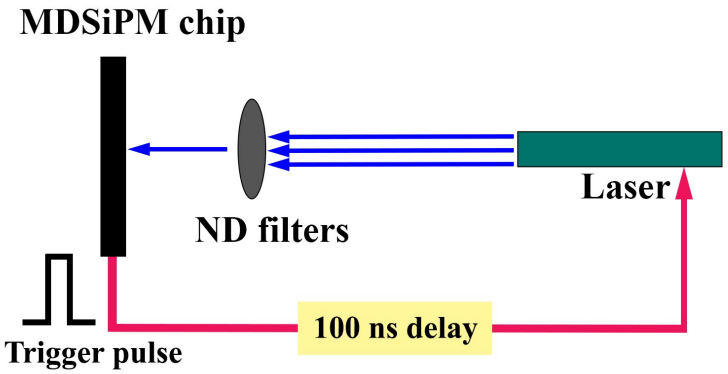

Figure 4.8: Schematic of the single photon time resolution setup.

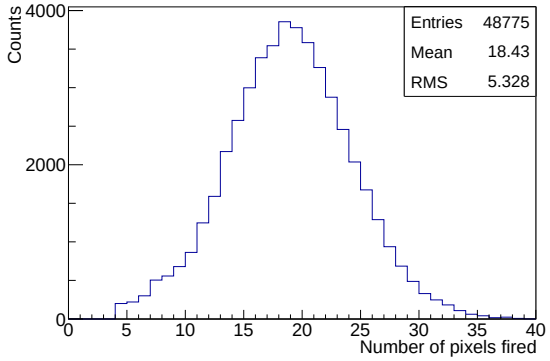

Figure 4.9: Pixels fired distribution for an array of MD-SiPM in absence of light. The over voltage was 2.5 V and the temperature was at 18 °C.

The SPTR measurement is based on the array of MD-SiPM chip. Since the SPTR requires low photon counting level, only 1 array was activated in the measurement. The DCR could be very high while the whole chip is enabled. Figure 4.9 shows the background spectra of an array when all pixels were enabled. The mean value of pixels fired is 18.4 and this high noise level make it unable to find the single photon spectrum. To suppress the noise events, only 60% of the pixels in the array were activated.

The distribution of number of fired pixels in the SPTR measurement is shown in figure 4.10. The number of fired pixels is 0 when no photon is detected by the chip. The arriving time of all events where only 1 pixel is fired were histogrammed as shown in figure 4.11. A gaussian fit to the time distribution gives a SPTR value of 287 ps (FWHM). The SPTR of this array was also measured as a function of over voltage. The SPTR improves when increasing the over voltage, and reach its optimal value of 285 ps (FWHM).

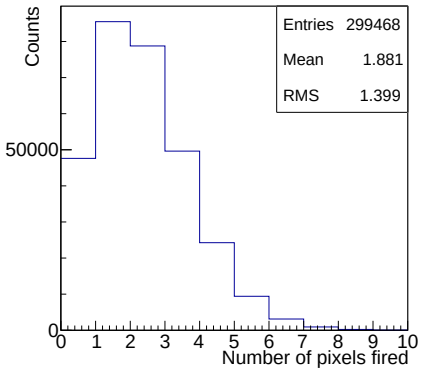

Figure 4.10: Number of fired pixels in the SPTR measurement. The over voltage is 2.5 V.

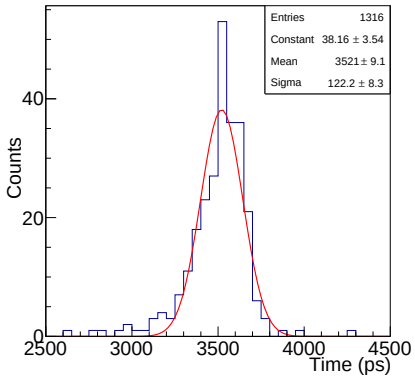

Figure 4.11: Histogram of the photon arriving time. The over voltage is 2.5 V.

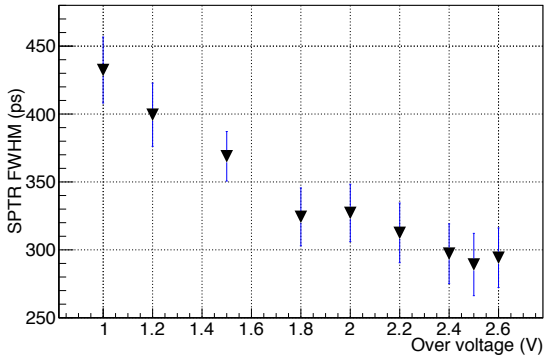

Figure 4.12: SPTR as a function of the over voltage. 40% of the pixels are inhibited.

4.5 Light yield with scintillation crystal

Each single crystal produced for the internal probe of EndoTOF-PET US detector has a cross section of 0.7 × 0.7 mm^2. Thus each crystal is coupled with a single array of 416 pixels. To test the energy performance of the MD-SiPM chip, a matrix with 4 × 4 LYSO crystals (0.7×0.7×10 mm^3) was glued to the MD-SiPM chip. The crystal matrix was fully wrapped with Teflon. Each LYSO crystal was aligned with an array of the chip, thus 16 arrays of the chip were coupled to crystals.

Figure 4.13 shows the picture of MD-SiPM chip with the crystal matrix glued to it. The Dow Corning RTV 3145 is chosen for the gluing [58] which remains stable coupling during the data taking for the coupling with SiPM. A ^{22}Na source with 3.65 MBq activity was positioned in front of the crystal matrix. The chip is operated at 2.5 V over bias voltage, at a stable temperature of 20 °C. A frame acquisition time of 400 ns is used.

Figure 4.14 shows the spectrum of the number of photons detected in the 16 arrays. The 511 keV photopeak can be identified in all the arrays. A gaussian fit is applied to the

spectrum of each array. The mean value of the energy resolution of the 16 arrays is 18.26% (FWHM). The distribution of the individual energy resolution is shown in figure 4.15.

The crosstalk of different arrays were also calculated. An example is shown in figure 4.16. One array was selected as a trigger array, only 511 keV event were histogrammed. After correction with the background spectra, the crosstalk in the neighbour arrays is from 16.2% to 26.3%.

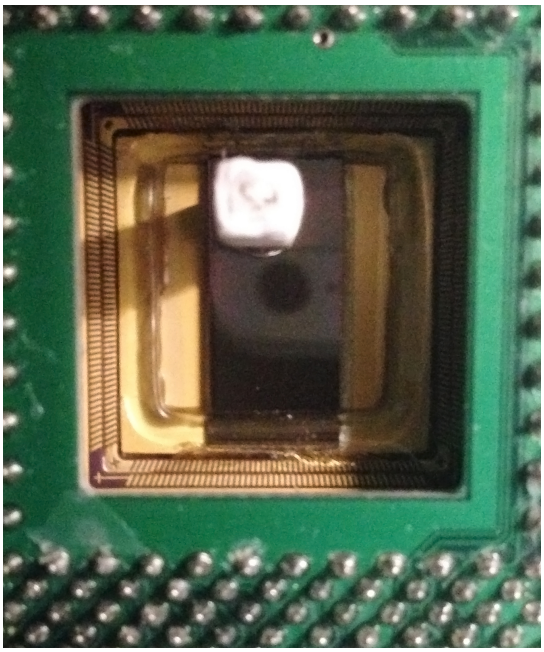

Figure 4.13: Picture of the glued crystal matrices and MD-SiPM chip.

4.6 Conclusion

The MD-SiPM chip developed from Delft University of Technology has been evaluated for its noise performance, timing performance and energy performance. A SPTR value of 285 ps FWHM was obtained and I have succeeded to get a 511 keV photopeak with coupled 4×4 LYSO crystal matrices of size $0.7 \times 0.7 \times 10$ mm^3 to the chip. An energy resolution of 18.26% (FWHM) of 511 keV photopeak has been achieved.

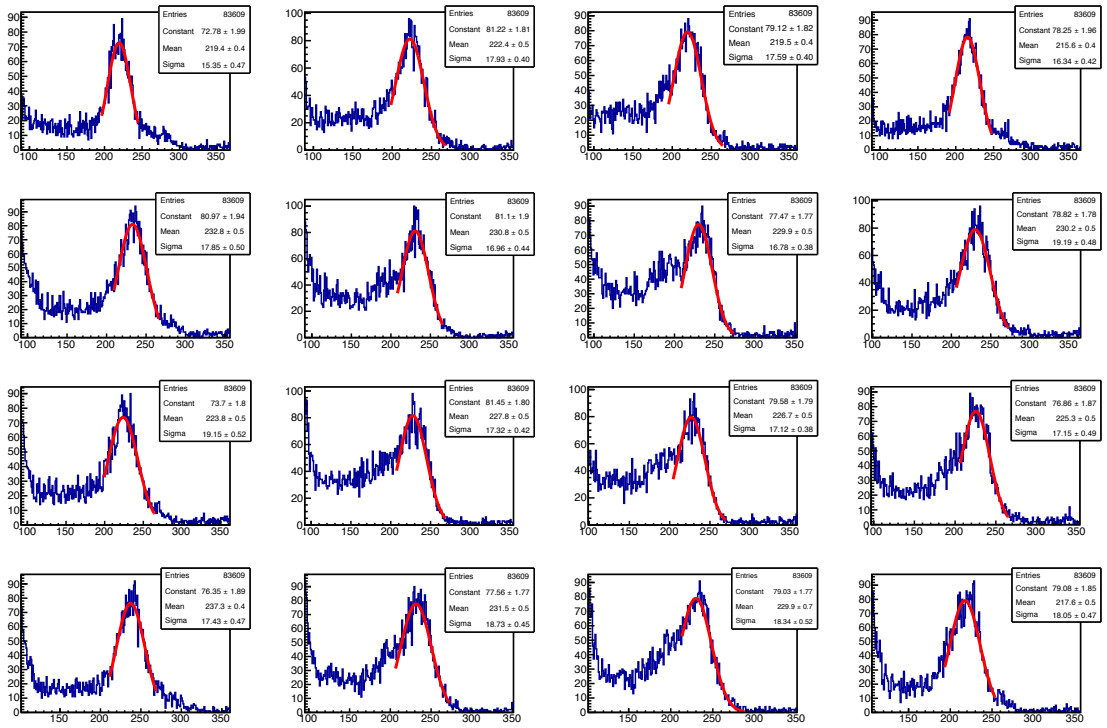

Figure 4.14: Fit of the array of 511 keV photo peak.

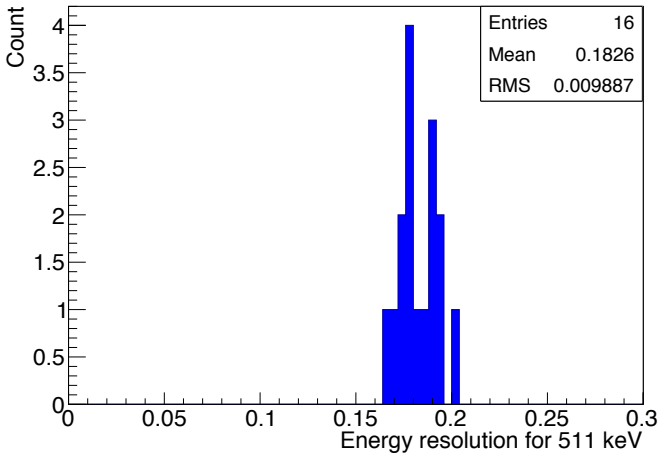

Figure 4.15: Distribution of the energy resolution for 16 arrays.

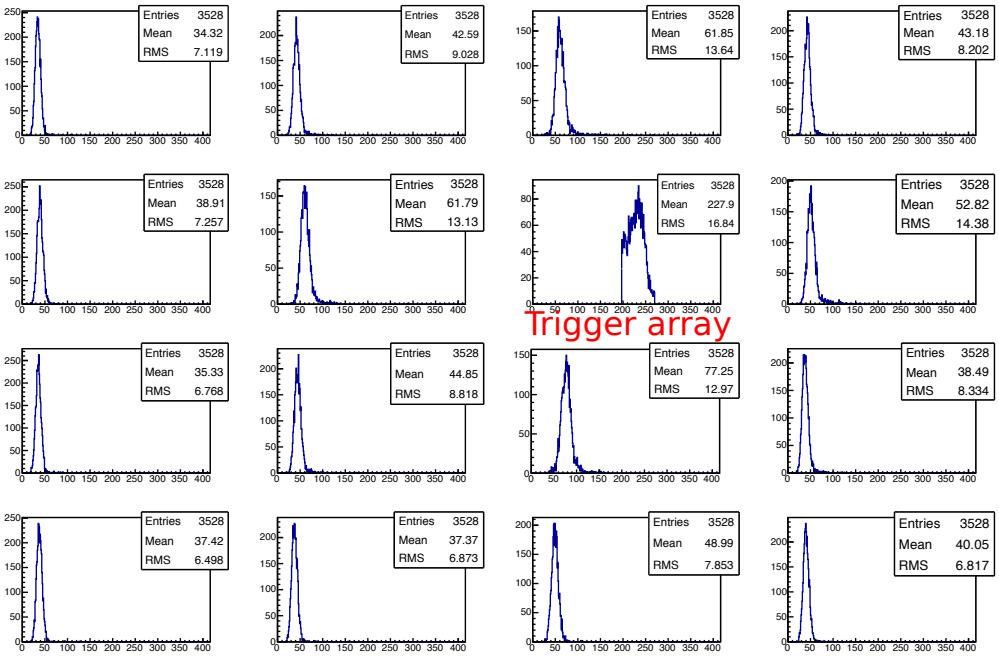

Figure 4.16: ^{22}Na spectra in the triggered array and spectra of neighbour arrays.

Chapter 5

Digital silicon photomultiplier of Philips

The concept of digital Silicon Photomultiplier (SiPM) has been introduced by Philips as an innovative technology to analog Silicon Photomultiplier devices. In general a SiPM consists of an array of single photon avalanche diode (SPAD) operated in Geiger mode and capable of detecting single photon to multi photons. In the case of the digital SiPM, complementary metal-oxide-semiconductor (CMOS) electronics are integrated into the SiPM chip, resulting in a fully digital readout. The number of SPADs that fired is summed by on-chip counter [53]. In the ideal case of a digital SiPM, each SPAD is connected to a time to digital converter (TDC), and the time information of a pulse from a scintillator can be obtained from the time information of the first few photons reaching the SiPM. However, such a device has not yet been realised. The Philips digital SiPM, has a pair of TDCs connected to each array (12800 SPADs). A complete characterization of the Philips digital SiPM is presented in this chapter.

5.1 Layout of Philips digital silicon photomultiplier

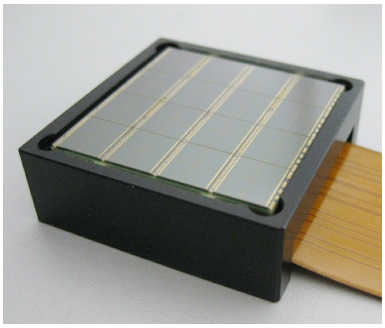

Figure 5.1: Image of Philips DPC-3200-22 sensor.

The Philips digital photon counter (PDPC) evaluation kit consists of two DPC-3200-22 sensors together with the DAQ computer and the voltage supply. An image of DPC-3200-22 sensor is shown in figure 5.1. Each DPC-3200-22 sensor consists of 16 independent dies arranged in a 4×4 matrix. The dimension of the whole chip is $32.6 \times 32.6\ mm^2$ as indicated

in figure 5.2. The layout of one die is shown in figure 5.3. The dimension of each die is 7.15×7.8775 mm^2 and each pixel of the die has an area of 3.2×3.8775 mm^2. There is a dead space of 0.8 mm from die to die for the bond wires mounted in the chip (orange area). The total number of SPAD cells in one die is 12800, arranged in 100 rows and 128 columns, and the dimension of each SPAD cell is 59.4×64 μm^2. Each die contains four pixels in the form of a 2x2 matrix. Each pixel consists of 3200 cells [69]. Each die sensor has a pair of TDCs and it generates a single timestamp per die. The trigger signals are generated when one pixel of a die reaches the threshold. Furthermore, the pixel is separated into 4 sub-pixels, which are used for setting the trigger schemes of the chip as detailed in the next section.

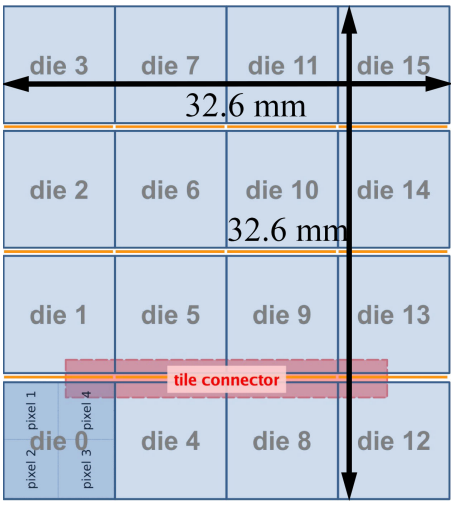

Figure 5.2: Layout and dimension of Philips digital SiPM [69].

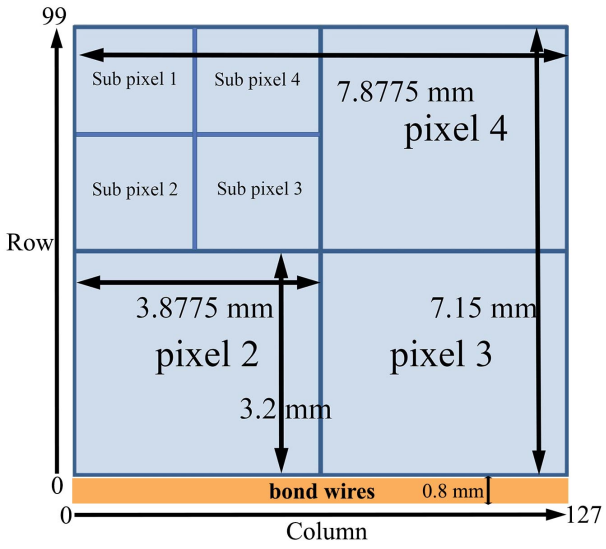

Figure 5.3: Layout and dimension of single die composed of 4 pixels. Each pixel consists 3200 SPAD cells.

5.2 Data acquisition sequence

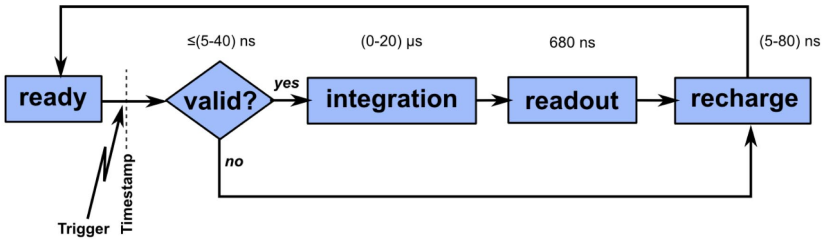

Figure 5.4: Schematic of the data acquisition. Picture taken from [69].

Figure 5.4 shows the data acquisition sequence of Philips digital SiPM. Each die of the

chip operates independently but it is synchronised with the internal clock time. Every die is ready to detect the photon when the operating voltage is applied. When the avalanches developed in some SPAD cells of a die, a trigger signal is generated if the number of fired SPAD cells exceeds a tunable trigger threshold. The timestamp of the event is also recorded by the TDC as the moment when the trigger signal started. A validation step follows trigger condition: The number of fired cells in the pixels counted counted in a given time interval (5-40 ns) after the trigger is not reach the configured detection threshold, the detection process is terminated and all SPAD cells are refreshed to get ready for the next process. Otherwise, an integration process with a configurable duration from 0 to 20 μs starts when the validation condition is fulfilled. At this process the chip continues to detect further incoming photons. Then all the number of the fired SPAD cells is read out and all the counters are sent to the memory buffer to be saved, this operation required about 680 ns to be completed. After the readout process, the SPAD cells of die are recharged and the die enter next data acquisition process.

5.2.1 Trigger scheme

The Philips digital SiPM provides a trigger setting based on the sub-pixels design of the chip. The trigger threshold can be configured so that the TDC can register the time information at the detection of the first photon or, alternatively, at higher photon thresholds. There are 4 available trigger schemes, each corresponding to different logic connection between the 4 sub-pixel of one pixel [69]. The logic connection of different trigger schemes and an estimate of the average number of photons required to reach the trigger threshold are indicated in the table 5.1. For instance, with trigger scheme 1, any one of sub-pixel detecting a photon can generate the trigger signal. When the trigger scheme 4 is used, the 4 sub-pixels are connected as a AND gate. To fulfil this trigger scheme, each sub-pixel of the die has to detect at least one avalanche breakdown. The dark counts can be suppressed by carefully choosing an optimal trigger scheme [70].

Trigger scheme	Logic connection	Average number of photons to trigger
1	sp1 $\vee$ sp2 $\vee$ sp3 $\vee$ sp4	1
2	[(sp1$\vee$sp2)$\wedge$(sp3$\vee$sp4)]$\vee$[(sp1$\vee$sp4)$\wedge$(sp2$\vee$sp3)]	2.333
3	(sp1 $\vee$ sp2) $\wedge$ (sp3 $\vee$ sp4)	3.0
4	sp1 $\wedge$ sp2 $\wedge$ sp3 $\wedge$ sp4	8.333

Table 5.1: 4 different trigger schemes provided in the chip and their corresponding logical connections based on sub-pixels (sp). The parameters are taken from [69].

5.2.2 Validation process

The validation logic of Philips digital SiPM is designed to suppress the recording of the false events due to dark count and it can be used as a pre-energy threshold when implemented to a PET detector system. There are two setting parameters for the validation process. The first one is the validation time interval. This tunable value can be configured as 5 ns, 10 ns,

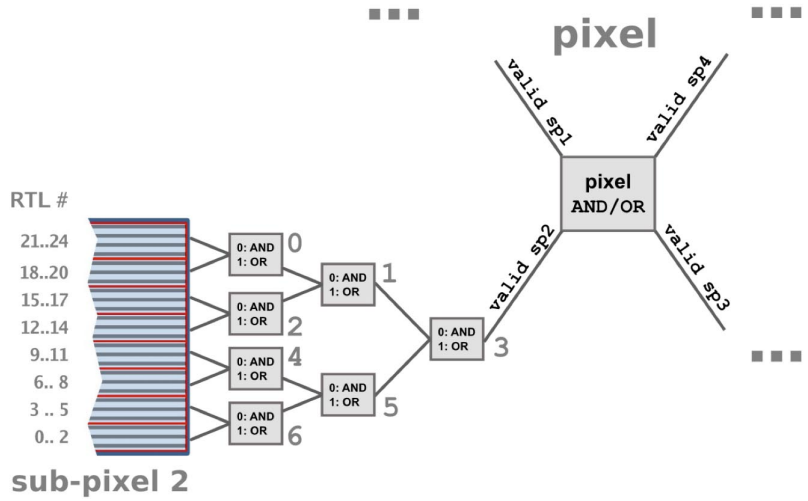

Figure 5.5: The validation configuration network of the Philips digital SiPM. Picture taken from [69].

20 ns and 40 ns, respectively. A longer validation time interval could result in a longer more accepted dark count events.

The other validation parameter is the validation threshold. The logic of the validation scheme is similar to the trigger logic. As shown in figure 5.5, the sub-pixel is divided to eight row trigger lines (RTLs), each contains 3 or 4 rows of SPAD cells. The RTLs are connected in paris to a logic gate, configured with OR logic or AND logic. The validation network of sub-pixel is built with seven logic gates, labeled with different number as indicated in figure 5.5. Additionally, the four sub-pixels are connected to another AND/OR logic gate. The validation threshold can be configured with six validation schemes. The validation schemes and their logic gate configuration are shown in the table 5.2. An appropriate validation setting can optimise the data acquisition rate and filter most of the noise events, especially for application coupling scintillators [71].

Validation scheme	Gate 0	Gate 1	Gate 2	Gate 3	Gate 4	Gate 5	Gate 6	Sub-pixel connection
1-OR	OR	OR	OR	OR	OR	OR	OR	OR
2-OR	OR	OR	OR	AND	OR	OR	OR	OR
4-OR	OR	AND	OR	AND	OR	AND	OR	OR
8-OR	AND	AND	AND	AND	AND	AND	AND	OR
4-AND	OR	AND	OR	AND	OR	AND	OR	AND
8-AND	AND	AND	AND	AND	AND	AND	AND	AND

Table 5.2: Six validation schemes and the logic connections for each validation scheme.

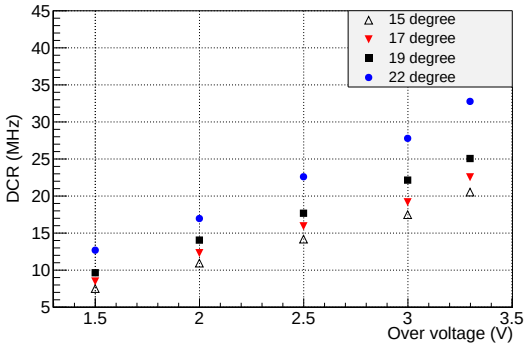

Figure 5.6: DCR of one die as function of over bias voltage at different temperature.

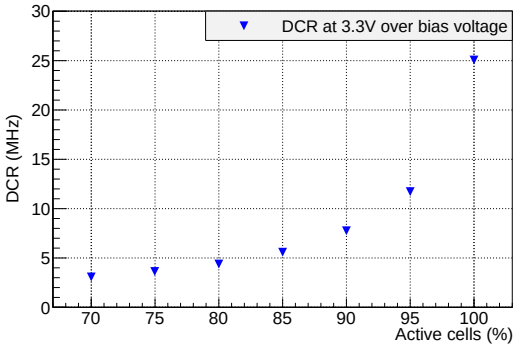

Figure 5.7: DCR as function of percentage of active cells for one die. The over bias voltage is 3.3 V. The temperature is 18 °C.

5.3 Basic characteristics of Philips digital photon counter

5.3.1 Breakdown voltage

The PDPC kit itself provides a method to measure the breakdown voltage, based on the current as a function of bias voltage. The breakdown voltage of sensor 1 (Tile 1) was found to be 22.65 V at 18 °C, while for sensor 3 (Tile 3) 22.62 V at 18 °C.

5.3.2 Dark count rate

The dark count rate of each SPADs can be measured by activating only one SPAD of the sensors, one after the other, and measure the DCR of the enable cell individually. The total DCR of the die is the sum of all the DCR values of each SPAD. As shown in figure 5.6, the DCR has a strong relation with the over bias voltage and temperature. The noise level of digital SiPM increases when increasing the over bias voltage and when increasing the temperature of the device. Figure 5.7 shows the DCR for different percentages of active cells. The DCR with 95% active cells is less than half the value for 100% active cells. As can be seen in figure 5.8, most of the cells in the die have a DCR value below 5 kHz and just few cells have DCR values exceeding 10 kHz. The DCR can be reduced a lot by just turning off

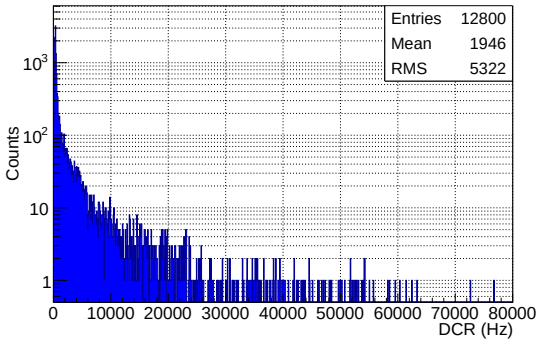

Figure 5.8: DCR distribution of the 12800 cells in one die. The over bias voltage of the chip is 3.3 V. The temperature is 18 °C.

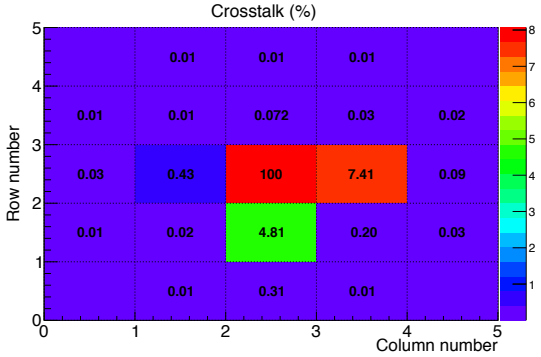

Figure 5.9: The crosstalk probability map of a centre SPAD cell.

the high noise cells with a marginal reduction of the PDE.

5.3.3 Crosstalk

Optical crosstalk happens when a photon generated in the avalanche process of one SPAD triggers a secondary avalanche in one of the neighbouring SPADs. The probability of crosstalk is directly related to the charge density in the junction of the SPAD. So the bias voltage applied to the SPAD and the geometry of the arrangement of the SPADs will affect the crosstalk. In order to characterise the crosstalk, I followed the same method as for the digital SiPM [53]. The advantage of activating only the selected cells allows directly to measure the crosstalk. A SPAD with high DCR in a low noise environment is selected as the photon source to trigger crosstalk to other SPADs. DCR values of each SPAD are measured to calculate the probability of randomly coincidence dark counts. Every time only the high DCR SPAD and one of the neighbour cell are activated. After substrating the calculated randomly coincidence dark counts, the crosstalk probability of that cell is calculated by the ratio:

$$P_{crosstalk} = \frac{Two\ photon\ events}{One\ photon\ events} \tag{5.1}$$

A 5×5 array of SPADs surrounding the high DCR SPAD were measured and the results

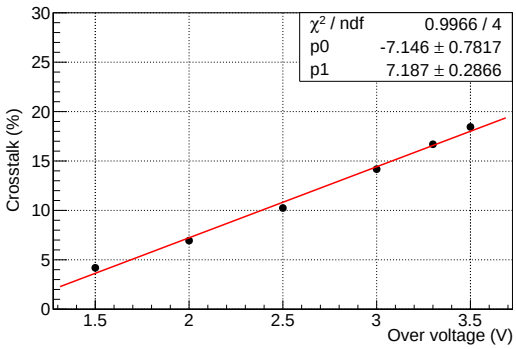

Figure 5.10: Crosstalk as function of over bias voltage.

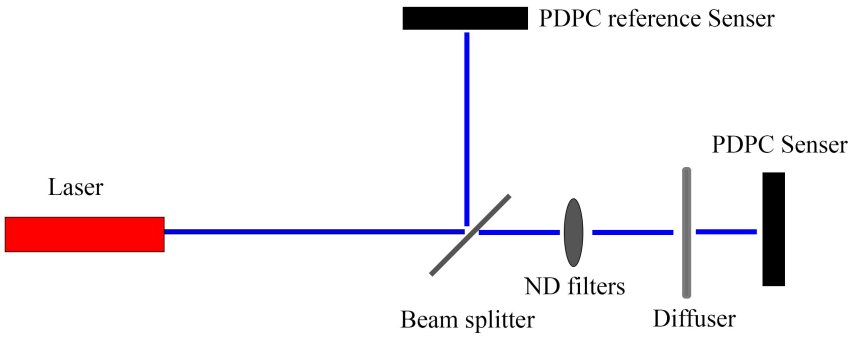

Figure 5.11: SPTR setup. All the measurements were performed at 18°C.

for each cell are shown in figure 5.9. As seen from the figure, the crosstalk probability is unsymmetric, which due to the designed geometry of the SPAD cells. Then we summed all the crosstalk probability of the 24 cells to get the crosstalk probability of the SiPM. The crosstalk for different over bias voltages is shown in figure 5.10. The crosstalk is linearly increasing with the over bias voltage, with the same trend as the analog SiPM one [19].

5.4 Single photon time resolution

5.4.1 Setup

A temperature controlled light tight box houses the digital SiPM. A Picosecond pulsed laser from PICOQUANT with 405 nm wavelength was used [61]. The temporal width of the laser light is 48 ps full width half maximum (FWHM). We used a repetition rate of 100 kHz for the laser since the maximum transmission rate between the field-programmable gate array (FPGA) and each die of the sensor is 120 kHz. The light spot of the laser has a diameter of 4 mm and a good uniformity of light was obtained by placing a diffuser after the laser beam. The scheme of the setup is shown in figure 5.11. The light from laser was split in two using a mirror. The reflected light was sent to the reference sensor, while the other half went to the PDPC under the test. In all the measurement the trigger threshold level was kept at the

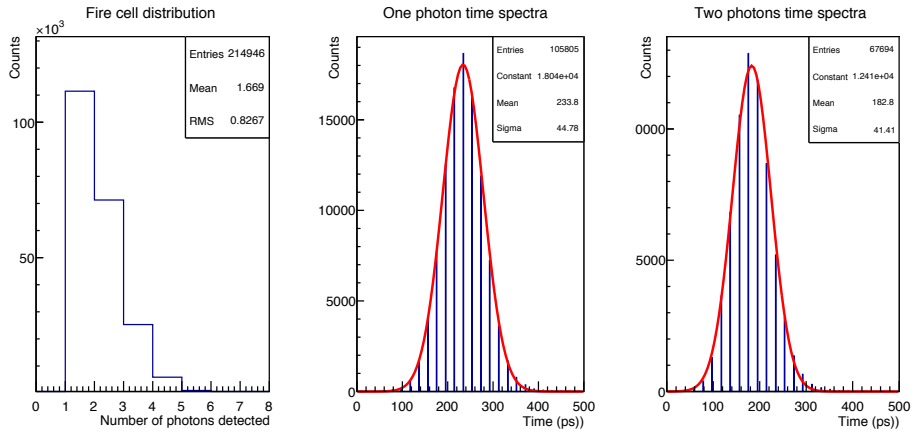

Figure 5.12: Histogram of the photon count for low intensity laser light (left), the single photon time spectra (middle) and the two photon time spectra (right).

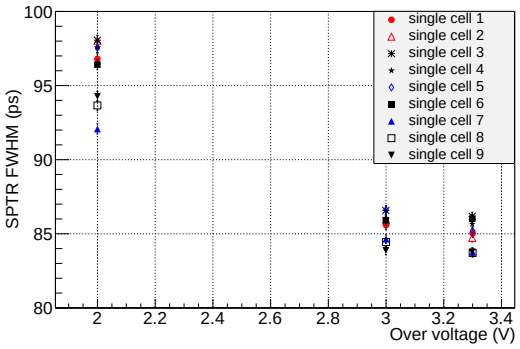

Figure 5.13: Time resolution of each cell at 1 photon level at 18 °C with different over voltage.

level of 1 photon to validate all events. The bias voltage of the reference sensor was kept constant during the entire measurement. A coincidence time resolution of 47 ps (FWHM) was measured between the two sensors when over 500 photons detected in both sensor. However, the laser light impinging the test sensor can be attenuated to the single photon level using a set of neutral density filter. for the single photon time resolution (SPTR) study, only 80% of the cells of pixel 2 of die 0 in the reference sensor has been activated in order to keep the total DCR below 2.0 MHz, to decrease the system dead time.

5.4.2 Single photon time resolution

The SPTR of the digital SiPM is the convolution of all the jitter sources, mainly the SPAD jitter, the SPAD non-uniformity and the trigger network skew [72]. To study the effect of the jitter sources, we measure the timing performance of the digital SiPM on a single SPAD level and on a pixel level.

The possibility of activating individual SPAD cells facilitates the characterization of the single SPAD cell for the SPTR. In the trigger network of the Philips digital SiPM there is a low-skew signal path from each cell to the TDC [72]. This skew is an important parameter

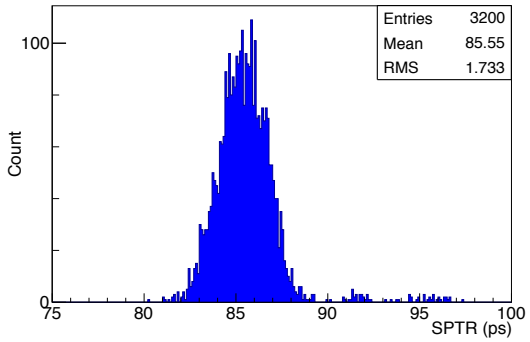

Figure 5.14: Distribution of SPTR for 3200 SPAD cells in one pixel.

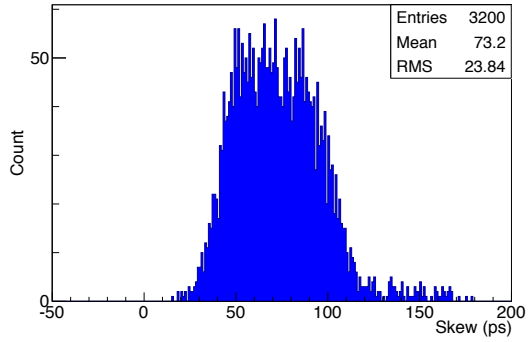

Figure 5.15: Distribution of skew for 3200 SPAD cells in one pixel.

affecting the single photon time resolution of the device. The relative signal propagation time of each SPAD cell can be extracted from the mean value of the time distribution.

Figure 5.12 shows the histogram of the photon counts for the attenuated laser pulse, together with the timing distribution after an offline selection of 1 photo electron event and 2 photon electrons event. A SPTR of 105.23 ps (FWHM) was extracted from the sigma of the gaussian fit of the time distribution in figure 5.12. The time resolution of multi-photons can also be measured by selecting events with a given number of the photons and extracting the sigma of a gaussian fit to the time distribution.

Firstly, I measured the SPTR at different over bias voltages for 9 different SPAD cells and the result is shown in figure 5.13. As can be seen in the figure, for these cells, the SPTR reaches a plateau when the over bias voltage is higher than 3 V. The SPTR of each cell in pixel 2 of die 0 has been measured at 3.3 V over bias voltage. The distribution of the SPTR for the 3200 cells in pixel 2 is shown in figure 5.14. The mean value of the SPTR for these cells is 85.55 ps (FWHM). Only few SPAD cells have SPTR values exceeding 90 ps (FWHM). The relative signal propagation time of each cell was extracted from the mean value of time histogram of each cell and the skew distribution of the 3200 cells is shown in figure 5.15. For these 3200 cells, the difference between the maximum skew and the minimum skew is less than 150 ps. A variation of 56.0 ps (FWHM) is obtained from the root mean square (RMS) of the distribution.

The SPTR of the pixel 2 (3200 SPAD cells) as a function of over bias voltage at different

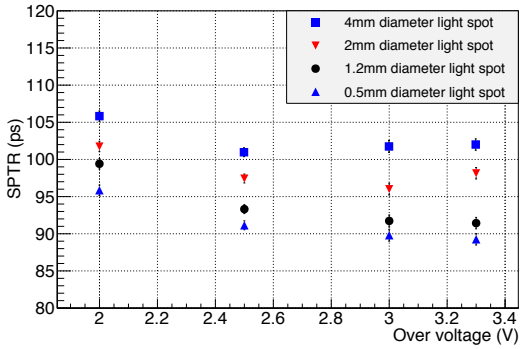

Figure 5.16: SPTR as a function of over voltage at different illuminating spot sizes. The temperature was 18 °C.

illuminating spot sizes was also measured. As shown in figure 5.16, the SPTR improves when less area of digital SiPM is being illuminated. This is due to the no uniformity of response of each cell electronics and to the trigger network skew. The SPTR I got when most of the cells of the pixel were illuminated is worse than the SPTR of a single SPAD. The SPTR value when only a spot with 0.5 mm diameter of the digital SiPM was illuminated is 88.6 ps, which is comparable to the SPTR value of a single SPAD. The mean value of the SPTR for all the 3200 SPAD cells in pixel 2 is represented as $\overline{\sigma_{SPAD}}$ and the skew variation of all the SPAD cells is expressed as σ_{skew}. From our measurement, the $\overline{\sigma_{SPAD}}$ can be estimated as 85.55 ps (FWHM) and the σ_{skew} is 56.02 ps (FWHM). By simply using a jitter transfer formula:

$$\sigma_{pixel} = \sqrt{\overline{\sigma_{SPAD}}^2 + \sigma_{skew}^2} \tag{5.2}$$

A value for σ_{pixel} of 102.26 ps is calculated, which is closed to the SPTR we have measured at 3.3 V when the whole pixel of digital SiPM is illuminated. I can conclude that the single photon time resolution of the pixel is mainly due to the contribution of SPAD jitter and of the signal skews from the SPADs to TDC.

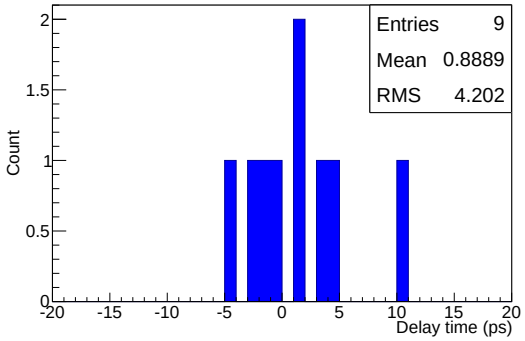

Figure 5.17: Distribution of the mean value of the delay time of each cell. The measurements were performed at 3.3 V over bias voltage and at 18°C.

Timing performance at different photon event level with 9 cells activated

Photon event	Timing jitter (FWHM) (ps)	Delay time (ps)
1	91.49±0.32	114.69±0.19
2	84.19±0.27	66.26±0.19
3	79.16±0.23	39.53±0.17
4	73.83±0.23	15.59±0.17
5	69.43±0.21	3.92±0.19
6	64.92±0.20	−17.51±0.17
7	60.89±0.28	−35.39±0.21
8	59.39±0.20	−45.41±0.16
9	58.19±0.17	-64.19±0.14

Table 5.3: Timing performance at different photon event level for 9 cells. The over bias voltage is at 3.3 V and temperate is at 18 °C.

5.4.3 Low photon number time resolution and crosstalk

In order to study the effect of the crosstalk on the timing performance of the Philips sensor, we attenuated the laser light using a set of neutral density filters and the over bias voltage of the test sensor was 3.3 V. The number of detected photons from the low flux of laser pulse should follow the poisson distribution [73]. Therefore we set the photon level to match to different poisson expected value (λ) of 0.015, 0.34 and 3.5, for which the ratio of two photons events to one photon events are 0.008, 0.16 and 1.58 respectively.

We selected a 3×3 array of cells, which have similar signal propagation time. This is shown in figure 5.17 (the difference is 15 ps between the earliest and the latest). The mean value of the SPTR of these cells at 3.3 V over bias voltage is 85 ps FWHM. We can conclude that these 9 cells have homogenous response.

The time resolution and the mean value of the event time of these 9 cells for different intensities of the laser light are shown in figure 5.18 and figure 5.19. In the measurement, 9 cells selected were turned on while the rest of the cells in the sensor were inhibited. For the response of the photon detector, N'th photon should improve the time resolution compare to the 1 photon time resolution [74]. We expect that the time resolution improves as the inverse of the number of photons. However, as shown in figure 5.18, the time resolution only improves for the events that are not mixed with the crosstalk. The delay time shifts to the earlier time as the detected number of photons increases. When the poisson expected value is 0.015, nearly no two photons would arrive to the SiPM in the same time. For very low μ (Poisson mean) events with 2 or 3 detected photons are mostly due to crosstalk or random coincidences. This is confirmed by the plot of figure 5.19 which one can see that the timing detected of arrival does not depend on the number of photons for low μ intensity. When the poisson expected value is 3.5, the two photons detected events are dominated by the two photons impinging to the SiPM from laser light. The degrading of timing of two photon events at $\mu = 0.34$ can be explained in figure 5.20. Due to the crosstalk and random coincidence, the two photon timing is degrading by the overlap of two different types of time distribution.

The factor affecting the timing response is the rise time of the signal as well as the trigger network skew. This is the same for the analog SiPM; for example the 2-photon timing can be as early as 200 ps compared to 1 photon event [75]. In order to understand better the influence

of these factors on the performance of the digital SiPM, I performed the measurements at SPAD level as described below. I changed the neutral density filter reach a light level of 9 photons to the 3×3 cell area. The timing performance was measured for each cell individually and the mixed time spectrum of the 9 cells is depicted in figure 5.21. It can be seen in the figure that for all the 9 cells the earliest timestamp is around 0 ps and the mean value of all cells is 95.03 ps. Then 9 cells were enabled together and the timing is been measured. The time spectrum of 9 SPAD cells triggered together is shown in figure 5.22. Mean value of delay time of 9-photon events is -64.19 ps and almost all timestamps are much earlier than 0 ps. This indicates the rise time of signal arrived to the TDC is changed when more than one signals arrived to the TDC in the same time and give a timestamp earlier than timestamp of individual cell. The summary of timing performance at different photon levels with 9 cells activated is shown in the table 5.3. The time resolution is getting better with the increasing of detected photons number. The time resolution reached 58.19 ps ± 0.07 ps when 9 cells have avalanches together.

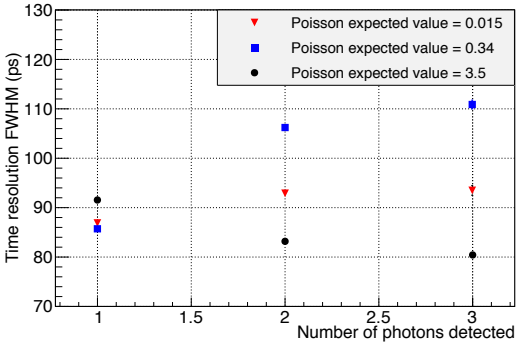

Figure 5.18: Time resolution with different photon level at 18 °C at 3.3 V over bias voltage.

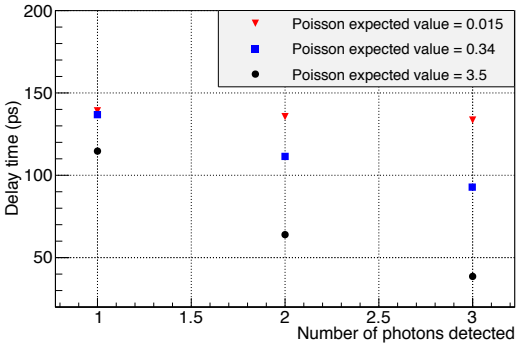

Figure 5.19: Delay time with different photon level at 18 °C at 3.3 V over bias voltage.

5.5 Time resolution from single photon to multi-photons.

The light intensity was changed by use different neutral density filter and was set to different levels of photons impinging to the digital SiPM. Figure 5.23 shows the results of measurement

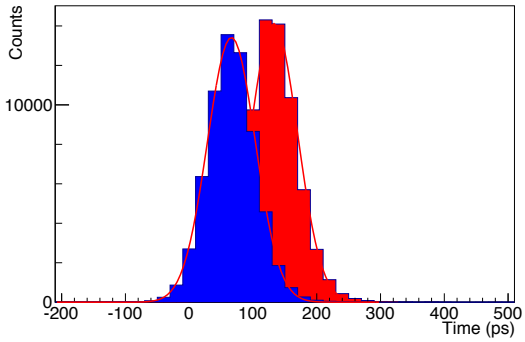

Figure 5.20: Red colour: time histogram of two photon events due to crosstalk and random coincidence. Blue colour: time histogram of two photon events due to two photons from laser light.

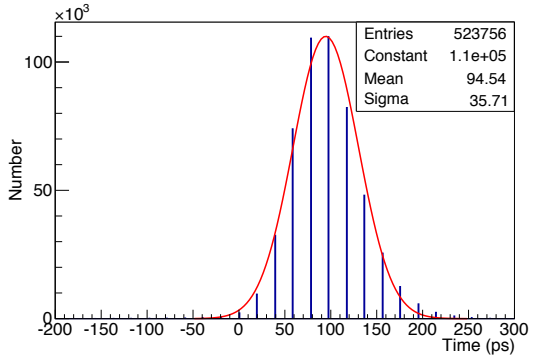

Figure 5.21: Time spectra of single cell at 18 °C at 3.3 V over voltage.

with different number of detected photons. The time resolution improves by increasing the number of photons from 1 to 110 (93 to 54 ps). The time resolution is getting better by the combination of sharper rise time and more statical of photons. This is the same as the analog SiPM. The delay time, which is the mean value of the time spectrum is shown in figure 5.24. As expected, the delay time is getting earlier as the increasing of the number of photon detected.

5.6 Conclusion

A evaluation for the DCR performance, optical crosstalk and single photon time resolution was performed. We have characterized the timing performance of the Philips Digital Silicon Photomultiplier with the trigger threshold of 1. The timing performance at SPAD level has also been studied. A mean value of 85 ps FWHM was obtained for SPTR of single SPAD. Mainly due to a low-skew signal path from each cell to the TDC in the trigger network of Philips digital SiPM, the SPTR of pixel (3200 SPADs) in the chip degrades to 102 ps. The measurement with very weak laser-light shows the SPTR value does not depend on the percentage of the crosstalk. However, if more than 1 photon are detected in the mean time then the timestamp registered in the TDC will be earlier than timestamp of single photon and the time profile depend on the difference of arriving time and number of photon detected. The time resolution from single photon to multi-photons is getting better, 93 ps to 54 ps.

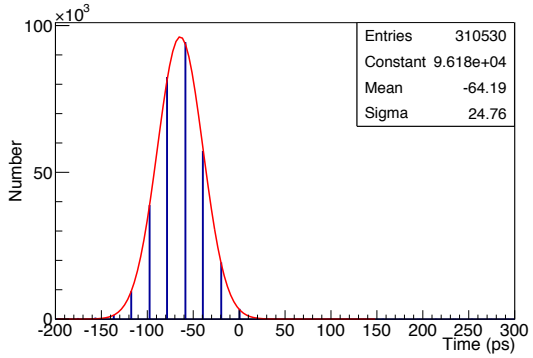

Figure 5.22: Time spectra at 9 photon event at 18 °C at 3.3 V over voltage.

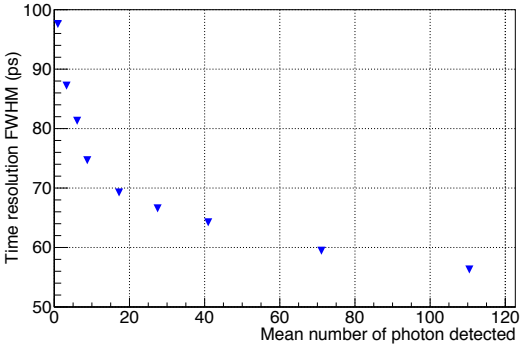

Figure 5.23: Time resolution with different level of detected photons. The sensor is operated at 3V over bias voltage and at 19°C.

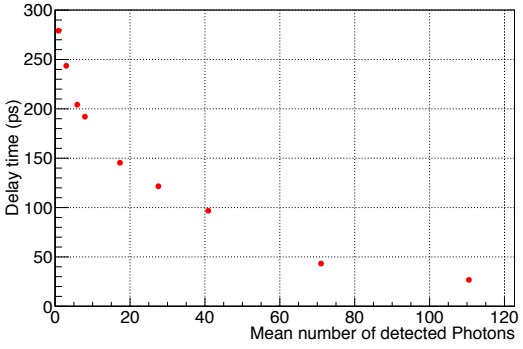

Figure 5.24: Delay time with different level of detected photons.The sensor is operated at 3V over bias voltage and at 19°C.

Chapter 6

Optimisation for energy resolution and CTR

Silicon Photomultipliers (SiPMs) are foreseen to be widely utilized in near future by Positron Emission Tomography (PET) scanners, thanks to their compactness, insensitivity to magnetic field and low operation voltage. Time of Flight (TOF) information has been shown to improve the performance of PET scanners. Analog SiPMs and digital SiPMs have already shown excellent timing performance when coupled to scintillators. A coincidence time resolution (CTR) of 108 ps full width half maximum (FWHM) has been achieved with 2×2×3 mm^3 LSO:Ce codoped 0.4%Ca coupled to Hamamatsu multi-pixel photon counter (MPPC) (S10931-050P) and NINO ASIC [23], [26]. The digital SiPM produced by Philips has been shown to provide CTR of 134 ps FWHM when coupled to 3×3×5 mm^3 Lutetium-yttrium oxyorthosilicate (LYSO) crystals [76].

In PET systems, scintillators and detectors are often arranged in the shape of arrays. In these configurations, the scintillating light produced by each crystal can be detected by multiple channels of the detector array [4], [5]. In general, because of the large angular distribution of light emitted by a scintillator [6], the photons produced by a single crystal have a chance to hit the detector over an area larger than the cross section of the crystal itself. Digital SiPMs have the advantage of allowing the user to select the active area of the detector, by enabling or disabling the single photon avalanche diodes (SPADs). In this paper, we present a study on the influence of choosing different active areas on the energy resolution and CTR for the Philips digital SiPM.

6.1 Setup

The performance of digital SiPM was investigated by means of the experimental setup shown in figure 6.1. Two sets of LYSO crystals produced by Crystal Photonics, Inc. (CPI) were tested. The crystals of one set have the same cross section of 2×2 mm^2, but different lengths of 5 mm, 10 mm, 15 mm and 20 mm. The crystals of another set of have the same length of 15mm, but different cross sections of 1.5×1.5 mm^2, 2×2 mm^2, and 3×3 mm^2. Each crystal was glued to the digital SiPM by means of Dow Corning RTV 3145 [58], and can be either fully wrapped with Teflon or left without any wrapping. All crystals were glued in the centre of pixel 1 in die 3 of the digital SiPM as shown in figure 5.3. In order to measure CTR, two crystals were placed facing each other at a distance of 5 cm, and a ^{22}Na source, 3 MBq

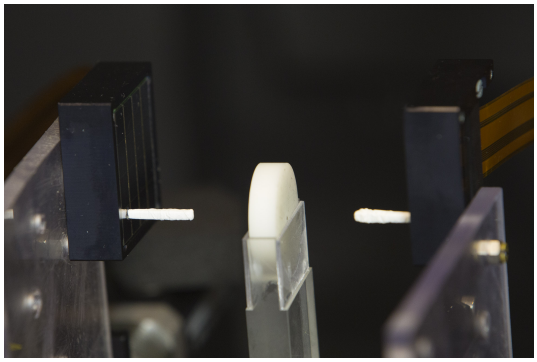

Figure 6.1: Setup for scintillating crystal measurement. All measurements were performed at 18°C inside a dark box.

activity, was placed halfway between the two crystals. In the energy and CTR measurement, to suppress the DCR of the digital SiPM, only the pixel 1 directly coupled to the crystal was enabled, while other areas of the digital SiPM were disabled.

6.2 Crystal position identification and active area selection

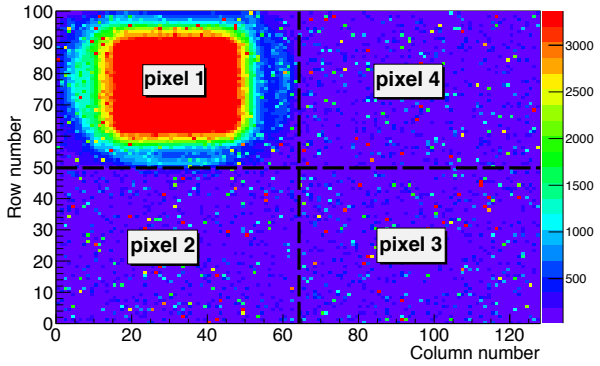

Figure 6.2: Photon count rate map of single LYSO crystal with dimension of 2×2×15 mm^3 glued on the Philips digital SiPM. The crystal was fully wrapped with Teflon. The measurement was performed at 2 V over bias voltage and the temperature was 18°C.

The position of the crystal coupled to the digital SiPM was identified by the photon count rate map recorded by the digital SiPM itself. A ^{22}Na source was positioned in front of the crystal and a 2 V over bias voltage was applied to the digital SiPM. The photon count rate was measured on SPAD-by-SPAD basis. We sequentially enabled single SPAD cells of the chip, one after the other, and measured the number of photons detected by each SPAD during the same amount of time. There was no crosstalk in these measurements since only one SPAD cell was activated during each data take. As shown in figure 6.2, from the photon count rate map it is straightforward to identify the position of the crystal coupled to the detector (red area). At the same time, it is clear that some optical photons interact with the digital SiPM also outside of the area of physical coupling between crystal and detector, as an

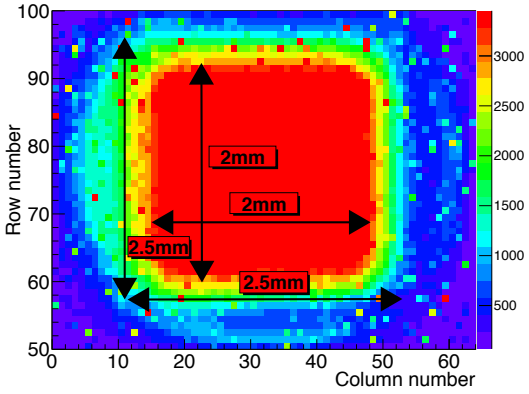

Figure 6.3: Plot of photon count rate map of one pixel of the Philips digital SiPM. A single 2×2×15 mm^3 LYSO crystal glued on it. The crystal was fully wrapped with Teflon. The measurement was performed at 2 V over bias voltage and the temperature was 18 °C.

effect of the large angular distribution of the photons emitted by the scintillator.

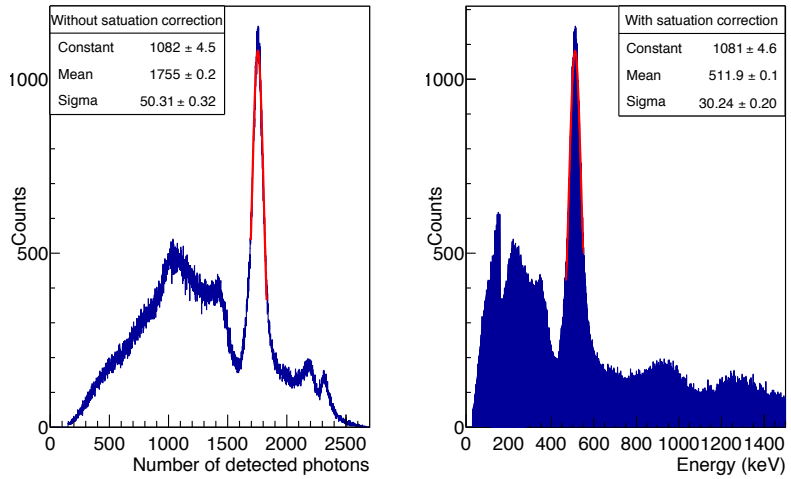

Figure 6.4: Left: ^{22}Na spectra with 2×2×15 mm^3 LYSO crystal at 3.3 volt over bias voltage with 100% cells activated. Right: Saturation corrected energy spectra of left ^{22}Na spectra. The measurements were performed at 18 °C.

Figure 6.3 shows the dimensions of one pixel and the dimensions of the crystal. As mentioned before, the pixel dimension for the digital SiPM is 3.2mm × 3.8775mm, while the cross section of the crystal is 2×2 mm^2, corresponding to the red square in figure 6.3. In our study we selected 7 different areas of SPAD activation, all centred on the crystal position, with the following dimensions: 1.6×1.6 mm^2, 1.8×1.8 mm^2, 2×2 mm^2, 2.2×2.2 mm^2, 2.5×2.5 mm^2, 2.8×2.8 mm^2, and the entire pixel 1 of die 3. An example of a 2.5×2.5 mm^2 square selection area is also shown in figure 6.3.

6.3 Energy resolution and light yield output

The variation of energy resolution and number of photons detected as a function of the different active areas of the digital SiPM has been studied. From the measurements we found that, without saturation correction, the energy resolution reaches the best values when over bias voltage is set to 3.3 V and 100% of the SPAD cells are enabled, which is in agreement with measurements reported by other groups [77]. Also, the energy resolution was found to be better in teflon wrapping configuration with respect to no wrapping condition. Therefore, for the purpose of the energy resolution investigation, the over bias voltage was fixed at 3.3 V and 100% of the cells in the selected digital SiPM area were activated, while the crystals were fully wrapped with Teflon.

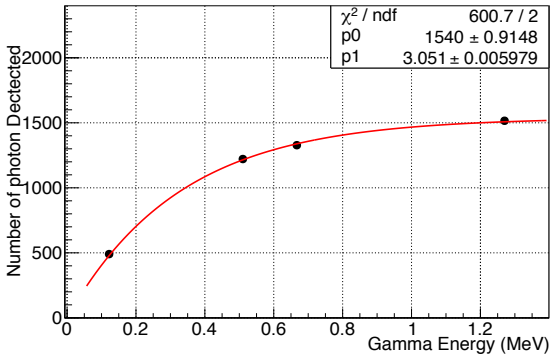

Figure 6.5: Light output of 2×2×15 mm^3 LYSO crystal coupled to digital SiPM with 2.5×2.5 mm^2 active area for different gamma energies. The measurements were performed at 3.3 V over bias voltage and the temperature was 18 °C.

The left plot of figure 6.4 shows the ^{22}Na spectrum of a 2×2×15 mm^3 LYSO crystal. Both 511 keV peak and 1270 keV peak can be clearly identified. The energy resolution for 511 keV in this plot is 6.7%, as can be deduced from a gaussian fit of the peak itself. However, this value of energy resolution has not been corrected for the saturation effect due to the finite number of cells available in the digital SiPM. In order to perform such a correction, we acquired the data with the same setup exciting the scintillator with three different gamma sources, ^{57}Co, ^{22}Na and ^{137}Cs. Then we extracted the mean number of photons detected by the digital SiPM for the four different gamma peaks provided by the sources, i.e. 117 KeV, 511 KeV, 667 KeV, and 1270 KeV. For digital SiPMs, under the assumption that each SPAD cell cannot detect more than one photon during the acquisition of a single scintillation event, a simple equation can be used to describe the saturation effect [53]:

$$N_{detected} = N_{cells}\left(1 - e^{-\frac{N_{photons}}{N_{cells}}}\right) \tag{6.1}$$

where $N_{detected}$ is the number of photons detected by the digital SiPM and $N_{photons}$ is the real number of photons that would interact with the digital SiPM if there was no saturation effect. N_{cells} represents the total number of active cells of the digital SiPM. If we express the number of photons emitted by the crystal, per unit energy of the incident radiation, as LY, the probability of a photon hitting the detector to be actually detected as photon

detection efficiency (PDE), and we introduce a factor η taking into account the optical coupling efficiency between the crystal and the detector, we can express $N_{photons}$ as

$$N_{photons} = PDE \times LY \times \eta \times E_\gamma \tag{6.2}$$

where E_γ is the energy of the gamma source. Equation 6.1 therefore becomes

$$N_{detected} = N_{cells}\left(1 - e^{-\frac{PDE \times LY \times \eta \times E_\gamma}{N_{cells}}}\right) \tag{6.3}$$

The parameters PDE, LY and η remain constant for a given experimental setup, so they can be collectively grouped in a factor $C = PDE \times LY \times \eta$, yielding to

$$N_{detected} = N_{cells}\left(1 - e^{-E_\gamma \frac{C}{N_{cells}}}\right) \tag{6.4}$$

By inverting this equation, it is easy to find a relation to derive $N_{photons}$ when a given number $N_{detected}$ is detected by the SiPM

$$C \times E_\gamma = N_{photons} = -N_{cells} \times \ln\left(1 - \frac{N_{detected}}{N_{cells}}\right) \tag{6.5}$$

Equation 6.4 can be used to derive the parameters C and N_{cells}, by fitting to the experimental points in plots like the one in fig. 6.5, where the number of photons detected by the SiPM is plotted against the energy of the gamma source. In this measurement, the detection area enabled on the SiPM is 2.5×2.5 mm^2. The N_{cells} parameter can then be used with Eq. 6.5 to derive the value of impinging $N_{photons}$ for each recorded events, enabling to plot non-saturated energy spectra like the one shown in the right plot of figure 6.4, for a ^{22}Na source.

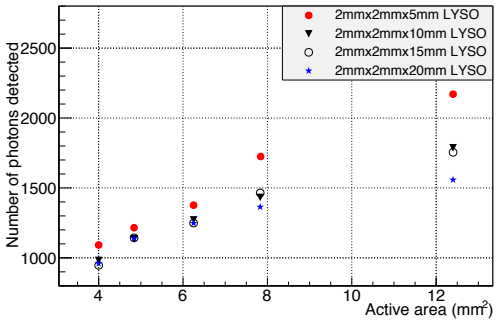

Figure 6.6: Number of photons detected by using different active area of digital SiPM. The measurements were performed at 3.3 V over bias voltage and the temperature was 18 °C.

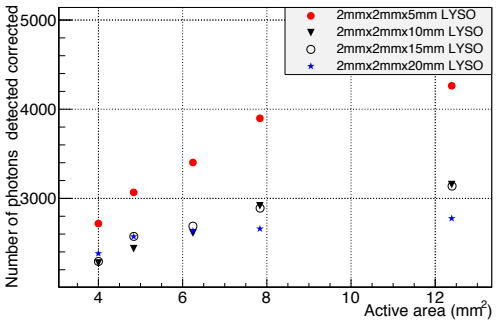

Figure 6.7: Number of photons impinging to the SiPM by using different active area of digital SiPM after saturation correction. The measurements were performed at 3.3 V over bias voltage and the temperature was 18 °C.

The number of photons detected and number of photons impinging on the SiPM as a function of different active areas of the digital SiPM, for crystals of different lengths, are shown in figure 6.6 and figure 6.7. Both with and without saturation correction, the number

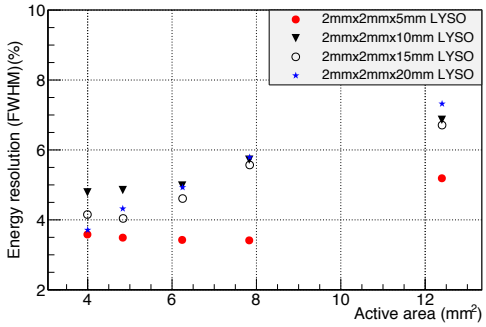

Figure 6.8: Energy resolution without correction by using different active area of digital SiPM. The measurements were performed at 3.3 V over bias voltage and the temperature was 18 °C.

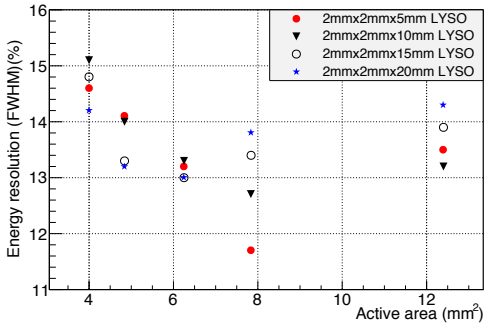

Figure 6.9: Energy resolution with saturation correction by using different active area of digital SiPM. The measurements were performed at 3.3 V over bias voltage and the temperature was 18 °C.

Dimension of CPI-LYSO (mm^3)	1.5×1.5×15	2×2×15	3×3×15
Energy resolution not corrected (FWHM)(%)	4.97	4.04	4.83
Energy resolution saturation corrected (FWHM)(%)	15.1	13.0	10.3
Energy resolution measured with PMT (FWHM)(%)	11.5	12.1	10.8
Number of photons detected	1045	1754	2180
Number of photons impinging to the SiPM	1757	3138	3882

Table 6.1: Energy resolution of different cross sections of LYSO crystals. The energy resolution not corrected and saturation corrected shown in the table are the best value while choosing the optimal active area of digital SiPM for the glued crystals. The Number of photons detected and saturation corrected shown in the table are the acquired number when the active area is the total pixel.

of photons detected by the SiPM increases when the active area is increased. Figure 6.8 and figure 6.9 show the variation of the energy resolution as a function of different active areas of the digital SiPM, for crystals of different lengths. The energy resolution without saturation correction shows an improvement when the active area of the digital SiPM is decreased. On the other hand, the energy resolution after saturation correction does not follow the same trend. For instance, the 2×2×5 mm^3 crystal achieves the best energy resolution value of 11.7% when the active area is 2.8×2.8 mm^2. For the scintillators we measured, the active area that optimizes the energy resolution was found to be neither the physical coupling area, nor the largest area of digital SiPM, but an area close to the average between the two. The values of energy resolutions obtained with the digital SiPM were also compared to measurements carried out with photomultiplier tubes (PMTs). All crystals investigated in this study, fully wrapped with Teflon, were measured coupled to an Hamamatsu PMT R2059 [78] by means of RTV 3145. The energy resolution (FWHM) obtained with the PMT for crystal lengths of 5mm, 10mm, 15mm, 20mm was found to be 10.7%, 11.6%, 12.1%, 12.5%, respectively. These values are comparable to the energy resolutions measured by the digital SiPM in the best active area configuration (see figure 6.9).

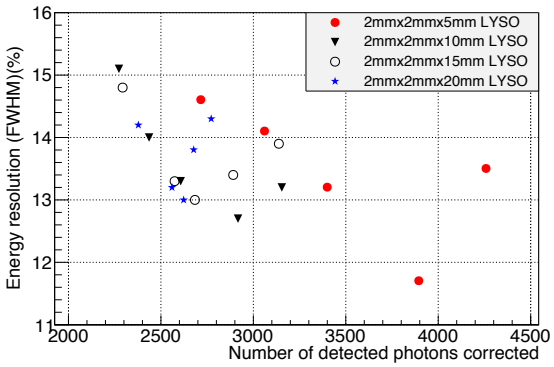

Figure 6.10: Correlation plot of number of photons impinging to the SiPM and energy resolution after saturation correction for different LYSO crystals. The measurements were performed at 3.3 V over bias voltage and the temperature was 18 °C.

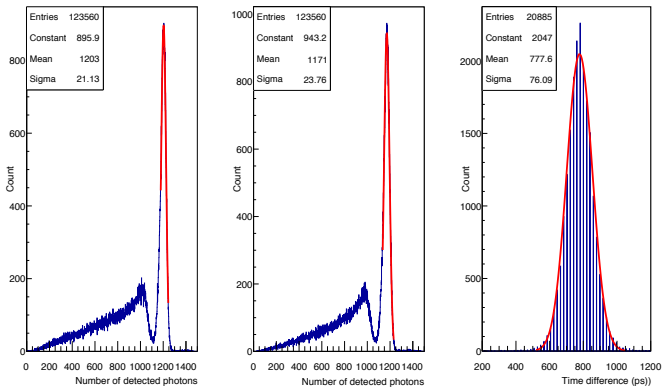

Figure 6.11: Coincidence time resolution plot of two 2×2×20 mm^3 LYSO crystals coupled to digital SiPM. The measurement was performed at 3.3 V over bias voltage and the temperature was 18 °C.

The variation of energy resolution as a function of the cross section of the LYSO crystal was also investigated. We obtained the best energy resolutions, after saturation correction, with the same optimal active area that was found in the previous part of this study. Table 6.1 summarizes the measurement results for digital SiPM and PMT. As shown in the table, the energy resolution measured by digital SiPM after saturation correction improves when the cross section area of the crystal is increased. This reflects the increasing number of photons detected when the section of the crystal becomes larger. However, the energy resolution measured by the PMT shows little variation when the cross section of crystals is increased, and the values obtained for 1.5×1.5×15 mm^3 and 2×2×15 mm^3 crystals are consistently better with respect to the ones measured by the digital SiPM.

For the same crystal, without saturation correction, activating a smaller area of the digital SiPM improves the energy resolution. This can be explained by considering that most of the scintillating photons are impinging on the detector inside the area of physical coupling between crystal and SiPM where the saturation effect is larger, resulting in an

spurious compression of the photopeak. The energy resolution with saturation correction is however the most important parameter to be taken into account, as it reflects the real energy discrimination capability of the system. This is shown to improve when the active area is larger than the area of physical coupling between crystal and detector, because more cells of digital SiPM are involved in the detection and therefore more photons from the scintillating light are collected, as shown in figure 6.10, improving the statistical contribution to the energy resolution. After having reached the best energy performance, the energy resolution is then limited by the noise of digital SiPM and by crosstalk, which explains the degradation of energy resolution when the active area is further increased.

6.4 Coincidence time resolution

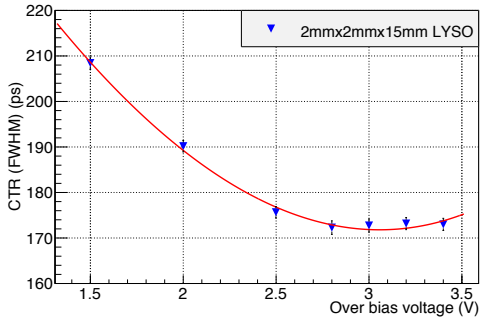

Figure 6.12: Coincidence time resolution with different over bias voltage of 2×2×15 mm^3 LYSO crystal. The measurements were performed when 100% in cells one pixel is enabled. The temperature was 18 °C.

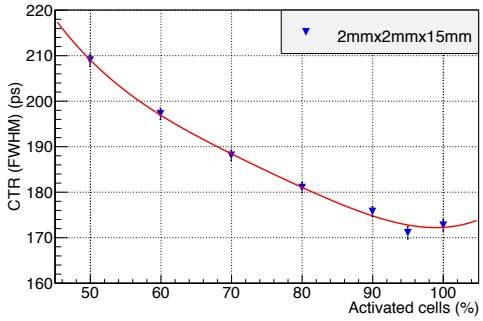

Figure 6.13: Coincidence time resolution with different level of activated cells of 2×2×15 mm^3 LYSO crystal. The measurements were performed at 3.5 V over bias voltage and the temperature was 18 °C.

Figure 6.11 shows a typical energy spectrum and a coincidence time difference histogram for two identical LYSO crystals with dimensions of $2 \times 2 \times 20\ mm^3$ coupled to the digital SiPM. All the events within one sigma of the gaussian fit of the photon peak were selected and their coincidence time differences were histogrammed in the time spectrum. A gaussian fit was performed on this resulting histogram and the CTR was extracted. CTR measurements with different bias voltage and different percentage of active cells were performed to find the

Crystal dimension (mm^3)	CTR (FWHM)(ps)
1.5×1.5×15	172.68±2.42
2×2×15	171.59±2.18
3×3×15	170.67±1.95

Table 6.2: CTR for different cross sections of LYSO crystals.

optimal configuration for the timing study. The results are shown in figure 6.12 and figure 6.13. As the two plots indicate, the CTR improves with increasing over bias voltage and reaches a plateau when the over bias voltage becomes larger than 3 V. The CTR reaches the best value when 95% of cells are activated. For CTR measurements with LYSO crystals, the over bias voltage was fixed at 3.5 V and 5% of the cells with high DCR values were disabled.

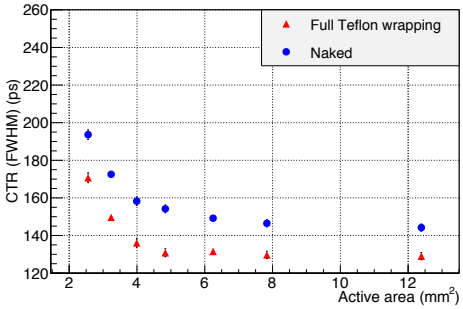

Figure 6.14: Coincidence time resolution for LYSO crystal with dimension of 2×2×5 mm^3 at different sizes of digital SiPM active area. The measurements were performed at 3.5 V over bias voltage and the temperature was 18 °C.

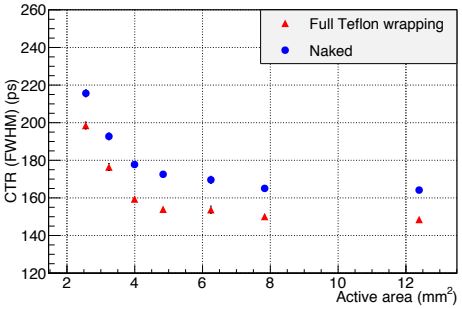

Figure 6.15: Coincidence time resolution for LYSO crystal with dimension of 2×2×10 mm^3 at different sizes of digital SiPM active area. The measurements were performed at 3.5 V over bias voltage and the temperature was 18 °C.

The variation of CTR with crystal length, for crystal cross section of 2×2 mm^2, is shown in figures 6.14 to 6.17. In the configuration without Teflon wrapping, to make sure no photon exiting from the lateral faces of the crystal impinges on the digital SiPM, a black holder with 2×2 mm^2 square hole was attached to the crystal itself. The CTR deteriorates when the length of the crystal is increased, for both teflon wrapping and no wrapping configuration. This is the same trend that was found in analog SiPMs [26]. For different dimensions of crystals, the CTR reaches the best values when the active area is larger than 2.2×2.2 mm^2, improving by 8-10 ps with respect to the condition where an active area of 2×2 mm^2 is set. This can be explained by recalling, as shown in figure 6.6 and figure 6.7, that the number of photons detected increases when a larger area of digital SiPM is activated. Photo-statistics can greatly impact the timing resolution, and a strong correlation between the crystal light output and timing resolution has already been demonstrated in our previous study [64]. However, when the active area is increased further than 2.2×2.2 mm^2, little effect on the CTR can be detected.

The CTR of 15 mm length LYSO crystals was also measured as a function of different crystal cross sections. The best CTR obtained for each cross section, when the active area of digital SiPM is optimized, is shown in table 6.2. As the difference in CTR between the cross

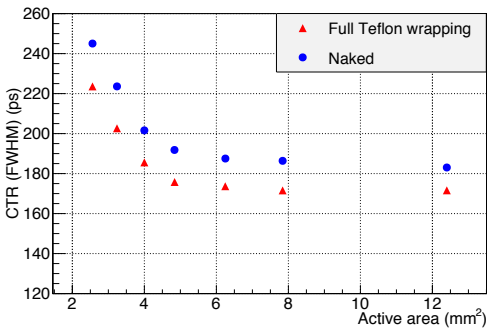

Figure 6.16: Coincidence time resolution for LYSO crystal with dimension of 2×2×15 mm^3 at different sizes of digital SiPM active area. The measurement were performed at 3.5 V over bias voltage and the temperature was 18 °C.

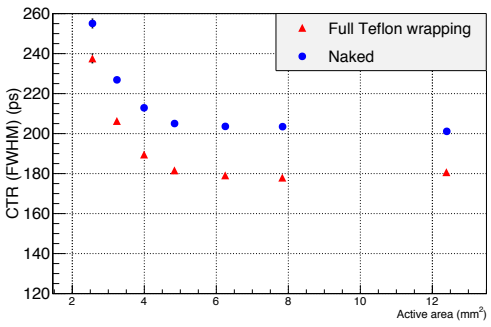

Figure 6.17: Coincidence time resolution for LYSO crystal with dimension of 2×2×20 mm^3 at different sizes of digital SiPM active area. The measurement were performed at 3.5 V over bias voltage and the temperature was 18 °C.

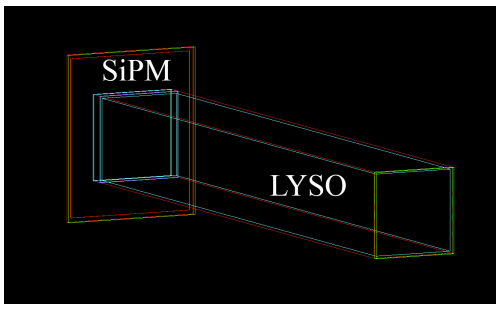

Figure 6.18: Schematic of the Geant4 simulation model.

sections investigated is negligible, we can conclude that CTR is independent on the physical coupling area between crystal and digital SiPM.

We performed a Geant4 [79] simulation study in order to understand the behaviour of CTR when using different active areas of digital SiPM. A physical volume of silicium, 3.2 × 3.8775mm^2 to simulate the digital SiPM together with a LYSO crystal are included in the simulation geometry, as shown in figure 6.18. X-axis and Y-axis are oriented along the plane of the SiPM, while and Z-axis is oriented along the main axis of crystal. The LYSO crystal surfaces were defined as optically polished, and the crystal can be either fully wrapped with Teflon or left without any wrapping. The properties of simulated LYSO material are shown in Table 6.3. The intrinsic light yield represents the number of optical photons created per unit of deposited energy. The rise time and decay time give shape to the scintillation pulse. A glass

Intrinsic light yield (ph/MeV)	Rise time (ps)	Decay time (ns)
40000	100	40

Table 6.3: Properties of LYSO crystal simulated. The parameters are taken from [64], [80].

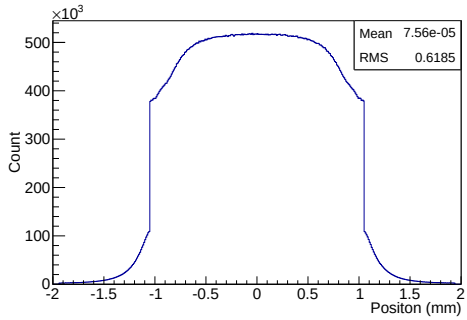

Figure 6.19: Simulation result of $2\times2\times20\ mm^3$ LYSO crystal. The plot is the position distribution of output scintillating light.

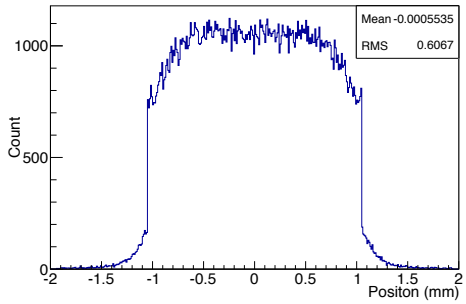

Figure 6.20: Simulation result of $2\times2\times20\ mm^3$ LYSO crystal. The plot is position distribution of output scintillating light in the first 200 ps.

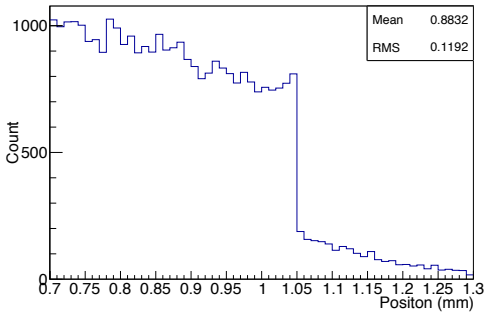

Figure 6.21: Zoom of position distribution of output scintillating light in the first 200 ps.

volume of 0.2 mm thickness is placed between the crystal and SiPM and is coupled with them by means of with optical glue. A source of gamma, 511 keV energy, is placed approximately 10 cm far from the crystal, on the opposite side of the SiPM. 10^5 gamma interactions with the scintillator are simulated for each configuration of LYSO crystal coupled to digital SiPM previously studied. Saturation effects are not considered and we consider the PDE of digital SiPM as 28%, based on the values reported in [53].

Figure 6.19 and figure 6.20 show the simulation results for a $2\times2\times20\ mm^3$ LYSO coupled to the digital SiPM, without any wrapping. In figure 6.19, a histogram of the impact position on the digital SiPM along the Y-axis of the optical photons is shown, for events in the 511 keV photopeak.

As it is very well known, the first photons arriving on the SiPM give rise to the most important contribution to the timing resolution. Figure 6.20 shows an histogram of the impact position on the digital SiPM along the Y-axis of the optical photons arriving in the first 200 ps of every detection process.

Both these plots show, as expected, that most of scintillating light impinges on the SiPM in the area of physical contact between crystal and detector. Outside this area, the number of collected photons has a sharp decrease. Figure 6.21 shows that most of the photons reaching the SiPM in the first 200 ps are contained in a range going from -1.05mm to 1.05mm. Moreover, as shown in figure 6.22 and figure 6.23, the number of scintillating photons detected

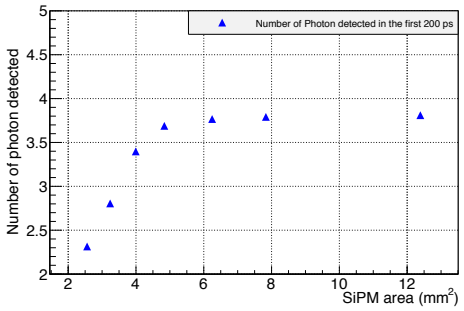

Figure 6.22: Simulation result of 2×2×20 mm^3 LYSO crystal. The plot is number of photons detected in the first 200 ps for different active area.

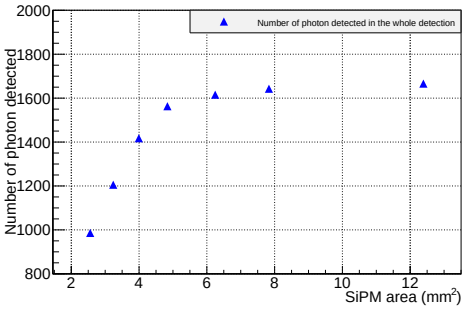

Figure 6.23: Simulation result of 2×2×20 mm^3 LYSO crystal. The plot is number of photons detected in the total scintillation process for different active area.

during the first 200 ps increases when the active area is increased from 1.6×1.6 mm^2 to 2.2×2.2 mm^2, and reaches a plateau for areas larger than 2.5×2.5 mm^2. The same trend can be seen also for the number of photons impinging on the SiPM. This is in good agreement with the experimental measurements of CTR reported in figure 6.17.

Furthermore, we separated the SiPM into the different regions based on the active area, as shown in figure 6.24. Region A is the area included in a square with dimensions 1.6×1.6 mm^2, region B is the area between region A and a square of dimensions 1.8×1.8 mm^2, and so on. The ratio of the number of photons detected in the first 200 ps to the number of photons detected in the total scintillation process for these different regions of the SiPM is shown in figure 6.25. The ratio in regions A, B and C is at the level of 0.25%, and decreases from D to G. Since the CTR is strongly related to the first photons arriving on the SiPM, the CTR resolution is dominated by the regions that present a high ratio in figure 6.25, while the remaining regions have little effect on the CTR. Simulations performed on the other crystal lengths show similar results to the ones obtained for a 2 × 2 × 20 mm^3 LYSO crystal. We can therefore conclude that collecting the photons that impinge on the SiPM outside of the area of physical coupling between crystal and detector can improve the CTR.

6.5 Conclusion

A set of LYSO crystals with different dimensions have been studied using different active area of the digital SiPM produced by Philips. We have found active areas larger than the area of physical coupling between crystal and detector can improve the energy resolution, because of the increased number of optical photons collected. We have also found that the cross section of the crystal has an impact on the energy resolution, with larger areas yielding better results. Moreover, the digital SiPM coupled to LYSO crystals with 2×2 mm^2 and 3×3 mm^2 cross section, can reach energy resolution levels comparable to the ones recorded by PMTs. The CTR measured with the digital SiPM coupled to LYSO crystals reached the same values that were previously reported with analog SiPMs. We found that the CTR can be improved by 8-10 ps when an active area of 2.2×2.2 mm^2 is used for the digital SiPM, rather than a 2×2 mm^2 active area matching exactly the LYSO crystal cross section. This can be explained by an improved collection of the first optical photons impinging on the

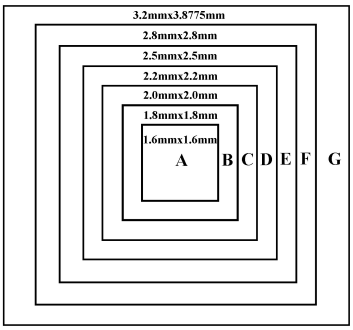

Figure 6.24: Schematic of the different regions of SiPM we selected.

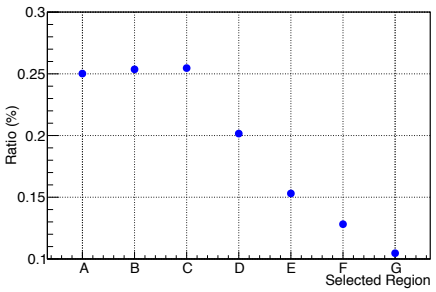

Figure 6.25: The ratio of the number of photons detected in the first 200 ps to the number of photons detected in the total scintillation process in different regions. The ratio is calculated from the simulation result of $2 \times 2 \times 20\ mm^3$ LYSO crystal.

detector, as was shown by Geant4 simulations. This leads to our conclusion that the energy resolution and CTR can be improved by optimizing the coupling between crystal and SiPM to extract more scintillating photons.

Chapter 7

Summary and conclusion

A fully characterisation of 256 Hamamatsu MPPC arrays (S12643-050CN) was performed to understand their intrinsic properties. This SiPM shows a uniformity of breakdown voltage, homogeneous gain of SPADs, and low noise performance. A reference of breakdown voltage, operation voltage, and the signal trigger level for all MPPC arrays was studied for the optimal parameter for the further operation of EndoTOFPET detector. An average CTR value of 239 ps FWHM has been measured for the 256 modules ($3.5\times3.5\times15$ mm^3 LYSO crystals + MPPC array). For such a large number of readout units (crystals + MPPC array), such performance is very promising and close to our target value of 200 ps. The CTR can be improved by reducing the size of LYSO crystal to $3\times3\times15$ mm^3, to match the size of MPPC. Crosstalk between the channels of HPTDC was measured due to the spread light from the scintillating crystal. This should be considered in the further design of the readout chip of EndoTOFPET-US scanner to optimise the timing performance.

The multichannel digital SiPM (MD-SiPM) chip designed by Delft University of Technology for the endoscopic probe for the EndoTOFPET US project was evaluated. The DCR level of this chip is significantly high comparing to the MPPCs. However, the DCR can be reduced by the trade off of the losing PDE of the chip. The 511 keV photopeak was obtained by coupled 4×4 LYSO crystal matrices of size $0.7\times0.7\times10$ mm^3 to the chip. An energy resolution of 18.26 % (nonlinear) FWHM of 511 keV was achieved. This bad energy resolution is due to the high DCR of MD-SiPM and limited dynamic range (416 SPADs).

A evaluation for the DCR performance, optical crosstalk and single photon time resolution of digital SiPM developed by Philips was performed. I have characterised the timing performance of the SiPM with the trigger threshold of 1. The timing performance at SPAD level has also been studied. A mean value of 85 ps FWHM was obtained for single SPAD SPTR of measuring 3200 SPADs. Mainly due to a low-skew signal path from each cell to the TDC in the trigger network of Philips digital SiPM, the SPTR of pixel (3200 SPADs) in the chip degrades to 102 ps. The measurement with very weak laser light shows the SPTR value does not depend on the percentage of the crosstalk. However, if more than 1 photon are detected in the mean time then the timestamp registered in the TDC will be earlier than timestamp of single photon and the time profile depend on the difference of arriving time and number of photon detected. The time resolution from single photon to multi-photons is getting better, 93 ps to 54 ps.

A performance summary for the three tested SiPMs is shown 7.1. The Hamamatsu MPPC has the lowest noise level among the three SiPMs. However, the crosstalk probability of MPPC is much higher than others. The Philips PDPC have a PDE quite close to the

MPPC, but the PDE of MD-SiPM is relatively much lower. Philips PDPC has a best SPTR value of 102 ps and energy resolution. The CTR for the MPPC and PDPC is quite close.

A set of LYSO crystals with different dimensions have been studied using different active area of the digital SiPM produced by Philips. I have found active areas larger than the area of physical coupling between crystal and detector can improve the energy resolution, because of the increased number of optical photons collected. I have also found that the cross section of the crystal has an impact on the energy resolution, with larger areas yielding better results. Moreover, the digital SiPM coupled to LYSO crystals with 2×2 mm^2 and 3×3 mm^2 cross section, can reach energy resolution levels comparable to the ones recorded by PMTs. The CTR measured with the digital SiPM coupled to LYSO crystals reached the same values that were previously reported with analog SiPMs. I found that the CTR can be improved by 8-10 ps when an active area of 2.2×2.2 mm^2 is used for the digital SiPM, rather than a 2×2 mm^2 active area matching exactly the LYSO crystal cross section. This can be explained by an improved collection of the first optical photons impinging on the detector, as was shown by Geant4 simulations. This leads to our conclusion that the energy resolution and CTR can be improved by optimising the coupling between crystal and SiPM to extract more scintillating photons.

Type of SiPM	MD-SiPM	Philips PDPC	MPPC (S12643-050CN)
DCR (MHz/mm^2)	78.43	0.44	0.09
Crosstalk (%)	10	17.4	43.8
peak PDE (%)	12.5 (V_{ov}=3.0V)	30.0 (V_{ov}=3.3V)	37.5 (V_{ov}=3V)
SPTR (FWHM) (ps)	285	102	251
Energy resolution (%)	15.7	11.6	13.1
CTR (FWHM) (ps)	-	170.7	170.2

Table 7.1: Performance summary of the three different SiPMs studied in the PhD work. The value of DCR, crosstalk and PDE are all based on the optimal operation bias voltage for the CTR measurement. The value of energy resolution and CTR are based on the measurement of 3×3×15 mm^3 LYSO crystals. Some values are taken from [67], [53], [81].

Bibliography

[1] Karp J S, Surti S, Daube-Witherspoon M E, et al. Benefit of time-of-flight in PET: experimental and clinical results. Journal of Nuclear Medicine, 2008, 49(3): 462-470.

[2] Surti S. Update on time-of-flight PET imaging. Journal of Nuclear Medicine, 2015, 56(1): 98-105.

[3] E. Auffray, F. Ben Mimoun Bel Hadj, N. Brillouet et al. Design and performance of detector modules for the endoscopic PET probe for the FP7-project EndoTOFPET-US. In Nuclear Science Symposium and Medical Imaging Conference (NSS/MIC), 2012 IEEE, pages 3236-3240, 2012.

[4] Auffray E, Hadj F B M B, Cortinovis D, et al. Characterization studies of Silicon Photomultipliers and crystals matrices for a novel time of flight PET detector. arXiv preprint arXiv:1501.04233, 2015.

[5] Florian R Schneider et al. A PET detector prototype based on digital SiPMs and GAGG scintillators. 2015 Phys. Med. Biol. 60 1667

[6] Fornaro G A, Pauwels K, Ghezzi A, et al. Study of the Angular Distribution of Scintillation Photons. Nuclear Science, IEEE Transactions on, 2014, 61(1): 456-461.

[7] Phelps M E. PET: molecular imaging and its biological applications. Springer Science and Business Media, 2004.

[8] Jens Langner. Development of a Parallel Computing Optimized Head Movement Correction Method in Positron-Emission-Tomography. Master thesis.

[9] Bailey D L, Meikle S R. A convolution-subtraction scatter correction method for 3D PET. Physics in medicine and biology, 1994, 39(3): 411.

[10] Conti M. State of the art and challenges of time-of-flight PET. Physica Medica, 2009, 25(1): 1-11.

[11] Surti S, Kuhn A, Werner M E, et al. Performance of Philips Gemini TF PET/CT scanner with special consideration for its time-of-flight imaging capabilities. Journal of Nuclear Medicine, 2007, 48(3): 471-480.

[12] Birks J B. The Theory and Practice of Scintillation Counting: International Series of Monographs in Electronics and Instrumentation. Elsevier, 2013.

[13] Bengtson B, Moszyski M. Energy-transfer and light-collection characteristics for different types of plastic scintillators. Nuclear Instruments and Methods, 1974, 117(1): 227-232.

[14] Beringer J, Arguin J F, Barnett R M, et al. Review of particle physics. Physical Review D, 2012, 86(1).

[15] Drozdowski W, Dorenbos P, Bos A J J, et al. Effect of proton dose, crystal size, and cerium concentration on scintillation yield and energy resolution of $LaBr_3$: Ce. Nuclear Science, IEEE Transactions on, 2007, 54(3): 736-740.

[16] Photomultiplier tube (PMT) basic principle. www.Hamamatsu.com.

[17] Ehrenreich H, Spaepen F. Solid state physics. Academic Press, 2001.

[18] Gundacker S. Time resolution in scintillator based detectors for positron emission tomography. CERN, 2014.

[19] Renker D, Lorenz E. Advances in solid state photon detectors. Journal of Instrumentation, 2009, 4(04): P04004.

[20] Orita T, Shimazoe K, Takahashi H. The dynamic time-over-threshold method for multichannel APD based gamma-ray detectors. Nuclear Instruments and Methods in Physics Research Section A: Accelerators, Spectrometers, Detectors and Associated Equipment, 2015, 775: 154-161.

[21] Powolny F. Characterization of time resolved photodetector systems for positron emission tomography. Neuchatel U., 2009.

[22] Collaboration A, Aamodt K. The ALICE experiment at the CERN LHC. Jinst, 2008, 3(420): S08002.

[23] F. Anghinolfi, P. Jarron, A.N. Martemiyanov et al., NINO: An ultra-fast and low-power front-end amplifier/discriminator ASIC designed for the multi gap resistive plate chamber, Nucl. Instrum. Meth. A 533 (2004) 183.

[24] Anghinolfi F, Jarron P, Krummenacher F, et al. NINO: An ultrafast low-power front-end amplifier discriminator for the time-of-flight detector in the ALICE experiment. Nuclear Science, IEEE Transactions on, 2004, 51(5): 1974-1978.

[25] Powolny, F., et al."Time-based readout of a silicon photomultiplier (SiPM) for time of flight positron emission tomography (TOF-PET)." Nuclear Science, IEEE Transactions on 58.3 (2011): 597-604.

[26] Gundacker S, Knapitsch A, Auffray E, et al. Time resolution deterioration with increasing crystal length in a TOF-PET system. Nuclear Instruments and Methods in Physics Research Section A: Accelerators, Spectrometers, Detectors and Associated Equipment, 2014, 737: 92-100.

[27] Henzler S. Time-to-digital converters. Springer Science and Business Media, 2010.

[28] J.Christiansen, "HPTDC, High Performance Time to Digital Converter version 2.2, CERN-EP/MIC (2004), http://tdc.web.cern.ch/tdc/hptdc.htm

[29] Best R E. Phase locked loops. McGraw-Hill Professional, 2007.

[30] Antonioli P, Meneghini S. A 20 ps TDC readout module for the ALICE Time of Flight system. 2003.

[31] Wolfgang C L, Herman J M, Laheru D A, et al. Recent progress in pancreatic cancer. CA: a cancer journal for clinicians, 2013, 63(5): 318-348.

[32] America Cancer Society, Cancer Facts and Figures 2010, 2010.

[33] R. Bugalho, C. Gastona, M. D. Rolo et al. EndoTOFPET-US data acquisition system. iWoRID 2012, JINST.

[34] http://www.advansid.com/home.

[35] Crowell C R, Sze S M. Temperature dependence of avalanche multiplication in semiconductors. Applied Physics Letters, 1966, 9(6): 242-244.

[36] McKay K G. Avalanche breakdown in silicon. Physical Review, 1954, 94(4): 877.

[37] Cova S, Ghioni M, Lacaita A, et al. Avalanche photodiodes and quenching circuits for single-photon detection. Applied optics, 1996, 35(12): 1956-1976.

[38] Liu Z, Doroud K, Auffray E, et al. Quality control of the TSV multi-pixel photon counter arrays, and modules for the external plate of EndoTOF-PET ultrasound detector. Nuclear Instruments and Methods in Physics Research Section A: Accelerators, Spectrometers, Detectors and Associated Equipment, 2015, 787: 240-244.

[39] Datasheet of AdvanSiD RGB SiPMs.

[40] Hurkx G A M, Klaassen D B M, Knuvers M P G. A new recombination model for device simulation including tunnelling. Electron Devices, IEEE Transactions on, 1992, 39(2): 331-338.

[41] Ramilli M. Characterization of SiPM: temperature dependencies. Nuclear Science Symposium Conference Record, 2008. NSS'08. IEEE. IEEE, 2008: 2467-2470.

[42] Collazuol G, Bisogni M G, Marcatili S, et al. Studies of silicon photomultipliers at cryogenic temperatures. Nuclear Instruments and Methods in Physics Research Section A: Accelerators, Spectrometers, Detectors and Associated Equipment, 2011, 628(1): 389-392.

[43] Lacaita A L, Zappa F, Bigliardi S, et al. On the bremsstrahlung origin of hot-carrier-induced photons in silicon devices. Electron Devices, IEEE Transactions on, 1993, 40(3): 577-582.

[44] Rech I, Ingargiola A, Spinelli R, et al. Optical crosstalk in single photon avalanche diode arrays: a new complete model. Optics express, 2008, 16(12): 8381-8394.

[45] Dietzinger C, Iskra P, Ganka T, et al. Reduction of optical crosstalk in silicon photomultipliers. SPIE NanoScience Engineering. International Society for Optics and Photonics, 2012: 84601L-84601L-9.

[46] Gallego L, Rosado J, Blanco F, et al. Modelling crosstalk in silicon photomultipliers. Journal of Instrumentation, 2013, 8(05): P05010.

[47] Datasheet KETEK.

[48] Musienko Y. State of the art in SiPMs. Industry-academia matching event on SiPM and related technologies, CERN, 2011: 16-17.

[49] Gola A, Ferri A, Tarolli A, et al. SiPM optical crosstalk amplification due to scintillator crystal: effects on timing performance. Physics in medicine and biology, 2014, 59(13): 3615.

[50] Mandai S, Jain V, Charbon E. A fully-integrated 780 800m^2 multi-digital silicon photomultiplier with column-parallel time-to-digital converter[C]//ESSCIRC (ESSCIRC), 2012 Proceedings of the. IEEE, 2012: 89-92.

[51] The International Technology Roadmap for Semiconductors, 2013 edition. http://www.itrs.net

[52] Seifert S, van Dam H T, Schaart D R. The lower bound on the timing resolution of scintillation detectors. Physics in medicine and biology, 2012, 57(7): 1797.

[53] Frach T, Prescher G, Degenhardt C, et al. The digital silicon photomultiplier-Principle of operation and intrinsic detector performance. Nuclear Science Symposium Conference Record (NSS/MIC), 2009 IEEE. IEEE, 2009: 1959-1965.

[54] Espana S, Marcinkowski R, Keereman V, et al. DigiPET: sub-millimeter spatial resolution small-animal PET imaging using thin monolithic scintillators. Physics in medicine and biology, 2014, 59(13): 3405.

[55] Mandai S, Venialgo E, Charbon E. Timing optimisation utilizing order statistics and multichannel digital silicon photomultipliers. Optics letters, 2014, 39(3): 552-554.

[56] Hamamatsu. S12643-050CN data sheet

[57] http://www.ni.com/labview.

[58] Marco Montecchi. Rome CMS group. Deeper investigation of Dow Corning 3145 and Bayer Silicones rtv 615 glues.

[59] Chitnis A, Kumar A, Shatalov M, et al. High-quality p/n junctions with quaternary AlInGaN/InGaN quantum wells. Applied Physics Letters, 2000, 77(23): 3800-3802.

[60] Perlin P, Osiski M, Eliseev P G, et al. Low temperature study of current and electroluminescence in InGaN/AlGaN/GaN double heterostructure blue light emitting diodes. Applied physics letters, 1996, 69(12): 1680-1682.

[61] http://www.picoquant.com

[62] Technical Information Manual. CAEN. Mod. V1290-VX1290 A/N, 32/16 Ch. Multihit TDC. 22 February 2010

[63] 3M, Vikuiti Enhanced Specular Reflector (ESR); http://www.3m.com

[64] Auffray E, Frisch B, Geraci F, et al. A Comprehensive and Systematic Study of Coincidence Time Resolution and Light Yield Using Scintillators of Different Size and Wrapping. Nuclear Science, IEEE Transactions on, 2013, 60(5): 3163-3171.

[65] Daniel McDonald, Calibration of the STAR Time-of-Flight Detector for Particle Identification. Master thesis.

[66] EndoTOFPET-US collaboration report.

[67] Mandai S, Charbon E. A 4 x 4 x 416 digital SiPM array with 192 TDCs for multiple high-resolution timestamp acquisition. Journal of Instrumentation, 2013, 8(05): P05024.

[68] Xu C, Garutti E, Mandai S, et al. Comparison of digital and analog silicon photomultiplier for positron emission tomography application[C]//Nuclear Science Symposium and Medical Imaging Conference (NSS/MIC), 2013 IEEE. IEEE, 2013: 1-7.

[69] Ralf Schulze. PDPC-TEK user manual, Philips Digital Photon Counting. v0.20, 2013-07-30

[70] Tabacchini V, Westerwoudt V, Borghi G, et al. Probabilities of triggering and validation in a digital silicon photomultiplier. Journal of Instrumentation, 2014, 9(06): P06016.

[71] Van Dam H T, Borghi G, Seifert S, et al. Sub-200 ps CRT in monolithic scintillator PET detectors using digital SiPM arrays and maximum likelihood interaction time estimation[J]. Physics in medicine and biology, 2013, 58(10): 3243.

[72] Frach T, Prescher G, Degenhardt C, et al. The digital silicon photomultiplier system architecture and performance evaluation. Nuclear Science Symposium Conference Record (NSS/MIC), 2010 IEEE. IEEE, 2010: 1722-1727.

[73] Eckert P, Schultz-Coulon H C, Shen W, et al. Characterisation studies of silicon photomultipliers. Nuclear Instruments and Methods in Physics Research Section A: Accelerators, Spectrometers, Detectors and Associated Equipment, 2010, 620(2): 217-226.

[74] Gundacker S, Auffray E, Di Vara N, et al. SiPM time resolution: From single photon to saturation. Nuclear Instruments and Methods in Physics Research Section A: Accelerators, Spectrometers, Detectors and Associated Equipment, 2013, 718: 569-572.

[75] Acerbi F, Ferri A, Gola A, et al. Characterization of single-photon time resolution: from single SPAD to silicon photomultiplier[J]. Nuclear Science, IEEE Transactions on, 2014, 61(5): 2678-2686.

[76] Yeom J Y, Vinke R, Bieniosek M F, et al. Comparison of end/side scintillator readout with digital-SiPM for ToF PET. Nuclear Science Symposium and Medical Imaging Conference (NSS/MIC), 2013 IEEE. IEEE, 2013: 1-3.

[77] Performance analysis of digital silicon photomultipliers for PET. Somlai-Schweiger I, Schneider F R, Ziegler S I. Journal of Instrumentation, 2015, 10(05): P05005.

[78] http://www.hamamatsu.com/jp/en/product/category/3100/3001/R2059/index.html

[79] Agostinelli S, Allison J, Amako K, et al. GEANT4. a simulation toolkit. Nuclear instruments and methods in physics research section A: Accelerators, Spectrometers, Detectors and Associated Equipment, 2003, 506(3): 250-303.

[80] R.M. Turtos, M. Pizzichemi, E. Auffury, et al. *Measurement of LYSO Intrinsic Light yield using electron excitation.* 13th *International Conference on Inorganic Scintillators and Their Applications* (SCINT 2015).

[81] Hamamatsu Photonics K.K. TSV MPPC array datasheet. www.hamamatsu.com